Space-Charge Effect in Strong-Field Ionization of Dense Media

im Fachbereich Physik
der Freien Universität Berlin
eingereichte Dissertation zur Erlangung des akademischen Grades der Doktorin der Naturwissenschaften (Dr. rer. nat.)
vorgelegt von
Ruba Taha Salim Al-Obaidi
Berlin
2016

HZB Helmholtz Zentrum Berlin

Die in vorliegender Dissertation dargestellte Arbeit wurde in der Zeit zwischen Juni 2012 und August 2016 im Fachbereich Physik an der Freien Universität Berlin unter Betreuung von Prof. Emad Flear Aziz durchgeführt.

1. Gutachter: Prof. Dr. Emad Flear Aziz
2. Gutachter: Prof. Dr. Ludger Wöste

Disputation am. 25/11/2016

‘‘Gedruckt mit Unterstutzung des Deutschen Akademischen Austauschdienstes‘‘

Table of Contents

Acknowledgments

First of all, I want to thank my God the most merciful to give me many things in my life. I would like to start by expressing my sincere gratitude to my advisor Prof. Emad Flear Aziz for the continuous support of my Ph.D. study and related research, for his patience, and motivation. My thanks go also to my second supervisor, Prof. Ludger Wöste, who was always available for discussing my work, and who also gave me the chance to study in the lovely city Berlin, Germany.

I would also like to thank my co-supervisor Dr. Igor Kiyan for the scientific discussion of my Ph.D. research. And also I would like to thank Dr. Bernd Winter, Dr. Kaan Atak, and Dr. Valeri Kozich for having discussed with me several topics of my work.

Special thank goes also to my family for large and continuous support, especially my wonderful mother who give me the trust and the power during my thesis work, to my great father who encourages me in all question of study and life, and I learned from his theater and plays the philosophy of life. To my loving sisters and brothers, especially my sister Shatha the most affectionate, and my brother Faiz who encouraged me to study outside Iraq, and finally to my beloved nephews. Special thanks also to Amr Abo-elela for supporting me in my study time. Also, I would like to thank my professors in my university in Iraq who provided me with the knowledge that prepared me for conducting the present work.

Very special thanks to Azhar Raheem for supporting me in my beam time. I also like to thank my group, particularly Jan Metje, Martin Wilke, Daniel Tolksdorf, and Nicholas Engel for their continuous scientific advice and assistance with experimental issues.

And I want to thank the Deutscher Akademischer Austauschdienst (DAAD) and the Ministry of higher education of Iraq for covering my expenses during my research.

Finally, I would also like to thank my friends in the physics department, and my colleagues in the Science department of Al-Mustansiriya University, Dr. Faten Azit, Osama Abd al-Aziz, Suha Al- Ani, Samar Tarish Norah Shamoun, Randa Kamil, Saher al-Aziz, and Baidi Muhsin, and also for the people that I have met them in Berlin, Heba tlallah, and Lamia Samer.

At the end, thanks go to my lovely city Baghdad.

Abbreviations

ATI	Above threshold Ionization
FFT	Free-free transition
HATI	High-order-above threshold ionization
HHG	High harmonic generation
LAPE	Laser assisted photoelectric effect
MP	Multiphoton processes
MPI	Multiphoton ionization
NIR	Near-infrared light
OBI	Over-the barrier ionization process
PES	Photoelectron spectroscopy
RIS	Resonance ionization spectroscopy
SCE	Space-charge effect
SFA	Strong -field approximation
SPV	Surface photovoltage
TARPS	Time and angle-resolved photoemission spectroscopy
TPES	Transient electron photoemission spectroscopy
UPS	The ultraviolet photoelectron spectroscopy
XPS	X-ray photoelectron spectroscopy
ZEKE	Zero electron kinetic energy
2PPS	Two-photon photoelectron spectroscopy

List of Figures

List of Publications

1. **Ultrafast photoelectron spectroscopy of solutions: space-charge effect**

   R. Al-Obaidi, M. Wilke, M. Borgwardt, J. Metje, A. Moguilevski, N. Engel, D. Tolksdorf, A. Raheem, T. Kampen, S. Mähl, I. Yu Kiyan and E. F. Aziz

   New Journal of Physics 17 (2015) 093016

   http://dx.doi.org/10.1088/1367-2630/17/9/093016

2. **Laser-assisted electron scattering in strong-field ionization of dense water vapor by ultrashort laser pulses**

   M. Wilke, **R. Al-Obaidi,** A. Moguilevski, A Kothe, N. Engel, J. Metje, I. Yu Kiyan, and E. F. Aziz

   New Journal of Physics 16 (2014) 083032

   http://dx.doi:10.1088/1367-2630/16/8/083032

3. **Multi-plateau structure in photoemission spectra of strong-field ionization of dense media**.

   M. Wilke, **R. Al-Obaidi**, I. Yu. Kiyan, and E. F. Aziz.

   Physical Review A, 94, 033423 – Published 29 September 2016

   https://doi.org/10.1103/PhysRevA.94.033423

4. **XUV photoelectron spectroscopy of halide anions in aqueous solutions**.

   Jan Metje, Daniel Tolksdorf, **Ruba Al-Obaidi**, Thorsten Kampen, Sven Mähl, Igor Yu. Kiyan, and Emad F. Aziz.

   Submitted.

5. **Monochromatization of femtosecond XUV light pulses with the use of reflection zone plates**

   Jan Metje, Mario Borgwardt, Alexandre Moguilevski, Alexander Kothe, Nicholas Engel, Martin Wilke, **Ruba Al-Obaidi**, Daniel Tolksdorf, Alexander Firsov, Maria Brzhezinskaya, Alexei Erko, Igor Yu. Kiyan, and Emad F. Aziz

   Optics Express, Vol. 22, Issue 9, pp. 10747-10760 (2014)

   https://doi.org/10.1364/OE.22.010747

6. **Time-of-flight electron spectrometer for a broad range of kinetic energies**

   Alexander Kothe, Jan Metje, Martin Wilke, Alexandre Moguilevski, Nicholas Engel, **Ruba Al-Obaidi**, Clemens Richter, Ronny Golnak, Igor Yu. Kiyan, and Emad F. Aziz, Review of scientific instruments. 84, 023106 (2013).

   http://dx.doi.org/10.1063/1.4791792

Chapter 1

Introduction

The recent development of modern laser technologies enables scientists to conduct experiments using ultra-short light pulses in intense laser fields. The extremely high peak intensities and the wide tuning range of photon energies available nowadays provide the possibility to study a variety of processes occurring during the interaction of a strong laser field with matter. When the laser field is sufficient to overcome the Coulomb potential in the quantum system, the dynamics of atoms and molecules is governed by the laser field. Various nonlinear processes occurs, such as *Multiphoton Ionization* (MPI), *Above Threshold Ionization* (ATI), *High-order-Above Threshold Ionization* (HATI), *High Harmonic Generation* (HHG), *atomic stabilization*, or *molecular dissociation* and *laser-assisted electron–atom collisions* [1-16]. Photoelectron spectroscopy (PES) finds a wide range of applications in the study of these processes, allowing to track the electronic and molecular dynamics of molecular systems. Earlier experiments were focused on studying the electronic and molecular dynamics in the gas and solid-state phase using PES methods [17-19].

Nowadays, the PES method can also be applied to investigate photo processes induced by an intense laser field in the liquid phase [20-22]. The study of electronic and structural dynamics in solutions and at interfaces received much attention during the past decade [20-27]. The development of the liquid microjet technique is uniquely suited for carrying out such experiments [28, 29]. Since the application of intense laser fields to solutions is novel, many fundamental questions are yet to be explored. Accordingly, it is interesting to investigate the electronic and molecular dynamics of the liquid phase, and it is anticipated that these new results will differ from those in gas and solid phase. The interest and the importance of these studies arise from the fact that solutions represent a natural environment

for most biochemical complexes [30-33]. Various non-radiative electronic transitions can be initiated by light in biochemical complexes. Charge transfer [34], electron solvation [20-27, 30-35], spin crossover [36, 37], and photo-oxidation [38] represent some of them. Depending on the transition character, the time scale of the complex dynamics can lie in the femtosecond range, requiring the application of ultrafast spectroscopies to study photo-reactions in detail. Different time-resolved spectroscopic methods are developed to follow the dynamics of a biochemical system upon photoexcitation. Among these are transient absorption and fluorescence spectroscopies [38, 39], and transient electron photoemission spectroscopy (PES) [40-45].

The present work is devoted to the latter approach. It is advantageous for the unambiguous determination of the electron population distribution among different states to map the electron density by ionization and record the kinetic energy spectrum of the emitted photoelectrons. While the electron dynamics can be initiated by photons in the UV/visible wavelength range, application of XUV light from high-order harmonic generation HHG represents a suitable tool for monitoring the electron population at a given time after the excitation [22, 44-46]. XUV photon energy is sufficient for probing the entire valence electronic structure in a one-photon transition into the continuum (i.e., by 1-photon ionization). The HHG setup developed by our group for time-resolved spectroscopic studies of solutions [47] is employed in this work.

Photoexcitation of the solute with the use of a short laser pulse imposes some specific conditions on the pump laser intensity. The reason is that the photoelectron spectrum, generated by the XUV probe pulse, is dominated by the ionization yield of the solvent due to its much higher number density. In order to identify changes in the kinetic energy spectra associated with the electron population dynamics of the solute, a substantial amount of the solute molecules must be initially excited by the pump pulse. For one-photon excitation, the transition probability can be estimated as $W = \sigma\,\tau(I/\hbar\omega)$, where σ is the photoabsorption cross section, τ is the pulse duration, I is the laser intensity, and $\hbar\omega$ is the photon energy. The

expression for W immediately implies that application of a shorter pulse requires a higher laser intensity in order to achieve the same yield of a given photoreaction process. The saturation condition, W~1, represents the ideal case where all solute molecules in the interaction region are excited. The intensity requirement becomes weaker if the photoreaction cross section is resonantly enhanced due to population of an excited state. However, the laser field may still be strong enough to ionize the solvent medium efficiently. This leads to the emission of many electrons, which in the case of a poor conductor leads to the formation of space charge at the interface of the system. Its effect on the XUV photoemission spectra of aqueous solutions represents the subject of this work.

The photoelectrons generated by high-intensity short pulses in a medium of a fairly high density are influenced by space-charge effect (SCE), induced by the Coulomb interactions between charged particles created in the laser field. SCE is caused not only by the electron-electron interaction but also by the electron-positive ions interaction. Space charge manifests itself in photoelectron spectra as an effect accompanies processes induced in a strong laser field [48-51]. It distorts the spectral distribution of the photoelectrons and decreases the energy resolution in the PES measurements. Therefore, a proper treatment of this effect in pump-probe studies represents an important issue addressed in the present work.

To describe the SCE occurring in pump-probe studies of liquid samples, a model is presented in this thesis based on *the mean-field consideration* and the *field superposition principle*. The model is tested in an experiment where an aqueous solution of potassium ferrocyanide $[Fe(CN)_6]^{4-}$ is used as the sample. An analogous approach was used before to describe the SCE in pump-probe experiments of the solid sample [52].

Apart of the manifestation of SCE in transient XUV spectra, its influence on photoemission spectra from dense media exposed to a strong infrared laser pulse is also considered in this work. Strong-field ionization, involving MPI, ATI, and high-order ATI, was studied on a fundamental level during the past decades. The processes are described by theories based on

strong-field approximation (SFA) [53], where the interaction of the emitted electron with the residual core is neglected in the final continuum state. Angle-resolved photoemission spectra generated by a strong laser field are used for testing the SFA theories. The question arises whether the measured spectra are distorted by the SCE. This issue is addressed in the second part of this thesis, where strong-field ionization of a dense gas (vapor) with variable density is studied in the case of linearly and circularly polarized light. In particular, we address the question as at which value of the medium density and ionization degree does the SCE become relevant in femtosecond photoemission spectra.

The thesis is organized as following: In Chapter 2, various aspects and concepts of physics necessary to understand this work, are introduced. These include a discussion of the ionization process in moderate and strong laser fields, the basic principle of HHG, the principle of the PES method, the previous studies of SCE induced by single laser pulse and by a pump-probe pulse sequence, the electronic structure of water, and the electronic structure of potassium ferrocyanide used as a solute in the present study. The experimental setup is described in detail in Chapter 3. The results of the study of SCE with the use of UV-pump and XUV-probe experiment is presented in Chapter 4, including the model of SCE. Chapter 5 presents the study of strong-field ionization of water vapor in a linear and circular field of high intensity.

Chapter 2

Interaction of Atoms and Molecules with Laser Fields

When an atom is exposed to a laser field, the intra-atomic electronic potential becomes significantly perturbed. An additional potential V representing the electron interaction with external field appears in the Hamiltonian.

$$H(t) = H_0 + V(t) , \tag{2.1}$$

where H_0 is the field-free Hamiltonian. The interaction of a short intense laser pulse with atoms and molecules leads to multiphoton ionization of these species. The principle of the description of this process is the same for systems. However, when electrons are ionized from different atoms of a molecule at the same time, the resulting electrostatic force between the created positive ions leads to the Coulomb explosion of the molecule [54]. This represents a specific feature of molecular ionization in a strong field. If the laser intensity is sufficiently strong so that it overcomes the intra-molecular potential, the dissociation dynamics of the molecules occurs [55].

The laser-induced molecular dynamics are more complex than the atomic dynamics because more degrees of freedom are involved. Here not only the electronic motions around the nucleus contribute but also nuclear motions are important. In general, the study of molecular systems becomes increasingly difficult as the size of molecules increases.

In this chapter, we first consider different channels of photoionization processes. Sections 2.1and 2.2 specify the processes such as MPI, ATI, high-order ATI, laser-assisted, and sequential and non-sequential ionization process. Section 2.3 provides an introduction to

strong-field approximation. Section 2.4 explains the strong field ionization in a circularly polarized field. A description of the ionization and HHG processes in terms of semiclassical electron trajectories is given in section 2.5 and 2.6, respectively. Section 2.7 describes the methods of photoelectron spectroscopy. Sections 2.8 and 2.9 present the results of the previous studies on the space-charge effect induced by a strong laser field in single-beam experiments and in time-resolved photoelectron spectroscopy experiments, respectively. In section 2.10 we describe the electronic structure of water molecule in the gas and liquid phase. The last section of this chapter describes the structure of $K_4[Fe(CN)_6]^{4-}$ which is the solute used in the present pump-probe experiments from aqueous solution.

2.1 Ionization in a Laser Field of Moderate Intensity

The interaction of atoms and molecules with electromagnetic fields can give rise not only to single-photon absorption or emission processes but also to higher order processes. They are called multiphoton processes (MP) and were described for the first time in 1926 by Lewis [56]. There are several types MP processes. Atoms can absorb more than one photon leading to a transition from the ground state to a higher excited state. This process is known as *multiphoton excitation*. Another process, opposite to the *multiphoton excitation* is called *multiphoton de-excitation*. It takes place when an atom in an excited state emits n photons and returns to the ground state. This process can be of stimulated or spontaneous emission character. When the radiation field has sufficient intensity, atoms can absorb a number of photons of energy $\hbar\omega$ with the total energy larger than the electron binding energy of the initial state ($n\hbar\omega > I_p$). This leads to the emission of one or several of atomic electrons. These MP photoionization processes can be:

$$A^q + n\hbar\omega \longrightarrow A^{q+1} + e^- , \qquad (2.2)$$

where q is the charge of the atomic system A in the initial state and n is the number of the absorbed photons. The emitted electron possesses a kinetic energy equal to:

$$E = n\hbar\omega - I_p, \tag{2.3}$$

where I_p is the ionization potential of the atom. This process, called *multiphoton single ionization*, is another type of MP processes. *The multiphoton ionization* (MPI) process was first observed in 1963 by Damon and Tomlinson [57]. The laser intensity plays a significant role to determine the MPI character [15]. It can be expressed in the atomic unit of intensity:

$$I_a = \frac{1}{2} \epsilon_0 \, c\varepsilon_a^2 \simeq 3.5 * 10^{16} W cm^{-2}, \tag{2.4}$$

where c is the speed of light, ϵ_0 is the free space permittivity and ε_a is the atomic unit of the field strength defined as:

$$\varepsilon_a = \frac{e}{(4\pi \epsilon_0) a_0^2} \simeq 5.1 * 10^9 \; V cm^{-1}, \tag{2.5}$$

here e is the electron charge and a_0 is the Bohr radius of the hydrogen atom.

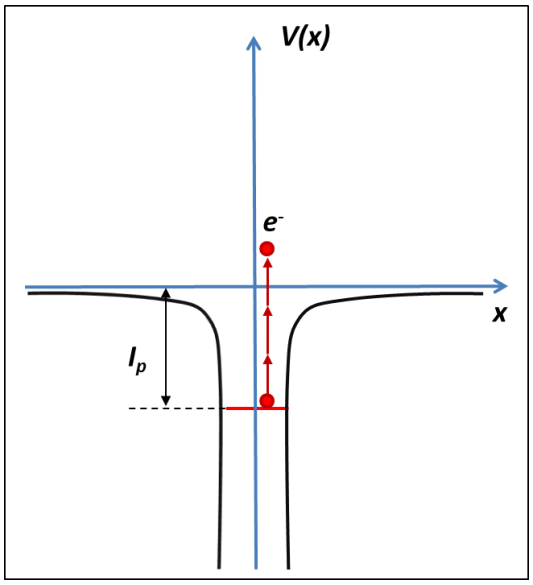

Figure 2.1 Multiphoton ionization (MPI) process.

At moderate intensities, the perturbation of the atomic system by an external field is small and the MP transition of the electron from the ground state to the continuum can be described by time-dependent perturbation theory [15]. Figure 2.1 shows a simple diagram of

MPI process. For an MPI process at low intensities, it was found that the ionization rate J is proportional to I^n. Strictly speaking, the energy conservation described by Eq. (2.3) is rigorous only in the limit $I \to 0$. For a non-vanishing intensity value, the electron ejected from the atom needs to possess additional energy associated with its quiver motion in the external electromagnetic field which is still present after the ionization transition event. This energy, which is additional to the drift kinetic energy, needs to be supplied from the total energy of absorbed photons. Thus, instead of Eq. (2.3) the exact energy conservation rule has the form:

$$E = n\hbar\omega - I_p - U_p \,, \tag{2.6}$$

where U_p represents the cycle-averaged kinetic energy of the quivering electron in the laser field, known as *ponderomotive energy*. For a monochromatic linearly polarized laser field, it is given by:

$$U_p = \frac{e^2 \varepsilon_0^2}{4m\omega^2} \,, \tag{2.7}$$

where m is the electron mass, ε_0 is the electric field strength and ω is the laser frequency [58]. In atomic units ($m=1, e=1, c=1, \hbar=1$), Eq. (2.7) reads:

$$U_p = \frac{F^2}{4\omega^2} = \frac{I}{4\omega^2} \,. \tag{2.8}$$

If the laser intensity is expressed in W/cm^2 and the wavelength λ is expressed in μm, the value of U_p expressed in eV has the form:

$$U_p = 9.33 \times 10^{-14} (I\lambda^2) \,. \tag{2.9}$$

The U_p is linearly proportional to the instantaneous laser intensity $I(\vec{r})$. It varies with the spatiotemporal pulse envelope. In a non-uniform electromagnetic field, a charged particle experiences a force which is proportional to the gradient of the ponderomotive energy:

$$\vec{F} = -\nabla U_p(\vec{r}) \tag{2.10}$$

In a laser focus with a Gaussian radial intensity distribution across the beam axis, the ponderomotive force Eq. (2.10) pushes electrons away from the focus. Thus, electrons can

gain a kinetic energy due to this acceleration, which is equal exactly to U_p. However, this energy gain is possible only if the laser field is present all the time, it takes far the electron to escape the focus. If the pulse is too short, the energy gain is smaller than U_p. Therefore, the kinetic energy spectrum of photoelectrons recorded by a detector in the far field is different for long and short pulses. In the limit of long pulse duration, the electron leaves the laser focus before the light turns off so that the electron ponderomotive energy at the moment of ionization is converted to translation kinetic energy when the electron drifts down the edge of the focus. This gain in the kinetic energy compensates the energy loss due to the ponderomotive shift of the ionization threshold discussed above. In this case, the electron kinetic energy, detected in a PES experiment is described by Eq. (2.3). In the short pulse regime, the electron does not have time to move far enough during the laser pulse and, therefore, does not gain the ponderomotive energy [59, 60]. In this case, its kinetic energy at the detector is described by Eq. (2.6).

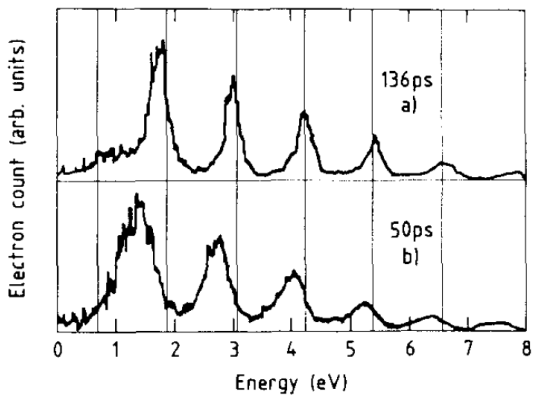

Figure 2.2. Electron energy spectra obtained for Xe at the intensity of 7.5×10^{12} W/cm^2 for 1064 nm wavelength. The spectra are recorded for two different pulse durations (a) 136 ps, and (b) 50 ps [59].

As an illustration, Figure 2.2 shows the photoelectron spectra of xenon measured at 1064 nm laser wavelength for two different pulse durations of 136 ps (a) and 50 ps (b). The laser intensity is 7.5×10^{12} W/cm^2 corresponding to the ponderomotive energy of 0.7 eV. Electron

energy spectra are shifted to lower kinetic energy due to the ponderomotive energy shift of the ionization threshold when the pulse length is decreased from 136 to 50 ps. This demonstrates the transition from the long- to the short-pulse regime. The multi-peak structure in the spectra shown in Figure 2.2 arises from above-threshold ionization which is considered in the next section.

2.2 Strong-Field Ionization

At sufficiently high intensities, new effects in the multiphoton ionization process appear. The ejected electron can absorb photons in excess of the minimum number required for ionization to occur. It is the presence of the Coulomb field of the still nearby residual ion, which enables the electrons to absorb additional photons. This phenomenon is called *above-threshold ionization* (ATI) [10, 15, 61]. It was first observed by Agostini et al. in 1979 [62] in the experiments performed in the long pulse regime and with laser intensities of $I>10^{11}$W/cm^2. The process of ATI is depicted in Figure 2.3.

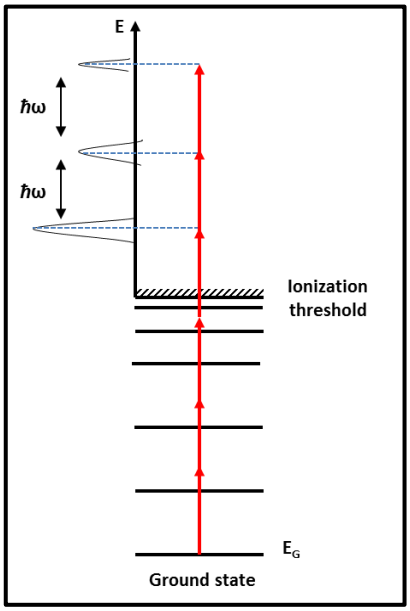

Figure 2.3. Above threshold ionization (ATI) process.

Figure 2.4 shows the ATI photoelectron energy spectra obtained in the experiment by Petite, Agostini, and Muller [63]. The Nd: YAG laser of 130 ps pulse duration and 1064 nm wavelength was used to ionize xenon gas. At low laser intensities, the emission yield of multiphoton ionization can be described in terms of perturbation theory. In this case, the ionization rate J for the (n_0+s)-photon process is proportional to I^{n_0+s}. This dependency is valid if there are no multiphoton resonances between the initial state and excited states of the atom.

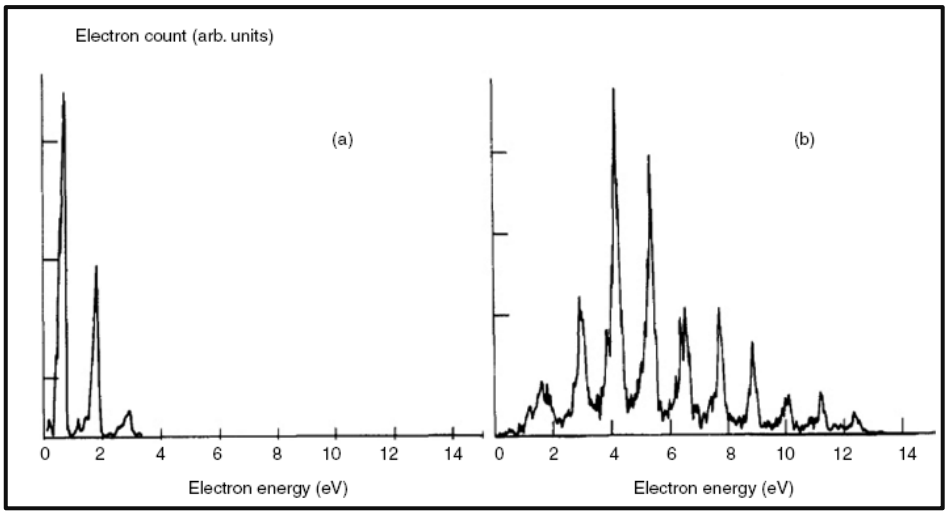

Figure 2.4. The photoelectron spectra of above threshold ionization ATI of xenon at the laser wavelength of 1046 nm (a) I=2.2×10^{12} W/cm^2, (b) I=1.1×10^{13} W/cm^2 [63].

Panels (a) and (b) show the photoelectron spectra measured at lower and higher intensity of 2.2×10^{12} W/cm^2 and 1.1×10^{13} W/cm^2, respectively. Both photoelectron spectra consist of several ATI peaks, separated by the photon energy $\hbar\omega$, and appearing at energies E_s [15].

$$E_s = (n_0 + s)\,\hbar\omega - I_p, \tag{2.11}$$

where n_0 is the minimum number of photons needed to ionize the atom, and s=0,1,2….is the number of excess photons or (above-threshold photons) absorbed by the atom.

In the long pulse regime and at high laser field intensity, this polynomial dependency does not hold because of different effects influencing the ionization process. First, the perturbation of atomic states, leading to their ac-Stark shifts, has been found to cause resonant enhancement of the ATI process [7].

This is schematically depicted in Figure 2.5 where it is considered that the unperturbed atom requires 4 photons to overcome the ionization potential and there are no resonance conditions for multiphoton transitions from the ground to excited states in the low-intensity limit. With the increase of the laser intensity, the energy levels of excited states undergo the ac-Stark shift. This shift of Rydberg states, which are depicted in Figure 2.5, is equal approximately to the ponderomotive energy U_p. One can see that due to such a shift, the 3-photon resonance condition can be fulfilled at intensity I_2 for the transition from the ground state to the Rydberg state R_1, whereas a 4-photon resonance with R_2 is depicted at intensity I_3. One should note that the ground state also experiences an ac-Stark shift. However, its value, which is defined by the dipole polarizability of the atom, is typically much smaller than U_p.

Second, as already discussed above, the ponderomotive energy term needs to be considered in the energy conservation rules (see Eq. 2.3). This can be understood as an increase of the ionization potential by than U_p, which is also depicted in Figure 2.5. Then, ionization by four photons, which is possible at the intensity I_1, becomes forbidden at the higher intensities I_2 and I_3, where five photons are needed to ionize the atom.

The suppression of the low-energy peaks in ATI spectra is evident from the panel (b) of Figure 2.4. This effect is called as *channel closing*.

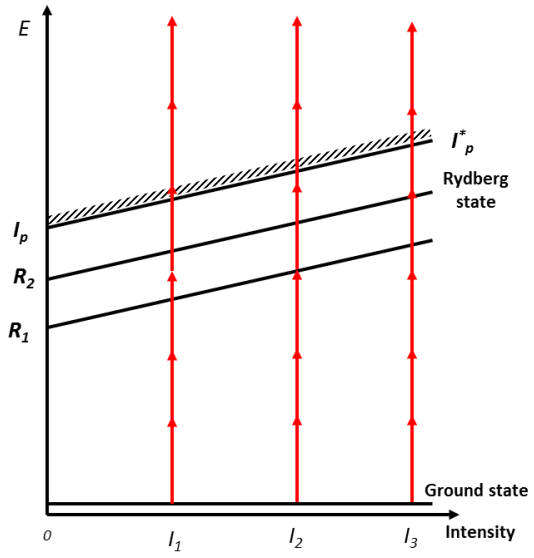

Figure 2.5. Resonant enhancement of ATI process.

In the short laser pulse regime, electrons do not escape from the focal volume before the laser field turns off. In this case, the quiver energy of the ejected electron is returned back to the electromagnetic field and the photoelectrons energies are given by:

$$E_s = (n_0 + s)\hbar\omega - (I_p + U_p), \tag{2.12}$$

Figure 2.6 demonstrates the change of the photoelectron spectra of xenon measured at different pulse durations in the range from 0.4 to 13 ps, while the pulse energy is kept constant. The peak intensity in the laser focus increases from 1.2×10^{13} W/cm^2 for the 13 ps pulse to 3.9×10^{14} W/cm^2 for the 0.4 ps pulse. The spectral shift and the broadening of ATI peaks are evident in the figure. The broadening arises from the spatiotemporal intensity distribution in the laser focus, leading to different ponderomotive shifts of the ionization threshold for different local intensity values. For the shorter pulse widths, the individual ATI peaks break up into a narrow fine structure. This substructure arises from the fact that the

intensity-dependent Stark shifts bring different excited states of the atom into multiphoton resonance during the laser pulse [64].

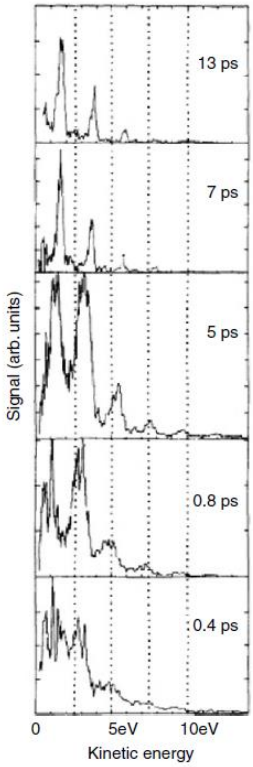

Figure 2.6. Photoelectron kinetic energy of xenon as a function of the laser pulse duration. The intensity increases from 1.2×10^{13} W/cm^2 for the 13 ps pulse to 3.9×10^{14} W/cm^2, while the pulse duration changes from 13 ps to 0.4 ps [64].

Another effect of the interaction of strong laser fields with atomic systems consists of high-order above-threshold ionization (HATI). The process occurs when the released electron is turned back to the core by the external laser field, where it scatters elastically off the parent ion which leads to gain in the kinetic energy. The high-energy spectrum of electrons observed in this process is characterized by a plateau (an energy interval during which the probability of the process is approximately constant) which is terminated as an abrupt cut-off

[65, 66]. Figure 2.7 shows spectra of photoelectrons produced by ionization of rare-gas atoms at high intensities in the visible range. The signal falls off rapidly for the first 10 to 20 ATI peaks. The following peaks, however, are of comparable heights, thus forming a plateau. These peaks are followed by a steep roll-off-the cut-off [67].

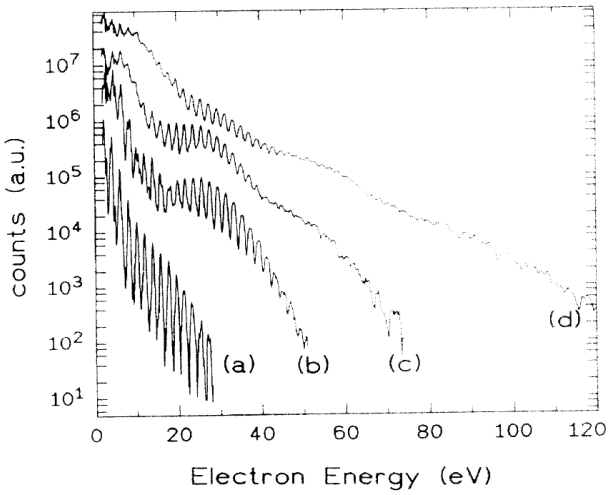

Figure 2.7. High-order above-threshold (HATI) spectra from argon with 40 fs, 630 nm pulses at intensities of to 6×10^{13} W/cm^2 (a), 1.2×10^{14} W/cm^2 (b), 2.4×10^{14} W/cm^2 (c), and 4.4×10^{14} W/cm^2 (d) [67].

The cut-off law derived for HATI reads $E_{max}=10.007\ U_p$. It was obtained by Paulus and *et al* [68].

The processes such as MPI and ATI represent original processes which can occur in the presence of a laser field, laser-assisted processes are phenomena that are modified by the presence of a laser field. It involves processes of the basic electron–atom collisions in the presence of a laser field. The processes were first observed in electron-atom scattering with the use of CO_2 laser field [69]. The laser-assisted electron dynamics can be classified into three types [15]:

I. Laser-assisted "elastic" collisions.

$$e^- + A(i) + n\hbar\omega \rightarrow e^- + A(i) \tag{2.13}$$

II. Laser-assisted inelastic collisions.

$$e^- + A(i) + n\hbar\omega \rightarrow e^- + A(f) \tag{2.14}$$

III. Laser-assisted single ionization (e, 2e) collisions.

$$e^- + A(i) + n\hbar\omega \rightarrow A(f)^+ + 2e^-, \tag{2.15}$$

were *A(i)* and *A(f)* denote an atom *A* in the initial state *i* and the final state *f* .The processes (2.13)–(2.15) are particular cases of transitions for which the electron–atom system under investigation is initially and finally in a continuum state. Such transitions are therefore called "free–free transitions" (FFT).

In the pump-probe experiments with the use of light from high harmonic generation as the probe pulse the laser-assisted electron dynamics also take place when the pump and probe pulses overlap in time [47, 70]. In this process, one or *n* photons of the low frequency of the pump beam can be absorbed or emitted simultaneously with the absorption of one XUV photon of the probe beam. Thus, the pump beam of low frequency can induce the free-free transition. The kinetic energy of the photoelectron can thus be expressed as:

$$E = \hbar\omega_{probe} + n\hbar\omega_{pump} - I_p \tag{2.16}$$

In the electron energy spectrum, such FFT results in the generation of sidebands in the photoelectron spectrum, corresponding to the absorption and stimulated emission of photons from the laser field. The sidebands represent the cross-correlation signal whose amplitudes are proportional to the product of the pump and probe beam intensities. When the pump pulse is delayed by a time τ with respect to probe pulse, the total population of the N^{th} sideband is proportional to the convolution of the two pulses:

$$S^N(\tau) \propto \int_{-\infty}^{\infty} I_{probe}(t) I_{pump}^n(t-\tau)dt, \tag{2.17}$$

where I_{probe} and I_{pump} are the intensity of the probe and the pump beam, respectively. The sidebands are separate from the ionization peak by the pump photon energy. The possibility of cross-correlation measurements on a solid surface by means of the laser-assisted photoelectric effect with the use of XUV light was demonstrated in [71]. A similar approach is applied in this work, where the liquid jet is used instead of the solid sample (see section 3.3).

Apart from single ionization of atomic in a strong laser field, multiple ionization can also take place. Double ionization was considered in detail by Walker *et al.* in (1994) [72] who initiated a new investigation of the MPI processes. It was shown that there are two types of double ionization, *sequential and non-sequential*. While the sequential process can be considered in two steps, where single ionization of atom is followed by single ionization of the created positive ion, the sequential process can be represented as:

$$A^q + n\hbar\omega \longrightarrow A^{q+2} + 2e^-. \tag{2.18}$$

The non-sequential double ionization processes have received a description as being due to the shake-off mechanism. In this representation, one electron is removed from a neutral atom or molecule which leads to change in the effective potential of the atomic core. The second electron is influenced by this fast change of the effective potential. As a result, the second electron is also ejected from the atom. The non-sequential double ionization process takes place at lower laser intensities, as compared to the intensities at which the sequential mechanism dominates. Typical intensity values at which the non-sequential double ionization dominates in the experiment [72] lie below10^{14} W/cm^2.

At long wavelengths and sufficient strong laser field, the ionization process can be described by using a quasi-static model, in which the bound electron experiences an effective potential formed by a superposition of the atomic potential and the potential of the instantaneous laser electric field *F(t)*. As a result, a potential barrier is created and the maximum of this barrier lies below the original ionization threshold. This is illustrated in Figure 2.8. Here, the blue solid lines represent the dipole potential of the external electric field *xF(t)*, lines represent the

superposition of the atomic and the laser field potentials. The energy level of the initial unperturbed state is indicated by the red line. Thus, the bound electron can tunnel through the created potential barrier (see Figure 2.8 (a)). This process is called *tunneling ionization*. The ionization rate can be calculated by using the expression of DC-tunneling theory, which was implemented by Ammosov, Delone and Krainov (ADK) [73, 74]. As a result, the ionization rate has the form:

$$w_{ADK}(t) = 4\frac{2IP^{5/2}}{F(t)}exp\left(-\frac{2(2IP)^{3/2}}{3F(t)}\right). \tag{2.19}$$

Eq. (2.19) is subsequently averaged over the field strength *F(t)* within the optical cycle of the laser field. If the laser field strength is increased further, the created potential barrier becomes lower than the energy level of the initial state (see Figure 2.8 (b)). In this case, the process changes from tunneling to the *over-barrier ionization process* (OBI). The sharp ATI peaks of the photoelectron spectra gradually convert into a continuous energy distribution [15]. The critical laser intensity, at which the tunneling and over-barrier ionization interchange each other, is defined by the condition that the maximum of the potential barrier acquires the value of the binding energy E_b.

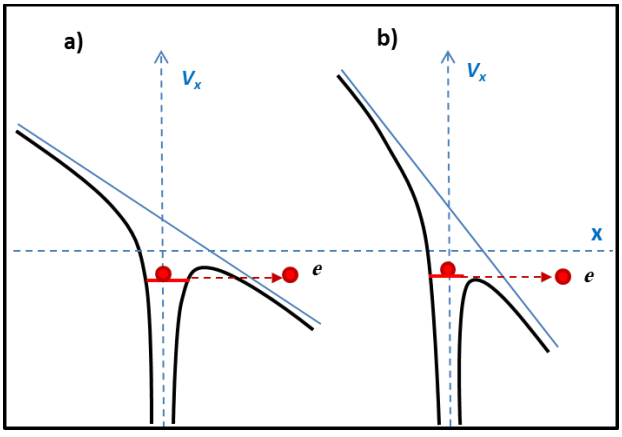

Figure 2.8. The potential barrier formed by the superposition of the atomic and the laser field potentials. Depending on the position of the barrier maximum, tunneling ionization (a), or over-barrier ionization (b) occurs.

The quasi-static theory relies on the condition that the laser frequency is low and the field strength is high so that the tunneling time is shorter than the period of the optical cycle. The fundamental parameter describing this condition is known as *the Kelydsh adiabaticity parameter* γ, which relates the time scale of the electron motion under the barrier and the laser field period [75]. It can be expressed as:

$$\gamma = \sqrt{\frac{I_p}{2U_p}} \ . \tag{2.20}$$

The tunneling regime of ionization occurs when γ <1. In the opposite case, γ >1, the multiphoton ionization characteristically occurs [15].

Multiphoton and tunneling ionization should not be understood as two different processes but as two limits of the same process. Ionization character is rather different in these two limits, which MPI rate has a polynomial dependency on the laser intensity I^n, this dependency acquires an exponential character in the tunneling regime (see Eq. (2.19)).

2.3 Strong-Field Approximation

The Strong-Field Approximation (SFA) represents the analytical method for the treatment of the interaction of nonperturbatively strong laser fields with atoms and molecules [76]. It assumes that the initial bound state of the atom or molecule is unaffected by the laser field while the final state, which is in the continuum, is not affected by the presence of the atomic potential, and the ejected electron dynamics is dominated by the laser field. The SFA is known to be gauge-dependent [77, 78]. In nonrelativistic quantum mechanics, when the dipole approximation is adopted, the interaction of an atom with a time-dependent field such as a laser field is usually described in either one of the two gauges: the length gauge *L* or the velocity gauge *V*. Gauge dependence of the SFA is shown probably most clearly in Ref. [77]. The gauges describe the same electromagnetic fields as long as they are related to each

other by gauge transformations. The two gauges give rise to different Hamiltonians in the corresponding TDSE.

Suppose a system in the initial state is described by the TDSE:

$$|\psi_i\rangle = \hat{H}(t)|\psi\rangle. \tag{2.21}$$

$$|\psi(t)\rangle = e^{-i\int_{t_i}^{t}\hat{H}(\tau)d\tau}|\psi_i\rangle = \hat{U}(t,t_i)|\psi_i\rangle \ , \tag{2.22}$$

Where $|\psi_i\rangle$ is the initial state of the system. The Hamiltonian in TDSE can be broken into two parts:

$$i|\psi\rangle = \hat{H}_0|\psi\rangle + \hat{V}|\psi\rangle \ , \tag{2.23}$$

where H_0 is considered as the field-free Hamiltonian and V is the interaction with the laser field. The goal is to relate the solution of H to the solution of H_0. The TDSE for H_0 is:

$$|\psi_i{}^{(0)}\rangle = \hat{H}_0|\psi^{(0)}\rangle \ . \tag{2.24}$$

One can write TDSE:

$$|\psi(t)\rangle = |\psi^{(0)}(t)\rangle + |\psi(t)\rangle = e^{-iH_0 t|\psi_i\rangle} + |\Delta\psi(t)\rangle \tag{2.25}$$

$$|\Delta\psi(t)\rangle = -i\int_{t_i}^{t} dt e^{-i\int_{t}^{t}\hat{H}(\tau)d\tau}\hat{V}(t)e^{-i\hat{H}_0(t-t_i)}|\psi_i\rangle. \tag{2.26}$$

Eq. (2.26) describes the system in the initial state $|\psi_i\rangle$ where the electron populates the ground state until the laser field $\hat{V}(t)$ interacts with the system. After the interaction of the laser with the system, the electron is emitted at time t´ to the continuum.

The transition amplitude a_{fi} for the initially bound state ψ_i to some final continuum state ψ_f can be found as:

$$\begin{aligned} A_{fi}(t) &= \langle\psi_f|\psi_t\rangle = \langle\psi_f|\Delta\psi_t\rangle \\ &= -i\int_{\hat{t}}^{t} dt \left\langle\psi_f\left|e^{-i\int_{t}^{t}\hat{H}(t)d\tau}V(t)e^{-i\hat{H}_0(t-t_i)}\right|\psi_i\right\rangle . \end{aligned} \tag{2.27}$$

One can realize that the ground state and the continuum are the two main participants in the dynamics. Now, while in the continuum the electron is dominated by the laser field, the strong field approximation replaces the propagator term $e^{-i\int_t^t \hat{H}(t)d\tau}$ in Eq. (2.27) by the propagator that includes the laser field exactly and completely ignores the atomic-potential of the system.

$$A_{fi}(t) \sim -i\int_t^t dt \left\langle \psi_f \left| e^{-i\int_t^t \hat{H}_V d\tau} V(t) e^{-i\hat{H}_0(t-t_i)} \right| \psi_i \right\rangle , \tag{2.28}$$

where

$$\hat{H}_V = \frac{\hat{P}^2}{2} + \hat{V}(t) . \tag{2.29}$$

This is the essence of the SFA, where the atomic or molecular potential in the continuum is neglected and the final state of the free electron in the laser field can be described by the Volkov wave function, which takes into account the external field and neglects the atomic field. Furthermore, the Volkov wave function describes explicitly the variation of the electron energy in the laser field [79]:

$$U_V(t,t) = e^{-i\int_t^t H_V(\tau)d\tau} \tag{2.30}$$

In the dipole approximation, the interaction Hamiltonian for an electron with an external electromagnetic field has different forms, depending on the gauge one uses [77]

$$H_x(t) = H_0 + V_x, \tag{2.31}$$

where the subscript x=L, V specifies the gauge. In the dipole approximation, which neglects the space dependence of the electric field and the vector potential, so that E(r, t)→E(t) and A(r, t)→A(t), respectively, the electron-field interaction operator has the following forms in length gauge and velocity gauge:

$$H_x(t) = \begin{cases} -er.E(t) & (x = L) \\ -\frac{e}{m}\hat{P}.A(t) + \frac{e^2}{2m}A^2(t) & (x = V) \end{cases}, \tag{2.32}$$

where $\hat{P}$ represents the momentum operator. The time-evolution operator of the total Hamiltonian satisfies the Dyson equation.

$$U_x(t,t) = U_0(t,t) - i\int_t^t d\tau U_x(t,\tau)H_x(\tau)U_0(\tau,t), \tag{2.33}$$

where $U_0(\tau,t)$ denotes the time-evolution operator of the H_0 Hamiltonian. Using the integral equation for $U_x(t,t')$, one gets for the exact (gauge-invariant) ionization amplitude from an initial ground state $|\psi_i(t)\rangle$ to a final continuum state $|\psi_f(t)\rangle$ of an atom with binding potential I_p, with asymptotic momentum P is:

$$A_P = \lim_{t\to\infty,\ t\to-\infty} \langle\psi_f(t)|U_x(t,t)|\psi_i(t)\rangle, \tag{2.34}$$

The operator $U_x(t,t')$is the time-evolution operator of the atom in the presence of the external laser field.

Both experimental [80] and theoretical [77] studies point out that the length gauge is the proper one to use in the frame of SFA.

2.4 Strong-Field Ionization in Circularly Polarized Field

Ionization of an atomic system in a strong field was described by *Keldysh-Faisal-Reiss* (KFR) theory [78, 81, 82]. It enables to describe the ionization phenomena at the fundamental level, relating it to electron trajectories in the continuum. This theory is based on the method of strong-field approximation. In the circularly polarized intense field, the rules of quantum interference in the ionization process should be considered. The study is analogous to the one developed by Gribakin and Kuchiev [53], and it employs the saddle-point analysis of contributions to the multiphoton transition amplitude.

Consider the removal of a valence electron from an atom by circularly polarized laser field

$$E(t) = F(\cos(\omega t), \sin(\omega t), 0), \tag{2.35}$$

where F is the field strength, and ω is the frequency. The polarization plane is assumed to coincide with the (x, y) coordinate plane and the polarization direction is counter-clockwise. The n photon differential detachment rate has a form [53]:

$$dw_n = 2\pi |A_{Pn}|^2 \delta\left(\frac{P^2}{2} + \frac{F^2}{2\omega^2} - E_0 - n\omega\right)\frac{d^3P}{(2\pi)^3}, \tag{2.36}$$

Atomic units are used in Eq. (2.36). Here $E_0 = -k^2/2$ is the energy of the initial bound state, P is the momentum of the emitted electron, A_{Pn} is the transition amplitude to the final state. The term $\frac{F^2}{2\omega^2}$ corresponds to the ponderomotive shift of the detachment threshold. The energy in the final state is determined by the energy conservation rule represented by the δ function in Eq. (2.36), the wave function electron propagation can be describe by the Volkov wave function. In the length gauge, the transition amplitude can be expressed as:

$$A_{Pn} = \frac{\omega}{2\pi}\int_0^{2\pi/\omega}\left(E_0 - \frac{(P+k_t)^2}{2}\right)\phi_0(P+k_t) \times exp\left\{\frac{i}{2}\int^t [(P+k_t)^2 - 2E_0]dt\right\}, \tag{2.37}$$

where $k_f = \int^t dt F(t)$ is the classical electron momentum due to the laser field and ϕ_0 is the Fourier transform of the initial electron wave function. More details about Eq, (2.37) can be found in Ref. [53]. The integrand function in Eq. (2.37) can be calculated analytically by using the method of steepest descents. Evaluating the integrand of Eq. (2.37) at the saddle point, substituting the transition amplitude A_{Pn} into Eq. (2.36) and integrating the latter over the coordinate P of the momentum space, for the n photons differential ionization rate in the length gauge one obtains [80]:

$$\frac{dw_n}{d\Omega} = \frac{A^2\omega^2}{8\pi^2}(2l+1)\frac{(l-|m|!)}{(l+|m|!)}\left|P_l^{|m|}(i\frac{p}{k}sin\theta)\right|^2 \times \frac{\left(\eta-\sqrt{\eta^2-1}\right)^{2n}}{\sqrt{\eta^2-1}Fcos\theta}\left[\frac{\sqrt{k^2+p^2sin^2\theta}}{\frac{F}{\omega}\left(\eta+\sqrt{\eta^2-1}\right)-pcos\theta}\right]^{2m} \times exp\left[2Fpcos\theta\sqrt{\sqrt{\eta^2-1}/\omega^2}\right], \quad (2.38)$$

where A is the normalization factor, l and m are the angular momentum quantum numbers, $p=\sqrt{2(n\omega-F^2/\omega^2+2E_0)}$ is the photoelectron momentum determined by the energy conservation rule, θ is the angle of electron emission with the respect to the polarization plane, $\eta = n\omega^2/(Fpcos\theta)$, and $p_l^{|m|}(Z)$ is Legendre polynomial. Eq. (2.38) is used in section 5.2.1 to simulated photoemission spectra generated by a strong circularly polarized laser field.

2.5 Electron Dynamics in a Laser Field

In the strong field regime, the interaction of the emitted electron with the parent core can be neglected in the continuum state. The electron motion in this state, thus, is completely governed by the external field and can be described (semi) classically. The classical analysis of electron trajectories in ac-field can be applied to derive several fundamental features of the ionization process, such as the energy cut-offs of ATI and HATI electrons. The equation of motion of a free electron in the harmonic electric field has the form:

$$\ddot{x} = \frac{e}{m_e}E(t), \quad (2.39)$$

where m_e is the electron mass and $E(t)$ the time oscillating electric field.

$$E(t) = F(t)\sin(\omega t) = F_0 . f(t)\sin(\omega t) \quad (2.40)$$

Here ω is the carrier frequency of the laser pulse, F_0 is the field amplitude, and $f(t)$ is the envelope of the pulse. At the moment, we consider a harmonic field and thus, assign $f(t)=1$.

Solving the differential Eq. (2.39), the velocity and position of the electron ionized at time t_0 are given by:

$$\dot{x}(t) = v_0 - \frac{e}{m_e\omega}F_0(\cos(\omega t) - \cos(\omega t_0)), \tag{2.41}$$

$$\begin{aligned} x(t) = x_0 + (v_0 & \\ & + \frac{e}{m_e\omega}F_0\cos(\omega t_0))(t - t_0) \\ & - \frac{e}{m_e\omega^2}F_0(\sin(\omega t) - \sin(\omega t_0)), \end{aligned} \tag{2.42}$$

where x_0 is the initial position of the electron, v_0 is the initial velocity of the electron. Since it is natural to assign the origin of the spatial coordinate to the position of the atom and the ionized electron appears at t_0 as a free particle in the vicinity of the atomic core, one can consider that $x_0=0$

The electron kinetic energy T can is given by:

$$T(t) = \frac{1}{2}m\dot{x}(t)^2. \tag{2.43}$$

Substituting Eq.(2.41) into Eq.(2.43) and averaging over the optical cycle we obtain:

$$\begin{aligned} \int_{t=t_0}^{t_0+2\pi/\omega} dt\,\frac{T(t)}{2\pi/\omega} & \\ = \frac{1}{2}m_e v_0^2 + \frac{1}{4}\frac{e^2F_0(t_0)^2}{m_e\omega^2} + \frac{1}{2}\frac{e^2F_0(t_0)^2}{m_e\omega^2}cos^2(\omega t_0) & \\ - \frac{1}{2}\frac{eF_0(t_0)}{\omega}\cos(\omega t_0), & \end{aligned} \tag{2.44}$$

The first term in Eq. (2.44) represents the initial kinetic energy of the electron T_0 acquired in the ionization event. The second term represents the ponderomotive energy U_p, representing the mean kinetic energy of the electron quiver motion. The third term in the Eq. (2.44) is phase dependent and corresponds to the drift energy of the electron gained in the laser field. The fourth term is called the cross term and is dependent on the initial velocity v_0 acquired in the ionization process.

Eq. (2.44) can be expressed in term of U_p:

$$T = T_0 + U_p + 2U_p cos^2(\omega t_0) - 2\sqrt{2U_p T_0}\cos(\omega t_0) \tag{2.45}$$

As discussed above, insufficiently strong laser field ionization has tunneling character. The electron tunnels through the potential barrier created by the superposition of the atomic and external field potential. As a result, it arises as a free electron with zero kinetic energy. Therefore, we will consider that the electron initial energy T_0 is equal to zero.

Eq. (2.45) allows to make some fundamental conclusions about the electron dynamics after the ionization process. First, the kinetic energy of the electron depends on the phase of the laser field ωt_0 at the moment of ionization. Second, one can conclude about the maximum value of the drift energy, which is called the cut-off energy of the direct ionization process. Here, one should distinguish between the two pulse regimes discussed in section 2.2. In the short pulse regime, the electron ponderomotive energy (the second term in Eq. (2.45) is not conservative and this energy is transferred back to the electromagnetic wave. In this case, only the third term in Eq. (2.45) defines the kinetic energy. It has the maximum value of $2U_p$ when ωt_0=0. This constituted the classical cut-off of ATI spectrum for short pulses. In the long pulse regime, the electron ponderomotive energy is converted to its drift energy and thus, the maximum electron drift energy for this regime is $3U_p$.

Figure 2.9 shows the electron trajectories calculated for a different phase of the laser cycle ωt_0, at which the electron is created as a free particle due to the tunneling ionization. Each trajectory represents the time dependency of the electron coordinate, where the time scale is expressed in terms of the phase of the electric field oscillating, and the coordinate is expressed in terms of the amplitude of the electron quiver motion $eFo/m_e\omega^2$, which can be inferred from Eq. (2.42). The trajectories are considered for the range of initial conditions where the electron is ionized within the first half of the optical cycle, $0 \leq \omega t_0 \leq \pi$. One can see from Figure 2.9 that electrons ionized in the first quarter of cycle travels away and do not return to the origin.

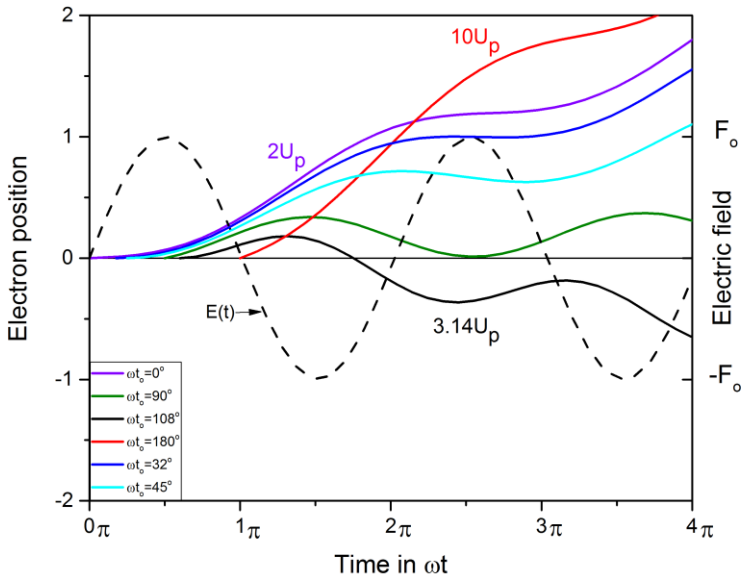

Figure 2.9. Electron trajectories represented by the dependency of the electron coordinate on the laser cycles phase ωt. The trajectories are calculated for different phase ωt_0 of the electron appearance as a free particle and assuming its initial velocity to be zero (tunneling ionization). The violet curve represents the trajectory corresponding to the maximum drift energy of $2U_p$. The black solid curve represents the trajectory with the highest recollision energy of $3.17U_p$. The red curve shows the electron trajectory after recollision which corresponds to the highest possible drift energy of 10 U_p acquired in the high order ATI process. The oscillating laser field is depicted by the dashed line.

Electrons released from the atom at $\omega t_0=0$, have the maximum drift energy of $2U_p$ and their trajectory is shown by the violet curve in Figure 2.9. This trajectory deviates the most from the zero position coordinate. If electron scattering is not considered (see discussion below). The trajectories with the starting point between $\omega t_0 = \pi/2$ and $\omega t_0=\pi$ return to the original atom.

Among these, there is a trajectory corresponding to the maximum electron velocity at the return moment. It is characterized by the maximum slope (tangent) at the intersection point with the abscissa axis in Figure 2.9. The initial condition for this trajectory can be found from numerical solution of Eq. (2.41) and (2.42). As a result, we obtain that electron created at $\omega t_0 = 108^o$ return to the parent ion with the maximum kinetic energy of $3.17U_p$ (this trajectory is shown by the black curve in Figure 2.9). This result is important for the discussion of high–order harmonic generation in section 2.6.

When the electron returns back to the core, it can also be scattered on the residual ion. This can lead to gain an additional energy from the electromagnetic field, as can be derived from the trajectory simulation. The highest energy gain occurs when the electron is scattered back with respect to its incident direction before recollision. It should be noted that the collision is considered to be elastic so that the electron velocity is preserved and only the direction of the motion instantly changes. If the incident direction was opposite to the external field force, after the back-scattering event the force is applied along the direction of motion and the electron is accelerated to a higher velocity. A numerical analysis of the electron trajectories with elastic scattering taken into account is presented in detail in Ref [67, 83]. As a result, it was shown that backscattered electrons can acquire a kinetic energy of up to $\sim 10U_p$. This value constitutes the cut-off of the high-order ATI process. The corresponding trajectory is presented by the red curve in Figure 2.9.

2.6 High-Order Harmonics Generation

High- harmonic generation (HHG) occurs in the strong-field regime, where the laser field is sufficiently strong to ionize atoms or molecules. The strong nonlinear interactions can lead to the generation of high harmonic orders which is an extreme form of nonlinear frequency conversion. The interaction of light and matter is ruled by the Schrödinger equation, which is linear for the wave function but nonlinear in the response of the wave function to perturbations [84]. The equation describes the nonlinear effects expressed as:

$$P(t) = \varepsilon_o(\chi^1 E + \chi^2 E^2 + \chi^3 E^3 + \cdots), \quad (2.46)$$

where *P(t)* is the is the polarization of the medium, *E* is the electric field, χ^1 is the linear susceptibility coefficient and the coefficients χ^n (n= 2, 3, …) are the n^{th} order susceptibilities of the medium. The presence of a term with χ^n is generally referred to as an n^{th} order nonlinearity [84].

The first harmonics generation was first observed in 1961. The Laser beam at 694.3 nm wavelength and of 10^6 W/cm^2 intensity was focused into a quartz crystal to generate a second harmonics [85]. In 1967, the observation of the third harmonics generation was performed by New and Ward [86]. The fifth harmonics generation experiments were carried out by D. I. Metchkov et al. [87] with long pulse infrared lasers. The generation of 9^{th} and 11^{th} and 15^{th} harmonics of iodine laser radiation was performed by J. Wildenauer [88]. J. Reintjes et al. [89] have achieved the generation of the XUV radiation of 5^{th} and 7^{th} harmonics in a rare gas. In 1983, the experiment was done with a use of 248 nm laser wavelength. The beam was focused into helium gas jet to generate the 7^{th} harmonic [90].

The development of lasers of short pulse duration and high intensities has opened the door to achieve high-order harmonics. The 17^{th} harmonics was produced by intense ultraviolet 248 nm radiation of 10^{15}–10^{16} W/cm^2 intensity in neon vapor [91]. Li et al. [92] used laser wavelength of 1064 nm, a pulse duration of 30 *fs* and intensity of 3×10^{15} W/cm^2 to generate the 21^{st} harmonics in xenon 29^{th} harmonic in krypton, and 33^{rd} harmonic in argon. Miyazaki and Sakai [93] observed the 37^{th} harmonics in neon and 41^{st} harmonics in helium by using of 800 *fs*, 616 nm laser, and intensity of 2×10^{14} W/cm.

The HHG in the strong-field regime can be described by using the 'three-step model'[94, 95]. The process is depicted in Figure 2.10 and can be represented by following steps [84]:

a) Tunnel-ionization: the electron is released from the atom near the peak amplitude of optical field (see Figure 2.10 (a)). The laser field suppresses the Coulomb potential and the electron can tunnel out of the atom.

b) Electron acceleration: the subsequent motion of the ionized electron in the oscillating electromagnetic field. The electron is assumed to be born with zero initial velocity and is subsequently accelerated by the laser electric field, in the course of which the electron acquires significant kinetic energy (see Figure 2.10 (b)).

c) The recombination: when the optical field reverses the direction (see Figure 2.10 (c)), the accelerated electron is driven back to the core where it can recollide with the parent ion. The accumulated energy resultant from the recombination process is emitted in the form of radiation. The frequency of the emission corresponds to the kinetic energy of the electron, with added energy of ionization.

It is assumed that the HHG process is driven by an optical field with linear polarization pointing in the x-direction. The Coulomb potential exerted on the electron by an ion is negligible due to the suppression of the Coulomb potential by the laser field.

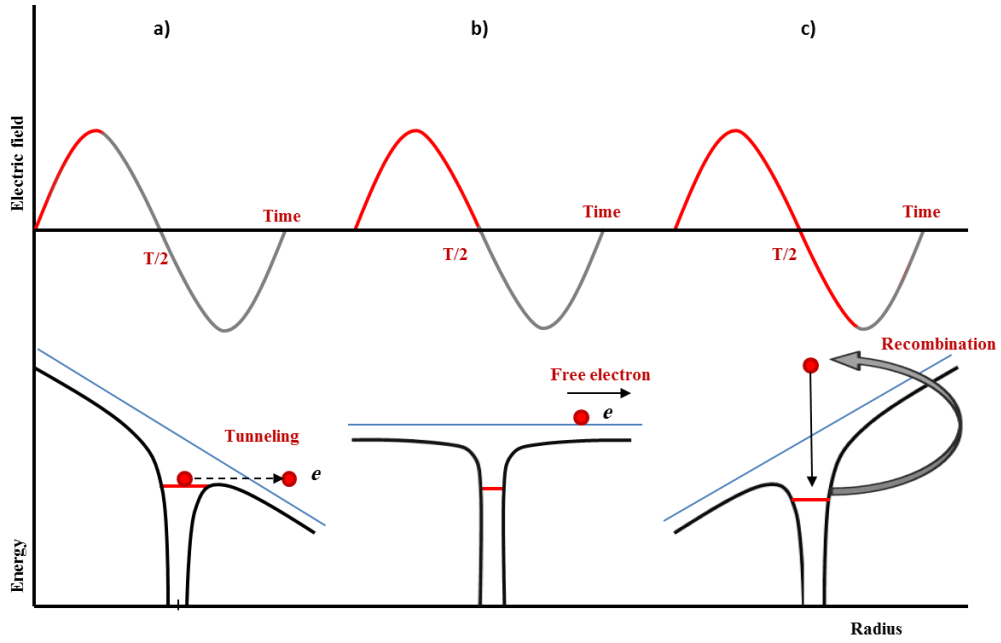

Figure 2.10. Three-step model: Laser field suppression Coulomb potential and electron tunnel out of the atom a), free electron gains the momentum in the laser electric field (b), electron recombines with parents ion and emit a photon of high energy (c).

The recombination process of the electron with parent ion produces photons emitted with a continuous distribution of frequencies, not at discrete harmonic frequencies. An effective "harmonic order" defined as the angular frequency of the emitted photons to that of the pump beam [15]:

$$q = \frac{\Omega}{\omega}, \tag{2.47}$$

Where Ω and ω are the angular frequencies of the emitted photons and for the pump beam, respectively. The harmonics frequencies Ω have the odd multiples of the laser angular frequency (q=3, 5, ...) because of the inversion symmetry of the atom in the field. The maximum energy electron gain in the process of recombination due to the quiver motion is $3.17U_p$. Hence, the maximum observable photon energy in this process is:

$$\hbar\omega_{max} = I_p + 3.17U_p. \tag{2.48}$$

Figure 2.11 shows the harmonic spectrum of xenon measured at 1064 nm wavelength. The odd harmonics between 9^{th} and 21^{st} were observed. The laser intensity was approximately 3×10^{13} W/cm^2.

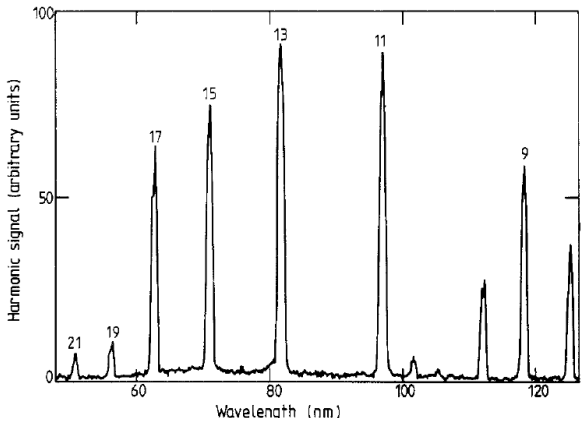

Figure 2.11. Harmonic emission spectrum using xenon gas jet showing all odd harmonics between 9 and 21. The peaks at 101, 112 and 125 nm are the second diffracted orders of the 21^{st}, 19^{th} and 17^{th} harmonics, respectively. The laser intensity was approximately 3×10^{13} W/cm^2 [96].

2.7 Principles of Photoelectron Spectroscopy

Photoelectron spectroscopy (PES) provides key information needed to understand the chemical and physical properties of matter in the gas, liquid, and solid phases. PES experiments from liquids require some special conditions which will be outlined in chapter 3. The principle of PES is based on the photoelectric effect which was detected for the first time by Hertz in 1887 [97, 98]. Phillip and Lenard were first to correctly describe the light-induced electron emission from a metal surface, including the work function that could not be described by the classical wave theory of light [99]. Later, the photoelectric effect was explained in terms of the quantum theory of light by Einstein in 1905 [100, 101]. In 1914, Rutherford found that the kinetic energy of the emitted electrons is determined by the difference between the energy of applied x-ray photons and the electron binding energy [102].

The field of PES has been nowadays tremendously extended to study various properties and process in liquids, solids, and gases of low vapor pressure. It became necessary to extend the PES applications to more complex molecular systems. In particular, organic liquids with low vapor pressures have been studied by means of PES, specially developed to detect electrons emitted from liquid samples [103].

When the light of short wavelength interacts with free molecules, electrons can be emitted from the occupied molecular orbitals in one-photon transition. PES enables to investigate the electrons from different molecular orbitals and provides information about the electronic structure of the atoms and molecules [104]. The law of the photoelectric effect by Einstein is based on energy conservation [100]. The electron kinetic energy can be expressed as:

$$E_{kin} = \hbar\omega - I_p \tag{2.49}$$

The process of one-photon ionization is possible only if $\hbar\omega > I_p$, requiring the application of light of short wavelength. The photoelectron spectrum of a molecule carries the molecular orbitals energy diagram. The spectral information also provides details about the molecular

dynamics and geometrical changes of the molecules when PES is applied in a pump-probe experiment.

2.7.1 The Methods of Photoelectron Spectroscopy

PES experiments consist of the energy measurement of photoelectrons emitted from solid, gas, or liquid samples due to the photoelectric effect. Depending on the energy of applied photons and the character of spectral information, PES studies can be divided into different types.

The angle-resolved photoemission spectroscopy (ARPES) method is typically applied to study the electronic structure of the valence shell. E.g., it enables direct observation of the Fermi surface of crystals. The ARPES provides information on both the direction and the energy of electrons emitted from the valence shell of the sample. When the incident photon energy $\hbar\omega$ is higher than the work function $\emptyset$ of the material, electrons are ejected into the vacuum at different angles. Angle-resolved electron energy analyzer can be used to detect the emitted electrons. In the case of a solid-state sample, the total energy and the momentum component parallel to the surface are conserved, but the momentum perpendicular to the sample surface is not conserved because of the broken translational symmetry along this direction. The ARPES method is rather effective in the study of quasi-2D metals, where the dispersion of electrons perpendicular to the surface of the sample is low [105].

The photoelectron angular distributions (PADs) is method provide information on the molecular orbitals and symmetry from which electron is originated [106]. Within the molecular frame, the symmetries of the emitted electron partial waves are related to the symmetry of the electronic state undergoing ionization. Experimentally, the most influential form of control the PADs experiment is the manipulation of the relative directions of vectors within an atom or molecule and the polarization vector of the ionizing light [107]. The photoemission is, in general, sensitive to the orientation of molecules. Recently the PADs

have been used as probes of other dynamical processes or the spatial distributions of molecules. The method was used to study free molecules in the gas phase and liquid-jet PES to access equilibrium molecular orientation and inter-molecular structure in a solution as well as provide a new window on aqueous-phase chemical reactivity [108].

Another important aspect of PES is the application of x-rays, and the method is then referred to as x-ray photoelectron spectroscopy (XPS). The XPS method is used to study the core-level electrons of the sample. The sample is placed in an ultrahigh vacuum environment where it is exposed to radiation of high photon energy from a monochromatic x-ray source. The energy of the incident photon can be in the soft x-ray range (SXPS method) between 100 to 1000 eV or in the hard x-ray range above 1000 eV [109] these energy ranges can be accessed of synchrotron of free-electron-laser facilities.

When the core electron is removed by the incident x-ray photon, the core hole can be filled by an electron from the outer shell of the atom. The energy of this transition is balanced by the emission of so called Auger electron[110]. Therefore, this method received the name of Auger photoemission spectroscopy. The Auger spectra are element-specific and, therefore, the Auger spectroscopy finds a wide range of application in the material sciences.The method was developed in 1957 to investigate the atomic binding energies [111].

The ultraviolet photoelectron spectroscopy (UPS) employs light source in the vacuum ultraviolet energy range typical source of radiation for UPS is a noble gas discharge lamp. In UPS experiments, the UV light is used to ionize valence shells of atoms and molecules. The incident photons possess energy between 5 to 100 eV [109]. The UPS method was developed by Turner and Al-Jobory [112].

The two-photon photoelectron spectroscopy 2PPS represents the most versatile method for studying the electronic states of solid surfaces [113, 114]. It is applied in time-resolved spectroscopy experiments. This method provides information on the initial density of states below the Fermi level of the studied system [115, 116]. The first pump photon $\hbar\omega_{pump}$ excites

an electron from an occupied state below the Fermi level to an intermediate state between the Fermi and the vacuum level. In the populated intermediate state, the electron can be excited above the vacuum level by absorption of the second probe photon $\hbar\omega_{probe}$.

A rather similar approach is the method of resonance ionization spectroscopy (RIS) where, the photon energy is tuned to resonance with the energy of an intermediate excited electronic state [103, 117]. The photo-transition in the RIS method obeys the angular momentum selection rules of the electronic transitions. It imposes some restrictions in the application of this method. Usually, lower-lying excited Rydberg states are used as the intermediate states in the RIS method.

Zero electrons kinetic energy (ZEKE) approach is one of the PES methods, based on pulsed field ionization. The principle of ZEKE is to detect only the photoelectrons that have been excited to a resonantly excited state [118] and undergo a subsequent ionization transition characterized by the extremely low kinetic energy of photoelectrons [119]. In the ZEKE technique, two lasers of different wavelengths are used. First, the photon energy is tuned to be resonant with the energy of an intermediate state. The second wavelength is chosen to be close to the ionization threshold of the excited states which are detected by pulsed electric field ionization. The technique works extremely well for high-resolution photoelectron spectroscopy.

2.7.2 Time-Resolved Photoelectron Spectroscopy

The photoinduced processes occur on very fast time scales, including molecular dynamics, electron transition, photon absorption and emission, and scattering processes. The time scale of these processes is in the picosecond (10^{-12} s) or femtosecond (10^{-15} s) range. In general, the idea of the time-resolved photoelectron spectroscopy (TRPES) method consists of the application of two light pulses, whereas the reaction is triggered by an initial laser pulse (which establishes the time zero) and the dynamics are probed by a second pulse. The early

experiments with the use of TRPES devoted to the study of the rapid chemical reactions, provided millisecond time resolution [120]. Later, the temporal resolution of the time-resolved spectroscopy measurement has been improved up to microseconds [121]. A better time resolution could be achieved with the development of fast photodiodes and oscilloscopes, which have a temporal resolution in the order of 10^{-10} s [122].

The laser based TRPES method was developed by Haight [123]. The first TRPES experiments of gas-phase with the use of nanosecond and picosecond lasers were performed in the mid-1980, by Pallix and Colson [124]. In early 1990, experiments by Song, et al [125] and by Knee [126] have demonstrated that TRPES with a picosecond resolution could be used to follow intramolecular vibrational relaxation (IVR) in excited electronic states. Another group applied the TRPES method to study the reaction and solvation dynamics of clusters on a picosecond time scale [127, 128].

The development of femtosecond time-resolved technique by Zewail to study gas phase [129], opens the door for new experiments designed to investigate the dynamics of ultrafast processes involving electron transitions and molecular dynamics. The first experiment of femtosecond TRPES of the solid sample was reported in 1993 by Baumert et al. [130]. Later, the technique was used to study the dynamics in polyatomic molecules [131, 132] and the relaxation dynamics of biomolecules [133].

Pump-probe experiment is the basic technique of the TRPES method. To study the dynamical process of a quantum system by the pump-probe technique, first, the system must be perturbed from its equilibrium state (see Figure 2.12).

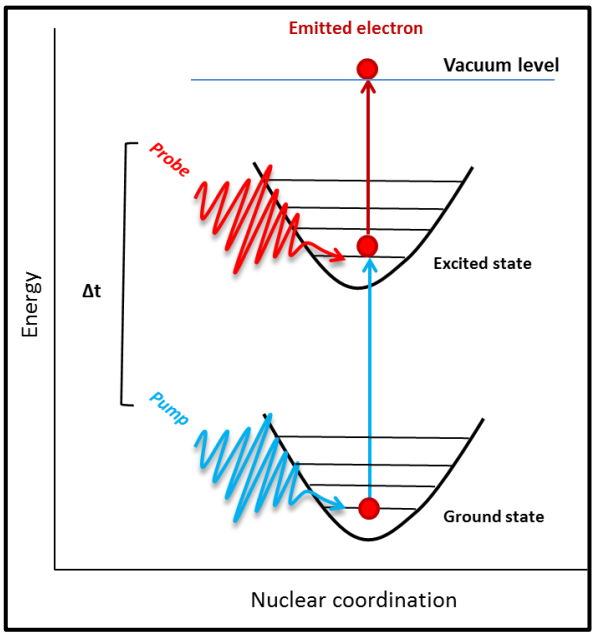

Figure 2.12. Illustration of pump-probe technique.

This is achieved by the pump pulse, which must travel a shorter path in order to interact with the sample first. The energy of the pump photon is tuned to excite a bound electron resonantly to the electronic excited state. In order to excite the electron to the chosen state, it should be possible to control the wavelength, intensity, polarization, and duration of the pump pulse. If the photon energy of the pump beam is equal to the energy difference between the ground state and the excited state, the quantum system absorbs photons of the pump pulse, leading to an increase in the population of electrons in the excited state (see Figure 2.12). Excited electrons absorb photons from the probe beam and, thus, are emitted from the system to vacuum (see Figure 2.12). The time delay between pump and probe pulse can be controlled by changing the path length of one of the pulses. One can summarize that the femtosecond pump-probe experiment represents a sequence of the three steps: (i) the preparation of an excited state by pump, (ii) the dynamical evolution of the quantum system, and (iii) the probing of the nonstationary superposition of states after a certain time of the system evolution [106].

2.8 Space-Charge Effect Induced by a Single Laser Pulse of High Intensity

With the development of the high-intensity lasers and their application in the PES experiments, associated effects caused by space-charge were reported [51, 134, 135]. When ionization by an intense laser field takes place, the large amount of electrons emitted from the sample acquires a spatial charge distribution which changes their kinetic energy measured by the electron detector. If the cloud of the emitted electrons is sufficiently dense, due to the Coulomb interactions, the fast electrons are accelerated by the slow electrons behind them while the slow electrons tend to be decelerated by fast electrons [136]. Coulomb repulsion between the emitted electrons can be a limiting factor for photoemission experiments since, as aforementioned, it changes the kinetic energy and also the angular distribution of the photoelectrons and, in particular, leads to a decrease in the energy resolution.

The space-charge effect (SCE) manifests itself differently in experiments on solid, liquid and gas samples. The atomic or molecular density of the sample determines the density of the emitted electrons. The phase state of the sample also determines the effect of the interaction of photoelectrons with positive ions generated in the sample during the ionization process. In addition, the laser intensity and the absorbance of the laser light in the medium also determine the density of the electrons emitted from the sample. Figure 2.13 depicts the interaction of a laser pulse with gas, liquid or solid phase.

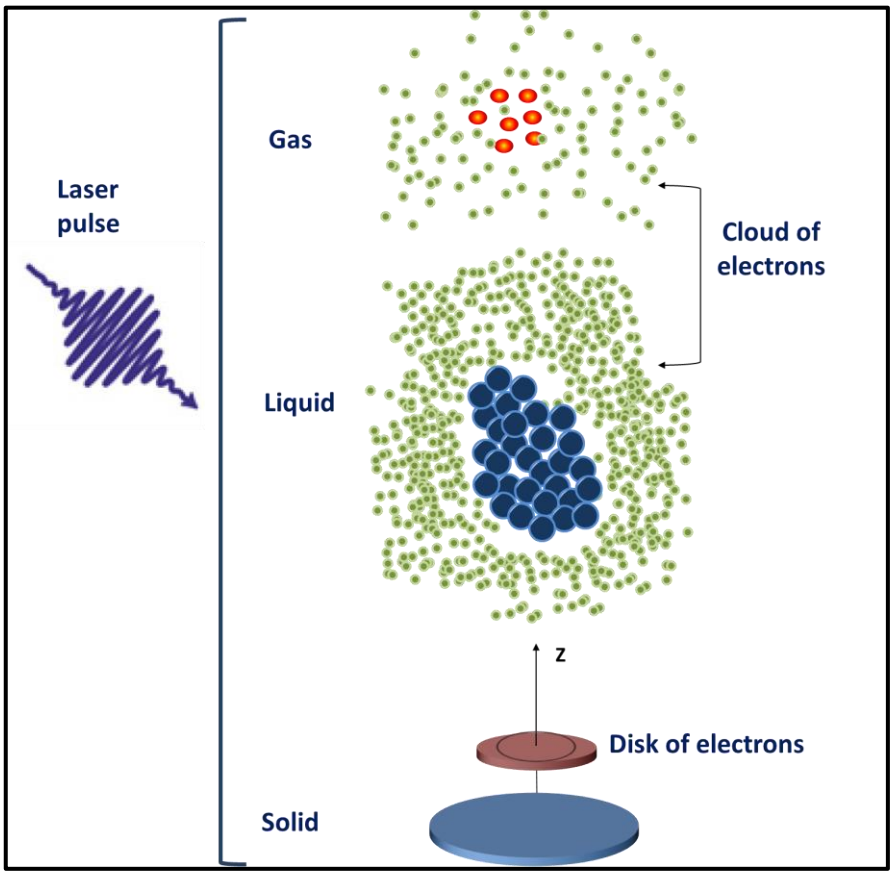

Figure 2.13. Interaction of laser field with gas, liquid or solid phase.

Photoelectrons emitted from a solid sample can be represented by as a quasi-2D disk [52] (see the lower part of Figure 2.13) since they can leave the sample only in the direction perpendicular to the surface. The density of photoelectrons generated from gaseous samples comparably small and electrons can propagate in three dimensions. In this case, the spatial distribution of photoelectrons resembles a 3D cloud. Photoelectrons generated by ionization process of the liquid sample form also a 3D cloud. In the former case, the cloud is characterized by a high electron density due to the high molecular density of the liquid sample.

SCE is caused not only by the electron-electron interaction but also by the electron-positive ions interaction. The latter leads to a reduction of the kinetic energy of the slow electrons. If

the positive electric field is strong enough, it can trap the slow electrons and they will not reach the detector. Thus, the slower electrons are affected stronger by the electric field of the positive ions, while the fast electrons escape the interaction region before a significant positive charge is accumulated in the medium. This explains the reduction in the count rate of the detected slow electrons in single-laser-pulse experiments, as also observed in the present work. Generation of positive ions depends on the physical properties of the sample. In gaseous samples, where the atomic density is low, the number of positive ions created in the ionization process is also low. Accordingly, the effect of the positive ions in the photoemission spectra is weaker. SCE from ionization of gases was reported in numerous experiment [137]. This effect was also widely studied in experiments on strong-field ionization of solids [52], where electrons with kinetic energies exceeding 10 eV were generated from a metal surface. SCE was studied in experiments on multiphoton ionization of metal samples with the use of picosecond [51] and femtosecond [138, 139] lasers. ARPES was applied in Ref. [140, 141] to investigate this effect. SCE induced in solid samples was shown the result in the acceleration of the higher-energy emitted electrons.

Chapter 5 of this thesis addresses the role of the SCE in a single laser pulse experiment, where strong-field ionization of dense gas (vapor) is studied. The experiments carried out by using linearly and circularly polarized light, generate a rather different distribution of the photoelectron kinetic energy spectra (see Chapter 5).

2.9 Space-Charge Effect in Time-Resolved Photoelectron Spectroscopy

The space-charge effect also plays an important role in the TRPES experiments. In this case, two clouds of electrons are generated at different times. The time delay between the pump and probe pulses determine the strength of the Coulomb interaction between the pump and probe clouds of generated electrons. Electrons lifted just above the vacuum level by a lower energy photon of the pump beam form a cloud of slow electrons. Photons of the probe beam

ionize the sample and create a cloud of fast electrons. The clouds are different in the electronic density due to the difference in the intensity of the pump and the probe beams. Figure 2.14 depicts the interaction of the pump and the probe pulses with the liquid sample. The lower part of the Figure shows the pump pulse interacting with the sample first (at positive time delay). It generates a cloud of the high-density electrons. At negative time delay, the probe pulse interacts with the sample first and generates a cloud of low-density electrons (see the upper part of Figure 2.14). The sequence of the laser pulse (which pulse interact the sample first) plays a significant role in the manifestation of the SCE, as will show in Chapter 4.

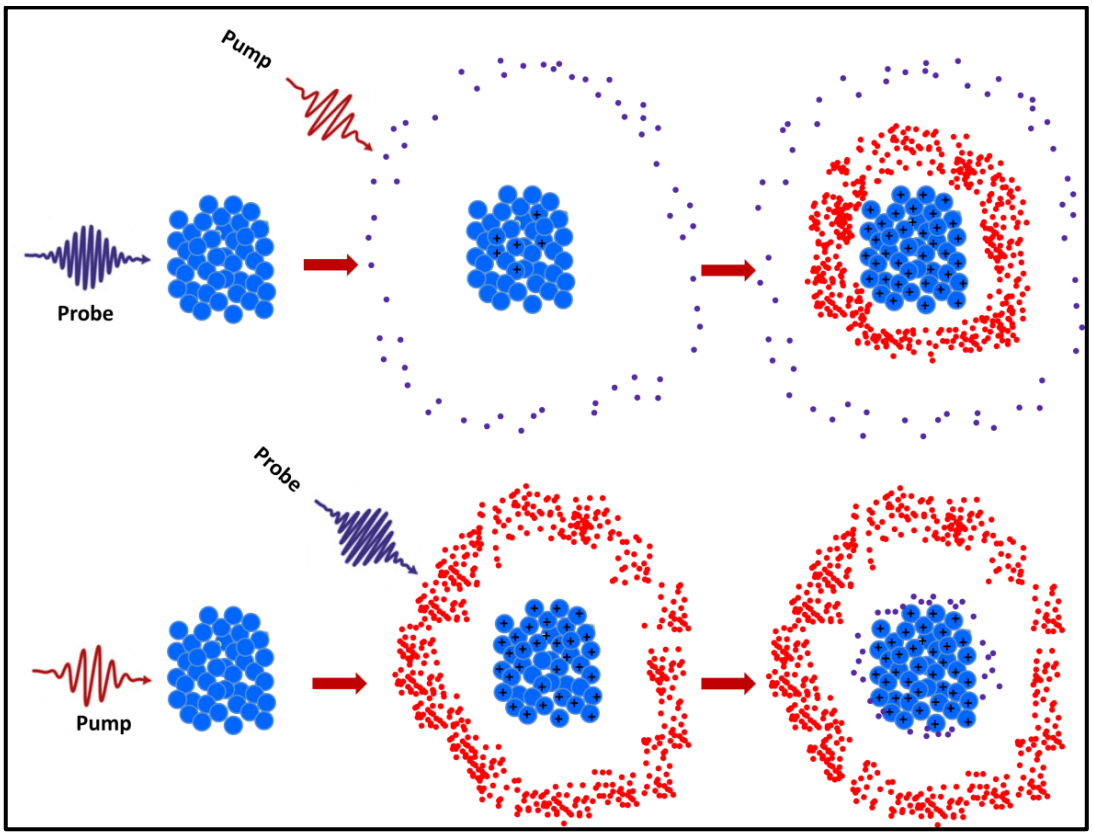

Figure 2.14. Illustration of pump-probe interaction with the liquid sample. The lower panel depicts the "pump → probe'' sequence, and the upper panel shows the ''probe → pump''sequence.

SCE was observed in pump-probe experiments on the solid-state samples, where soft x-ray [142, 143] or hard x-ray [52] radiation from a free-electron laser or from a synchrotron light source [144] was used to probe a sample irradiated by a laser pulse. It was found that at start pump-probe delays, the formation of laser generated electron cloud leads to acceleration of electrons ionized by high-energy photons.

A comprehensive discussion of the charge dynamics due to the interaction between the pump and the probe photoelectron clouds emerging from a solid state surface is presented in Refs. [52, 143, 145]. SCE was also observed in the experiment on the laser-assisted photoelectric effect (LAPE) induced at a solid surface [71]. It was also studied by the ZEKE method, applied to study ionization of gaseous media [137], and in a femtosecond 2PPE experiment, on a solid sample [50].

Chapter 4 presents results of this work, where the SCE in time-resolved PES study is considered for a liquid sample. One can anticipate some difference in the SCE manifestation as compared to pump-probe experiments on solid samples. As discussed above, the interaction of the laser pulse with the sample initiates two effects related to the formation of space charge: *positive and negative charge effect*. It will be discussed in Chapter 4 that the two effects of space charge appear differently in the pump-probe experiment. While the interaction of negatively charged particles leads to acceleration of faster electrons, the positive charge effect results in electron deceleration. The negative charge effect is expected to be similar in solids and liquids since the interaction of pump and probe electron clouds takes place in a vacuum (free space) in both cases.

However, the carrier mobility in a metal or semiconductor sample is much higher than in a liquid sample. This implies that the induced positive charge is preserved for a much longer time at the liquid surface, while a fast charge recovery takes place at the solid surface. Therefore, the positive space charge effect is expected to be much stronger in pump-probe experiments on liquids as compared to experiments on solids.

2.10 Electronic Structure of Water

Since water represents one of the most important compounds in nature, the electronic structure of water molecules in a gas, liquid, and solid phase was in the focus of investigations for many years. The electronic properties of water are extremely interesting since water can influence many electrochemical processes of dissolved compounds. Various methods were applied in the studies on the electronic structure of isolated water molecules. Among these are the method of x-ray photoelectron spectroscopy [146, 147], and x-ray absorption spectroscopy. The electronic structure of liquid water and water clusters was widely studied as well. Here the use of x-ray absorption spectroscopy [148], x-ray Raman scattering [149], and x-ray emission [150-152] received the greatest success. In particular, these methods were applied in the studies of the hydrogen bonds [146, 150, 153]. The time-resolved x-ray absorption spectroscopy has emerged as an important method to study the structural dynamics in the liquid water [154]. [155]. The photo-ionization of liquid water by ultrashort laser pulses has been under investigation by several groups for many years, see Refs. [156-161]. Recently, the development of femtosecond laser technology provide the opportunities to apply the method of time-resolved photoelectron spectroscopy for study molecular dynamics in gaseous and liquid water [20, 45]. One interesting aspect of this dynamics in liquid water is the formation of solvated electrons in the process of ionization, which occurs due to the reorganization of the hydrogen-bond network of water molecules leading to the formation of the solvation shell. The dynamics of bulk and surface solvated electrons were studied in Refs. [162, 163].

The water molecule consists of two light hydrogen atoms and a relatively heavy oxygen atom. The H_2O molecule, thus, possesses 10 electrons: 8 electrons originate from the oxygen atom and 1 electron originates from each hydrogen atom. The electronic structure of H_2O has the configuration:

$$(1a_1)^2(2a_1)^2(1b_2)^2(3a_1)^2(1b_1)^2, \tag{2.50}$$

where only the occupied molecular orbitals of the ground state are indicated. The diagram of the energy-level structure of the water molecules is depicted in Figure 2.15 (a), where one can see how atomic orbitals of oxygen and hydrogen contribute to the different molecular orbitals, the resulting electron density distribution of molecular orbitals is shown in Figure 2.15 (b). Here, the molecular orbitals are depicted in a sequence according to their energy, with the lowest energy orbitals in the bottom. The highest occupied molecular orbital (HOMO) in the water molecules is $1b_1$. The two lowest unoccupied molecular orbitals (LUMO) are $4a_1$ and $2b_2$.

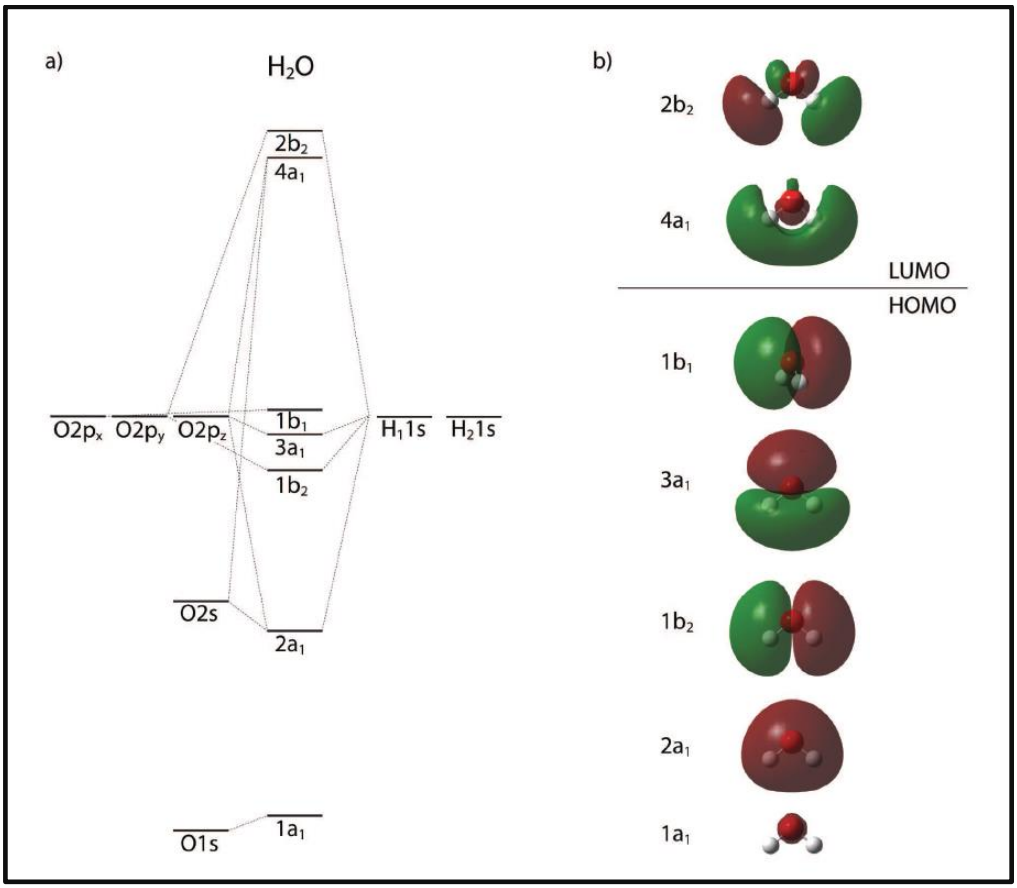

Figure 2.15. a) Molecular orbital diagram of H_2O. b) Occupied and the first two unoccupied molecular orbitals of a single water molecule. Orbitals were calculated using the Gaussian 03 program [164].

The application of HHG light enables to access the HOMO and a few lower-energy orbitals in a PES experiment. A photoemission spectrum of gas-phase water obtained with the use of the 21st harmonics (32.55 eV photon energy) is shown in Figure 2.16. The ionization yield from the $1b_1$, $3a_1$, and $1b_2$ orbitals governs the spectrum. The contributions from the $3a_1$ and $1b_2$ orbitals have a broad-band shape due to a large number of vibrational states. A similar spectrum was recorded in a PES experiment with the use of synchrotron radiation [146].

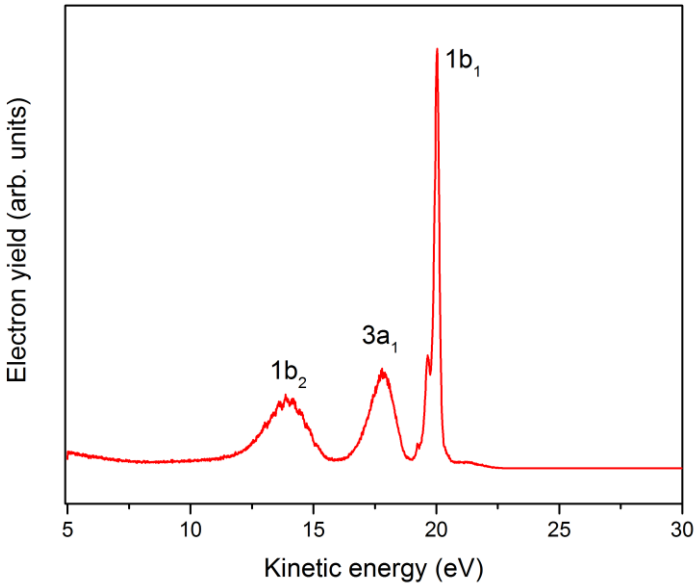

Figure 2.16. The kinetic energy spectrum of water in gas phase obtained from ionization by XUV photons. The spectrum shows $1b_1$, $3a_1$, and $1b_2$, ionization contributions of water in the gas phase.

The electronic structure of water in liquid phase is different from the gas phase. First, the formation of the hydrogen bonds between molecules leads to the small spectral shifts and broadening in the band structure of the orbitals. The larger contribution to the shift is

however due to the long-range electronic polarization of liquid water. This will be detailed in section 4.3. The principle difference consists of the existence of a conduction band in liquid water which lies below the vacuum level. This has been observed in the experiment of two-photon ionization of liquid water [165].

The electronic properties of bulk water such as the conduction band edge and the associated band gap, and the vacuum level position have been studied in Refs. [166, 167]. The method of transient absorption spectroscopy was used to study the geminate recombination kinetics of solvated electrons following two-photon ionization of liquid water at several excitation energies [165, 168, 169]. The aforementioned properties are essential for this work since the character of the multiphoton ionization process induced by the pump beam is influenced by the presence of the conduction band in the liquid water.

2.11 The Molecular Structure of Potassium Ferrocyanide

Since the aqueous solution of potassium ferrocyanide is used as a sample in the present work, the electronic structure of this metal coordination complex will be considered next.

Potassium ferrocyanide, $K_4[Fe(CN)_6]^{4-}$, is an inorganic salt compound. In aqueous solutions this compound dissociates, leading to the formation of four positively charged potassium ions and an anion of the metal coordination complex carrying a negative charge of 4-:

$$K_4[Fe(CN)_6] \rightleftharpoons 4K^+ + [Fe(CN)_6]^{4-} \tag{2.51}$$

The coordination complex consists of the central iron atom which is bonded with six CN ligands (see Figure 2.17). A ligand is an ion or molecule that is bound to the central metal (atom) to form a coordination complex.

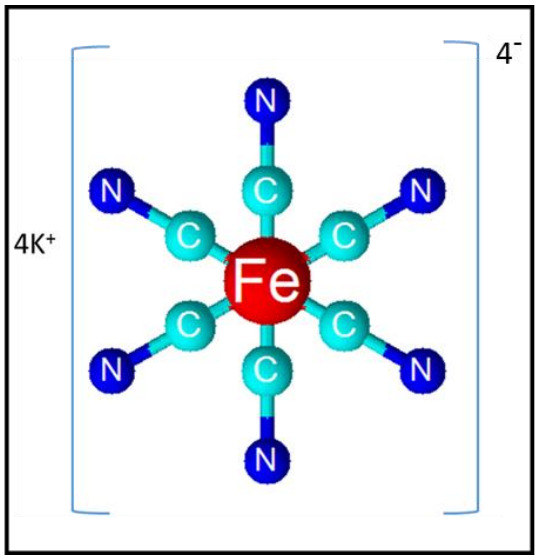

Figure 2.17. The structure of potassium ferrocyanide $K_4[Fe(CN)_6]^{4-}$ molecule.

Each ligand carries a single negative charge. Since only four positive charges can be donated from the four potassium atoms, two negative charges are donated from the central iron atom. Thus, the iron center possesses a positive charge of 2+.

The $[Fe(CN)_6]^{4-}$ complex may undergo oxidation, resulting in the formation of ferricyanide where the iron atom carries a positive charge of 3+:

$$[Fe^{2+}(CN)_6]^{4-} \rightleftharpoons [Fe^{3+}(CN)_6]^{3-} + e^- \tag{2.52}$$

Figure 2.18 shows the molecular orbitals of $K_4[Fe(CN)_6]^{4-}$ complex, obtained from the calculations using the density functional theory [170]. The five atomic iron 3d orbitals are split due to the ligand field into two e_g and three t_{2g} orbitals. The e_g is a high-spin-state is formed from the mixing between Fe-$d_{x2-y2,}$ Fe-d_{z2}, with CN-σ donor and CN-σ acceptor orbitals.

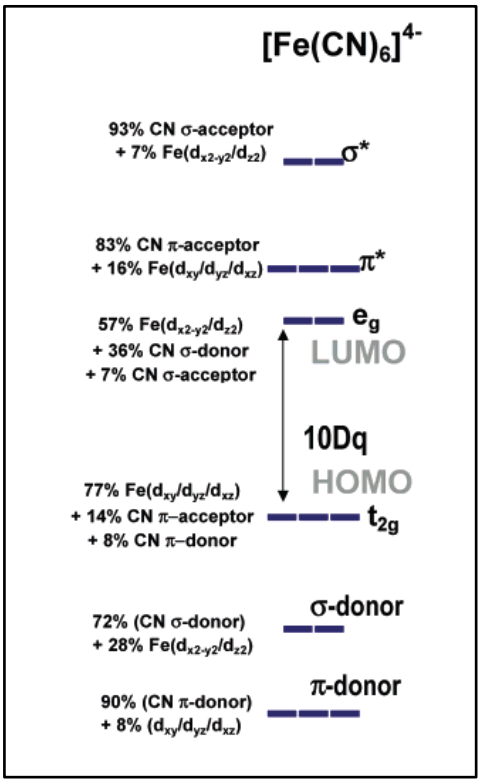

Figure 2.18. Molecular orbital diagrams of potassium ferrocyanide $K_4[Fe(CN)_6]^{4-}$ calculating using density functional theory [170].

The t_{2g} is a low-spin-state, results from the π back-bonding interaction between Fe-d_{xy}, Fe-d_{yz}, and Fe-d_{xz} with CN-π donor and CN-π acceptor orbitals. The ligand field splitting energy 10Dq was calculated 4.19 eV. The percentage ratio of the orbitals contributions is calculated by using density functional theory is shown in Figure 2.18 [170]. In the ground state of ferrocyanide, the six electrons of Fe^{2+} occupy the three t_{2g} orbitals representing the HOMO state of the complex. This state has a binding energy of 6.11 eV [171]. The next lower-lying state is the $\sigma(e_g)+\pi$ state representing mainly CN-donor contribution [172].The electronic energy-level structure of ferrocyanide was studied Seidel *et al.* [171] in a PES experiment with the use of synchrotron radiation.

Chapter 3

Experimental Setup

This chapter describes in detail the experimental setup used in the femtosecond time-resolved pump-probe measurement. Section 3.1 introduces our femtosecond laser system, including the high harmonic generation and the third harmonic generation. The UV light was used to excite electrons from a sample to an excited state, consequentially, the electrons are ionized by an XUV light. Section 3.2 describes the interaction region, including the characterization of the liquid microjet setup and the time-of-flight electron spectrometer. Section 3.3 explains the spatial and time overlaps of the pump and probe pulse. The time resolution of the pump and probe pulse giving rise to a photoelectron signal, which is analogous to the cross-correlation signal. Section 3.4 of this chapter is to explain the sample preparation.

For a single laser pulse of high intensity experiment, the optical parametric amplifier (OPA) was used to generate the near-infrared light. Section 3.5.1.1 describes the OPA structure. Section 3.5.1.2 explains the optical setups of linear and circular polarization light control. Section 3.5.2. depicts the design of the time-of-flight electron spectrometer was used in the measurement of high intensity single laser pulse.

3.1 Laser Setup

Our laser system consists of femtosecond Ti: sapphire laser producing 2.5 mJ, 800 nm pulses at the repetition rate of 5 kHz and with duration of 25 *fs* used to generate the UV pump and XUV probe beams. Approximately 60% of the laser output was used for the frequency upconversion by the high harmonic generation in an argon filled cell to generate XUV pulses. The rest 40% is used for generation of the third harmonic.

3.1.1 High Harmonic Generation

This section is based on results published in (5) (J. Metje *et al.*). Optics Express, Vol. 22, Issue 9, pp. 10747-10760 (2014).

The setup for high harmonic generation HHG is shown in Figure 3.1. A gas cell filled with argon was placed into a vacuum chamber. A focusing lens of 600 mm focal length was mounted on a translation stage in order to adjust the position of the pump laser focus in front of the argon cell. The polarization plane and the intensity of the pump beam were controlled by a λ/2 wave plate (W) and a polarizer (Z), respectively, placed before the focusing lens (L). With the use of the focusing lens, a peak intensity of 6×10^{14} W/cm^2 can be reached in the focus of the pump laser beam. The saturation of ionization in the argon gas was avoided by reducing the pulse energy of the pump laser beam. The gas cell was designed as a cylinder hollow rod of 16 mm length and was sealed with aluminum foil. The focused pump laser made an entrance and exit holes in the aluminum foil by itself. A dosing valve was used to adjust the flow rate of the argon gas into the cell. The XUV photocurrent was detected by a moveable photodiode (P) placed behind the monochromator. The typical pressure inside the gas cell was about 20 mbar during the operation.

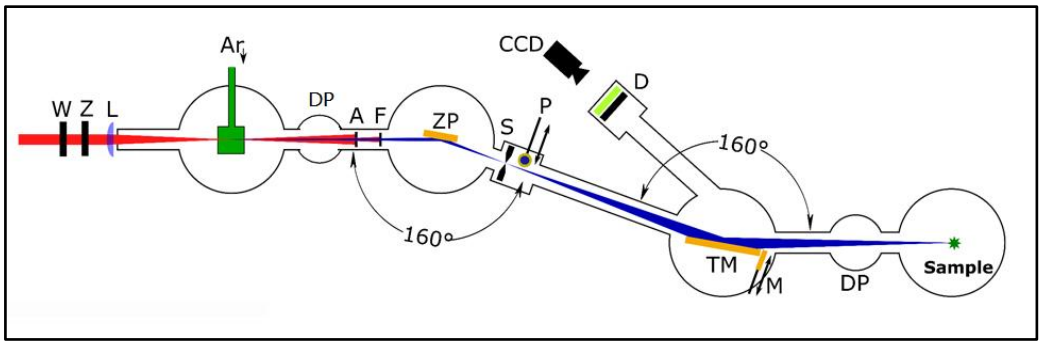

Figure 3.1. Schematic view of the HHG setup. Notations: (W) wave plate, (Z) polarizer, (L) lens, (DP) differential pumping stage, (A) aperture, (F) Al foil, (ZP) zone plate, (S) slit, (P) movable photodiode, (TM) toroidal mirror, (M) movable plane mirror, (D) position-sensitive detector [47].

A zone plate (ZP) monochromator is used to select the high harmonics. The monochromator consists of three gold-coated zone structures made on a single silicon substrate [47]. The several ZP structures were designed to select the 17^{th}, 21^{st}, and 25^{th} harmonics of the XUV beam, respectively (see Figure 3.3). The ZP substrate was mounted on a motorized stage that could be adjusted in three transnational directions and three rotational axes. The adjustment precision is 0.1 μm and 2 μrad, respectively. The ZP was mounted in a vacuum chamber. The ZP chamber was connected to a differential pumping stage (DP) to provide a low pressure of 10^{-8} mbar in the ZP chamber (see Figure 3.1). In front of the ZP, a thin aluminum foil (F) of 150 mm thickness was used to filter out the residual infrared pump beam. The foil has been prevented from melting by using an aperture (A) of 2 mm diameter placed before the foil to block the main part of the pump beam. This aperture reduced the divergence of the incident XUV beam at the ZP position down to 3.3 mrad.

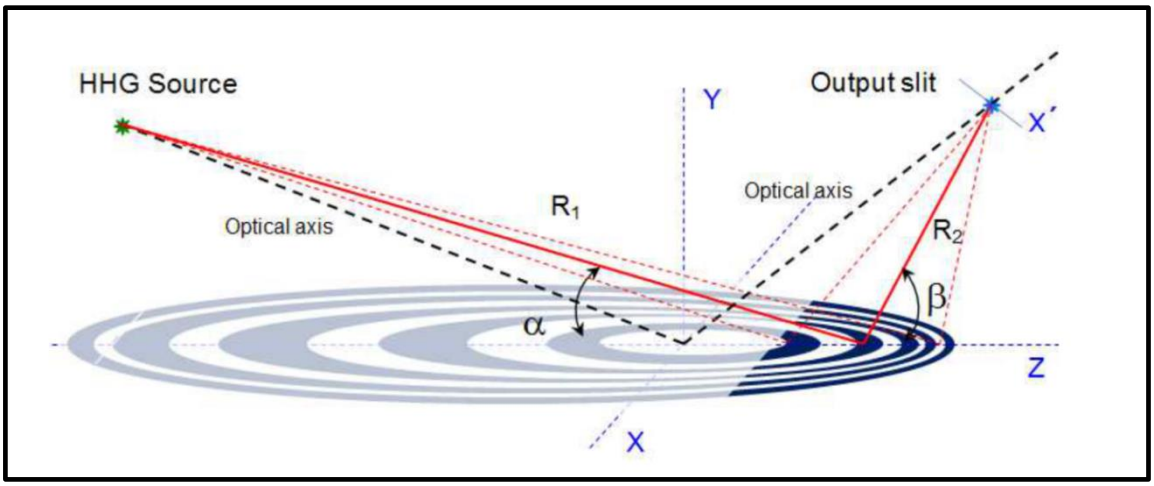

Figure 3.2. The optical design of the reflection zone plate. The area of use is shown by dark-blue color [47].

Figure 3.2 shows the optical design of the reflection zone plate. The ZP has full elliptical mirror structure. The center of the ZP possesses high dispersion and reflection

characteristics, which represent a projection of the transmission Fresnel zone plate on the plane mirror surface [173]. If the off-axes section of the ZP illuminated by XUV beam (see Figure 3.2 dark-blue color), the incident beam onto this section is reflected and focused along the optical axis. The off-axes section represented an ideal monochromator. The harmonic of interest was deflected in the first diffraction order at an angle of 20^{o} and focused behind the ZP at a focal length of 350 mm. The other harmonics are focused differently into a plane behind the ZP. In order to select the required harmonic from other harmonics reflected and focused differently, a slit (S) with a variable width is positioned at the ZP focal point (see Figure 3.1). The width and the longitudinal and transversal positions of the slit could be adjusted with micrometer precision.

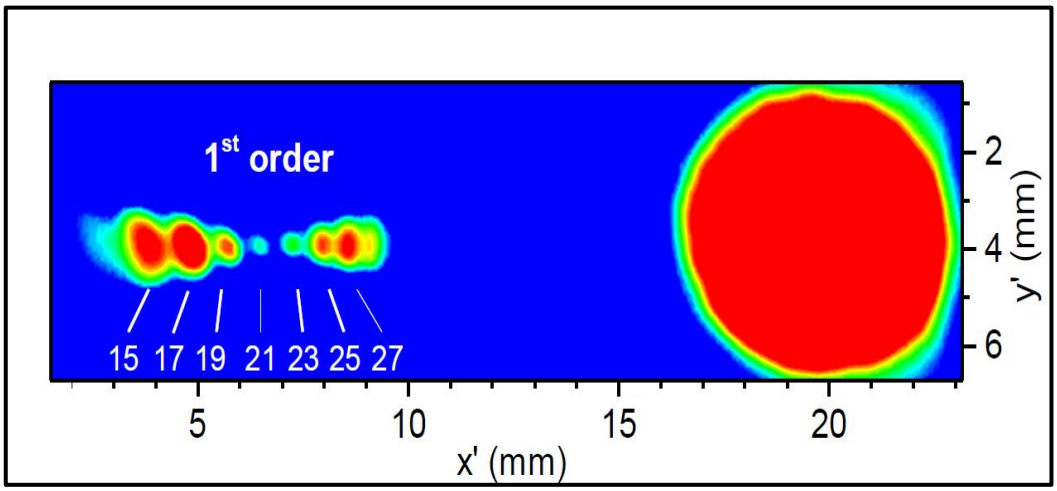

Figure 3.3. The Intensity distribution of XUV light at the slit plane behind the ZP, taken from Ref. [47]. The image is recorded with the use of the ZP designed to select the 21^{st} harmonic. The large spot on the right-hand side represents the unfocused specular reflex. The spots in the first diffraction order are labeled according to the HHG orders.

Figure 3.3 shows an image of the intensity distribution of XUV radiation when the ZP is installed for the selection of the 21^{st} harmonic. The image was recorded by an XUV detector

placed at the plane of the ZP focal point instead of the slit [47]. The left side of Figure 3.3 shows 15^{th}, 17^{th}, 19^{th}, 21^{st}, 23^{rd}, 25^{th}, and 27^{th} harmonics, respectively. These spots represent the harmonic contributions to the first diffraction order. The signal of the 21^{st} harmonic is shown in the middle of harmonics sequence. The spots have different size because only the 21^{st} harmonic is focused on the plane of the detector, other harmonics are focused in front or behind the detector plane. By adjusting the slit width of a few tenths of a millimeter in the ZP focal point, the 21^{st} harmonic can be selected (see the left side of Figure 3.3). The right side of the image shows the zero-order reflection (specular reflex) of XUV beam. The image clearly demonstrates the high dispersion of the ZP.

A gold-coated toroidal mirror (TM) was used to refocus the divergent XUV beam into the interaction chamber. The mirror was mounted on a stage (which is similar to ZP stage) inside a vacuum chamber (see Figure 3.1). The mirror has a focal length of 1200 mm, and refocuses the beam by a magnification factor of 1 to the focal point of the mirror. In order to monitor the reflected XUV beam from the gold-coated toroidal mirror, for diagnostic purposes, a small plane gold mirror (M) was inserted into the XUV path to reflect the beam to the detector. The detector (D) consists of double stack MCP with a phosphor screen and a CCD camera.

3.1.2 Generation of the Third Harmonic Beam

The rest of the split beam of the femtosecond laser system (800 nm wavelength) was used to generate the third harmonic at 266 nm. In the third harmonic generation (THG) setup, we used two Beta-Barium borate (-BaB2O4 or BBO) crystals (EKSMA, BBO-601H) (see Figure 3.4).

The first BBO crystal was used to generate the Second Harmonic (SHG) at 400 nm wavelength (3.1 eV photon energy). A compensation plate of calcite was used for adjusting

the group velocity delay of the SHG and the fundamental beam. The polarization plane of the fundamental beam was rotated by 90° with the use of zero orders λ/2 plate.

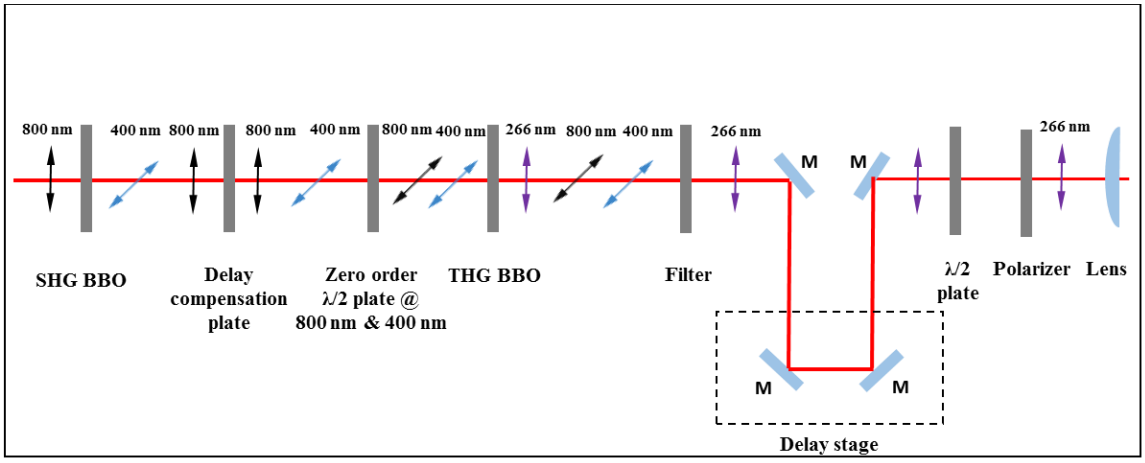

Figure 3.4. Schematic illustration of the THG setup.

The second BBO crystal was used to generate the beam of THG (4.65 eV photon energy). We used a filter to select the third harmonic at 266 nm. The 266 nm beam was reflected by a mirror to the delay stage. In the delay stage, the traveling time of the beam can be adjusted in order to have time overlap between pump and probe pulses. A combination of a λ/2 plate and a polarizer were used to vary the THG intensity. The UV beam enters the vacuum chamber through a UV laser window. In the differential pumping stage, a mirror positioned close to the XUV beam was used to redirect the UV beam toward at the sample. A shutter was positioned in the pump beam way to switch between the pump-probe and probe only measurement.

3.1.3 Beam Diagnostics of the Pump and Probe Pulses

The beam diagnostic in the femtosecond time resolved pump-probe experiments is an important issue which should be considered. Since the femtosecond timescale is beyond the range of the fastest electronics, the pulse diagnostic techniques have to be redesigned in

order to characterize the amplitude and the phase of the electric field. Many techniques, such as auto-correlation and cross-correlation, were used to determine the temporal profile of the laser pulse [174]. The diagnostics of the beam include the temporal profile of pulse, the focus spot size, and the peak intensity, which provide details about the beam quality.

The focus spot size of the XUV and UV beam was measured separately in the experimental chamber, by scanning a knife edge (razor blade) across the beam while monitoring the current of a photodiode positioned behind the razor blade. The measured beam sizes for XUV and UV beam are approximately 60 μm and 100 μm, respectively.

For the XUV beam, for a pure selection of the 21st harmonic, a spectral characteristic of the XUV beam took place. The spectral bandwidth of XUV pulses was measured by recording the kinetic energy of photoelectrons generated during the process of ionization of argon gas.

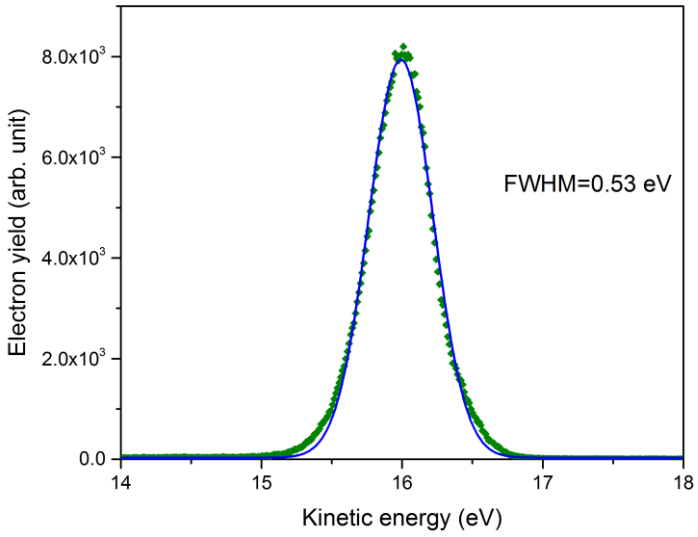

Figure 3.5. The kinetic energy spectrum of photoelectrons generated by ionization of argon with the use of the 21st harmonic (32.55eV photon energy). The solid curves represent the Gaussian fit.

Figure 3.5 shows the kinetic energy distribution of photoelectrons obtained with use of the 21st harmonic (32.55 eV photon energy). The spectrum was recorded by operating the detector in the wide-angle collection mode. The spectral bandwidth of the XUV pulse was determined from the Gaussian fit.

The XUV pulse duration of 50 *fs* was inferred from a cross-correlation measurement in argon with the use of the 800 nm beam [175]. The calibration curve of the photodiode was used to derive the XUV photon flux. The number of photons per pulse was attenuated to 10^6 by decreasing the pump pulse energy of the HHG to 1 mJ.

A simple cross-correlation measurement was carried out to determine the temporal profile of the UV beam. The 800 nm pulse with the duration of 25 *fs* as a reference pulse and the UV beam was focused into the nonlinear medium BBO crystal in order to generate a new frequency. A delay stage was mounted in the UV beam path in order to scan the time overlap of the two pulses. A photodiode was mounted after the BBO crystal to record the photocurrent. Assuming that the 800 nm and the UV pulses have Gaussian temporal envelopes, the cross-correlation signal has the Gaussian shape as well. The dependence of the autocorrelation signal on the temporal delay is given by:

$$A_{cc}(\tau) \propto \int_{-\infty}^{\infty} I_s(t)\, I_r(t-\tau) dt \quad . \tag{3.1}$$

Eq. (3.1) represents the intensity cross-correlation function, where I_r and $I_s(t)$ is the intensity temporal profile of the reference pulse of a known shape and of the unknown laser pulse, respectively. The pulse duration of 140 *fs* of UV beam was determined by deconvolution of the width of the reference pulse from the cross-correlation function.

3.2 Interaction Region

The interaction region included two important setups, the liquid microjet and the time of flight spectrometer. In sections 3.2.1 and 3.2.2, we describe the two setups in details.

The vacuum chamber of the interaction region consists of two hollow parts: a cubic and a horizontal cylindrical vacuum chamber (see Figure 3.6). The two chambers are connected to each other. In the cubic-vacuum chamber, the interaction of the pump and probe beam with the liquid beam occurs. The jet's holder was inserted into the chamber from the upper part and connected with it by a flange. The jet position can be adjusted with an XYZ-manipulator. It was designed to have fine micrometer steps, which allow adjusting of the jet position relative to pump and probe beam as well to the analyzer. The chamber was equipped with two nitrogen-cooled traps. The first nitrogen-cooled trap was designed to collect the west of the sample, and to keep a low pressure around the interaction region. It is connected to the lower part of the cubic-vacuum chamber, (see Figure 3.6).

The cylindrical vacuum chamber is used to connect a second nitrogen-cooled trap that acts as a strong pump for water vapor. The combination of the cryopumps and a turbo pump with a pumping speed of 1600 l/s kept the background pressure in the cubic chamber below 10^{-4} mbar during the experiment.

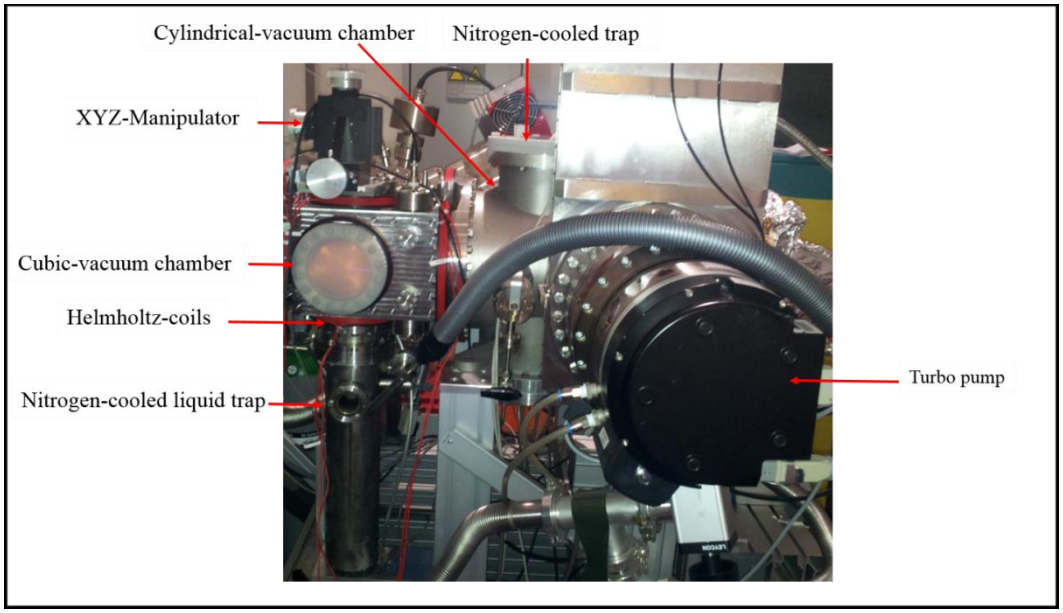

Figure 3.6. The vacuum chamber of the interaction region setup.

The cubic chamber is equipped with Helmholtz coils to compensate for the earth magnetic field and other disturbing magnetic fields. Therefore, the emitted electrons have an undisturbed path to travel to the detector.

3.2.1 Liquid Microjet Technique

The technique of liquid microjets has been widely used to study various processes in the gas and liquid phase [44, 152, 176-178]. It has been developed in 1980 by Faubel and Kisters [28, 29]. The technique provides high-vacuum conditions, even for highly volatile solutions, required for electron detection [147, 179, 180]. The liquid jet is formed by pushing the aqueous solution through a 24 μm, diameter glass capillary into the vacuum chamber.

Figure 3.7. A quartz capillary nozzle with filament of water

A syringe pump was employed to transport the sample solution. As measurements of undisturbed photoelectron spectra require a smooth laminar surface, an extremely stable

flow, was created via accurate flow control. For this purpose, the syringe pump is convenient. To reduce the electronic charging of the sample, a flow rate of 0.5 ml/min was applied to the nozzle [181]. The inner diameter of the glass capillary was 24 µm, giving rise liquid filament of approximately the same diameter, (see Figure 3.7). The jet temperature is typically about 4^{o} C in the vacuum chamber. At a jet velocity of approximately 19 m/s, the sample filament remains laminar over a length of a few millimeters. After this region, it breaks up into a stream of droplets, which is collected at the wall of trap filled with liquid nitrogen, at approximately 20 cm travel distance (see Figure 3.6).

3.2.2 Time-of-Flight Electron Spectrometer

In the present experiment, we used the time-of-flight electron spectrometer (TOF) designed for time-resolved photoelectron spectroscopy of gas, liquid, and solid samples. It is delivered by SPEC [182]. It consists of vacuum housing and four major internal components: Magnetic shielding, input lens system for receiving charged particles, 3D-delay line detector and iris aperture with an external rotary feedthrough, (see Figure 3.8).

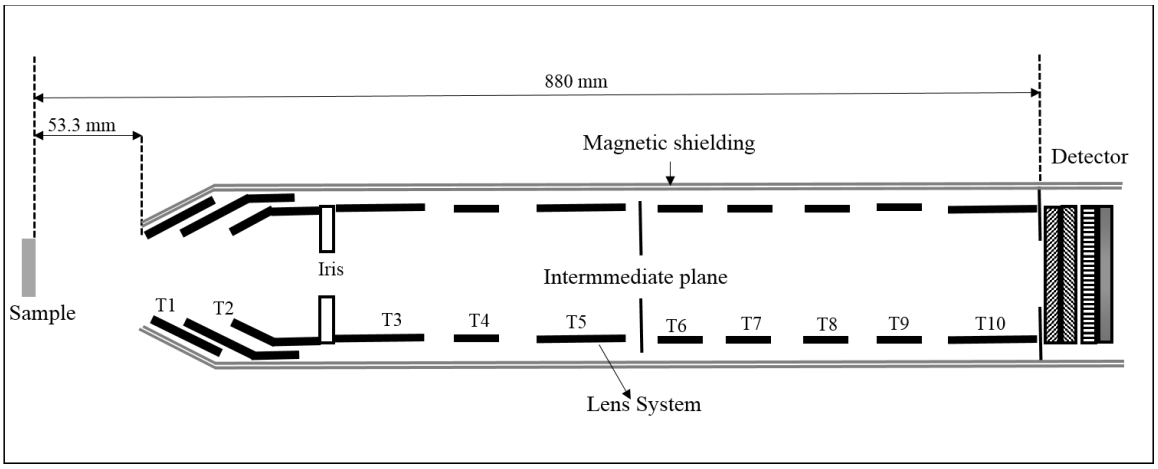

Figure 3.8. The time-of-flight (TOF) electron spectrometer design.

The entrance of the TOF spectrometer was equipped with a skimmer of 200 µm entrance diameter to ensure that the gas pressure inside the spectrometer is below 10^{-6} mbar.

Before reaching the detector, the particles first enter the TOF skimmer and pass through the lens system (see Figure 3.8). In the lens stage, electrons emitted from the sample are imaged onto the detector. The lens system can easily magnify or converge the electron trajectories. The lens system and the detector are surrounded by a magnetic shielding. It has two layers of 2 mm thickness made of the high permeability of µ-metal to provide a low magnetic resistance path for the magnetic flux inside the TOF.

In the TOF, an iris aperture with a variable opening was designed to pass the emitted electrons from the sample to the detector. The distance from the sample to the detector is about 880 mm. The 3D-delay line detector can detect the position in (x, y) axis and the arrival time (t) for each arrived particle. It consists of a dual (Chevron) multichannel plate for pulse amplification and an in-vacuum readout unit. The incident electrons are amplified by a factor of 10^6.

The in-vacuum readout unit, consist of crossed coils. Each position of the particle that hit the crossed coils is encoded by fast data-acquisition unit. The hit time of the particles is also detected by referencing the hit time to an external clock [182].

The TOF spectrometer can be operated in different modes. In the drift mode, corresponding to a classical field-free design, the acceptance angle of electrons emitted from the interaction region is 1^o and the kinetic energy scale is not limited. In this experiment, this mode was used to acquire photoelectron spectra in a wide kinetic energy range, where ionization contributions of both $[Fe(CN)_6]^{4-}$ and water are present.

In the wide-angle collection mode, a predefined non-uniform electrostatic field is imposed in the drift region of the spectrometer, allowing to increase the acceptance angle to $\pm 15^o$. The kinetic energy scale, however, is limited to a certain range around chosen pass energy. In our experiment, this mode was used for the acquisition of spectra with a high signal-to-noise

ratio in an energy range sufficient to reveal XUV ionization from the Fe 3d(t_{2g}) orbital of $[Fe(CN)_6]^{4-}$.

3.3 Spatial and Temporal Overlap of Pump and Probe Pulses

This section describes the procedure of overlapping of the pump and probe pulses, which is an essential condition in the time-resolved pump-probe experiment. Figure 3.9 shows a scheme of the interaction region of the UV probe and the XUV pump beam with the liquid microjet. A mirror was positioned inside the vacuum chamber close to the path of the XUV beam to reflect the UV beam toward the interaction region. With such geometry, we could achieve a small angle of 1^{o} between the propagation directions of the pump and probe beams. The polarization of both beams was kept parallel to the spectrometer axis, oriented perpendicular to the propagation direction of the beams and the micro-jet. The liquid microjet was adjusted to a position in front of the center of the skimmer of the time-of-flight spectrometer. The cross-correlation measurement of the XUV and the UV beam was carried out to define the time resolution in the setup. In the experiment, two procedures were carried out to achieve a good cross-correlation measurement:

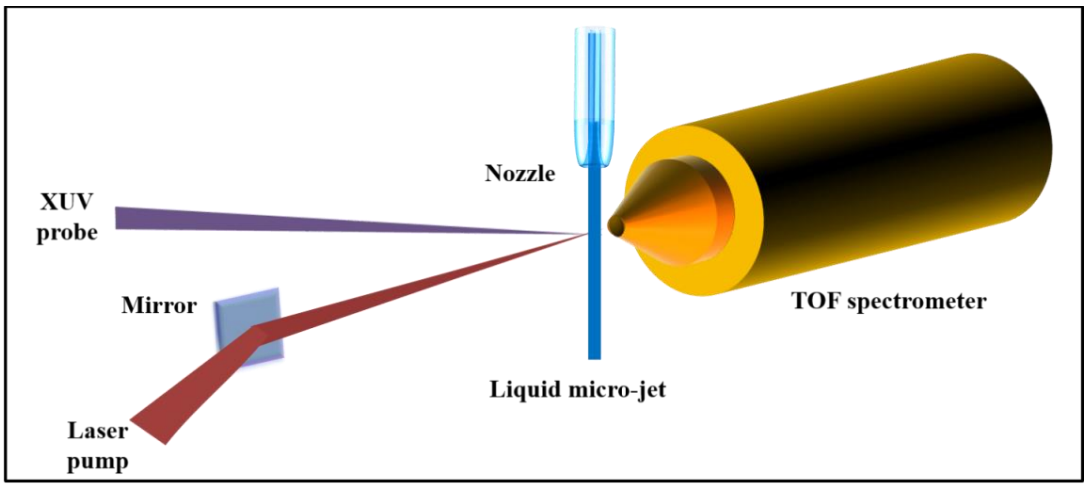

Figure 3.9. Schematic illustration of the interaction region of the UV pump and the XUV probe beam with the liquid microjet.

I) *Spatial overlap*: The spatial overlap has been achieved in the experiment by adjusting first the jet's position with the use of XYZ-manipulator to maximum the emission yield from the probe beam only. Afterward, the pump beam was overlapped with the probe beam. The spatial overlap of pump and probe pulses was controlled by monitoring an increase or decrease in the photoelectron yield integrated over a range of kinetic energies which encompasses the higher-energy part of the water spectrum. At any pump-probe time delay, the sensitivity of photoelectron yield to the pump laser position is caused by the studied SCE, which influences the XUV photoemission spectrum the most when the two pulses overlap on the sample at the same position. Changes in the photoelectron yield are more pronounced when the yield is considered in a spectral range lying in the vicinity of the sharp spectral feature, such as the ''cutoff'' of the water XUV spectrum at the onset position the $1b_1$ energy peak.

II) *Temporal overlap*: The temporal overlap in the pump-probe experiment can be found in two steps. First, a pump-probe delay scan is carried out over a wide range of time delays (full scan). The arrival time of the pump pulse is controlled by moving the optical delay stage positioned in the pump beam path. The delay stage position can be controlled with a precision of 0.1 μm, corresponding to an uncertainty of <1 *fs* in the arrival time of the pump beam. In the full delay scan, a much large time increment in the order of 100 *fs* was used to roughly predefine the zero time delay. A typical delay scan in the full range is shown in Figure 3.10. The zero time overlap can be found from the cross-correlation measurements (see Figure 3.11). The scan exhibits a sharp peak in the XUV ionization yield, which was integrated over a kinetic energy range which includes a sharp spectral feature of the water spectrum (the edge of the $1b_1$ peak). This sharp structure in the delay scan originates due to the studied here SCE and roughly indicates the delay stage position at which the two pulses overlap in time. Though, the width of the sharp peak in Figure 3.10 corresponds to a time interval of a few picoseconds, which is by one order of magnitude larger than the pulse duration of both pump and probe pulses.

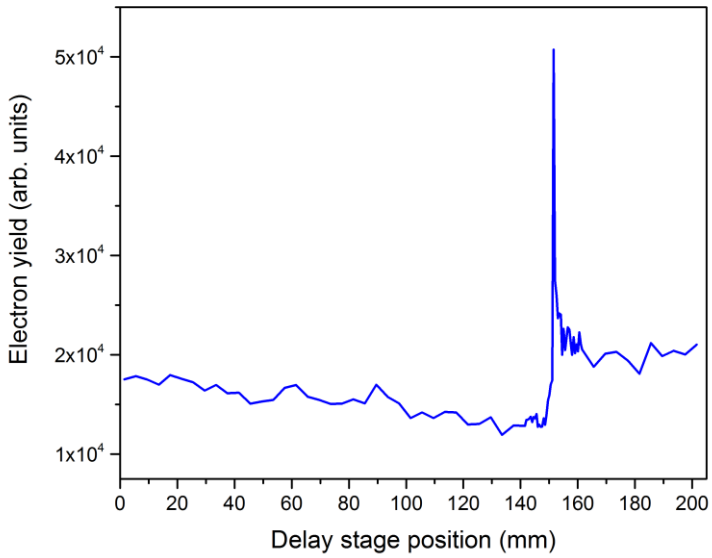

Figure 3.10. Integrated yield photoelectrons ionized by the XUV photons as a function of the position of the optical delay stage placed in the UV pump beam path. The spectra were recorded at the UV pump intensity of 1.25×10^{11} W/cm^2.

In order to define the temporal overlap of the UV and XUV pulses with a high precision, the cross-correlation ionization yield of the two beams was recorded as a function of the time delay. Since the zero time is roughly pre-defined in the first step, the delay stage was moved within a much smaller range in the vicinity of the position of the sharp peak in Figure 3.10, and the stage increment was reduced to 1μm, corresponding to a time delay increment of ~10 *fs*. The cross-section was considered in the first sideband of the laser-assisted XUV ionization process, corresponding to absorption of an XUV and a UV photon. The cross-correlation signal was obtained by integrating of the ionization yield over a kinetic energy range lying within the UV photon energy (4.65 eV) beyond the water spectrum, where the strong XUV emission yield of water is not present. A typical cross-correlation measurement

is presented in Figure 3.11. The experimental data were fitted to a Gaussian profile to characterize the FWHM of the peak.

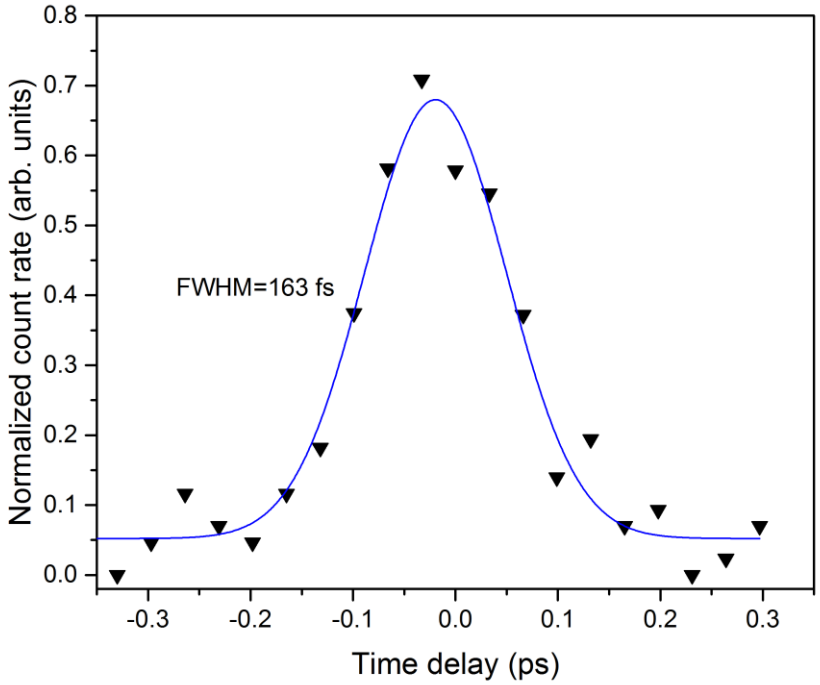

Figure 3.11. Integrated cross-correlation signal in water (triangle). The solid curves represent the Gaussian fit.

In the measurement presented in Figure 3.11, the cross-correlation width is approximately 163 *fs* (FWHM), representing a convolution of the UV pump and XUV probe pulse duration. Since the XUV pulse duration in the used HHG setup is 45 *fs* [47], the UV pulse duration is found to be 156 *fs*. It indicates that the pump pulse duration is broadened due to the group velocity dispersion when the pulse propagates through the optical elements and air to the interaction region.

3.4 Sample Preparation

Aqueous solutions of potassium ferrocyanide $[Fe(CN)_6]^{4-}$ (purity > 99%, purchased from Sigma-Aldrich), with 500 mM concentration were prepared by dissolving the salt high-purity Milli-Q water. NaCl with a concentration of 50 mM was added to the aqueous solution of $[Fe(CN)_6]^{4-}$ to compensate for the streaming potential caused by friction of the liquid flow inside the nozzle capillary [181]. In order to prevent clogging of the capillary, the solution was filtered prior to being pushed through the capillary. This allows the jet run stable for the time of the measurement.

3.5 Experiment with Strong Laser Fields: Laser and Spectrometer Setups.

In the experiment with strong laser fields, the femtosecond optical parametric amplifier was used to generate near-infrared (NIR) radiation. The NIR pulse duration of approximately 40 *fs* was measured by an autocorrelator. The beam size of 22 μm was measured using the same technique as already described in section 3.1.3. The experiments were performed by applying linearly or circularly polarized NIR light.

The TOF spectrometer was used in the experiments with strong laser field has similar operation principles as the one described before (see section 3.2.2), but has also some differences which are outlined below. A detailed description of this spectrometer is given in Ref. [183]. The sample was prepared from high-purity Milli-Q water. A small amount of NaI salt of 50 mM concentration was added to water to reduce the streaming potential [181]. A nozzle of 20 μm was used to deliver the sample into the interaction region.

3.5.1 Laser Setup

3.5.1.1 Optical Parametric Amplifier

A commercially available optical parametric amplifier (OPA) is used to generate ultrashort pulses of radiation in a tunable wavelength range. The principle of OPA is based on the processes of three- waves mixing in a nonlinear medium (BBO crystal). If two waves with frequencies ω_3 and ω_1 propagate through a nonlinear medium, they interact with each other and generate the difference frequency $\omega_2 = \omega_3 - \omega_1$ [84]. The wave vectors of these waves compose the difference $\Delta k = k_1 - k_2 - k_3$. It follows from the principles of non-linear optics that optical parametric amplification is only efficient if the phase matching condition is fulfilled $\Delta k = 0$. The wave with ω_2 is generated and ω_1 is amplified and vice versa. This process is called optical parametric amplification. The amplified wave is called *signal wave* ($\omega_1 = \omega_s$). The second wave, which is generated, is called *idler wave* ($\omega_2 = \omega_i$). The wave with the highest frequency ω_3, which is converted to signal and idler wave, is called *pump wave* ($\omega_3 = \omega_p$) [184].

The femtosecond OPA was used in the present study to generate the NIR beam of 1300 nm wavelength. Figure 3.12 shows the OPA optics setup. Its layout consists of a number of units. These units are the pump beam delivery and splitting optics (PO), white-light continuum generator (WLG), the first amplification stage (PA1), a signal beam expander-collimator (SE) and the second amplification stage (PA2) [21].

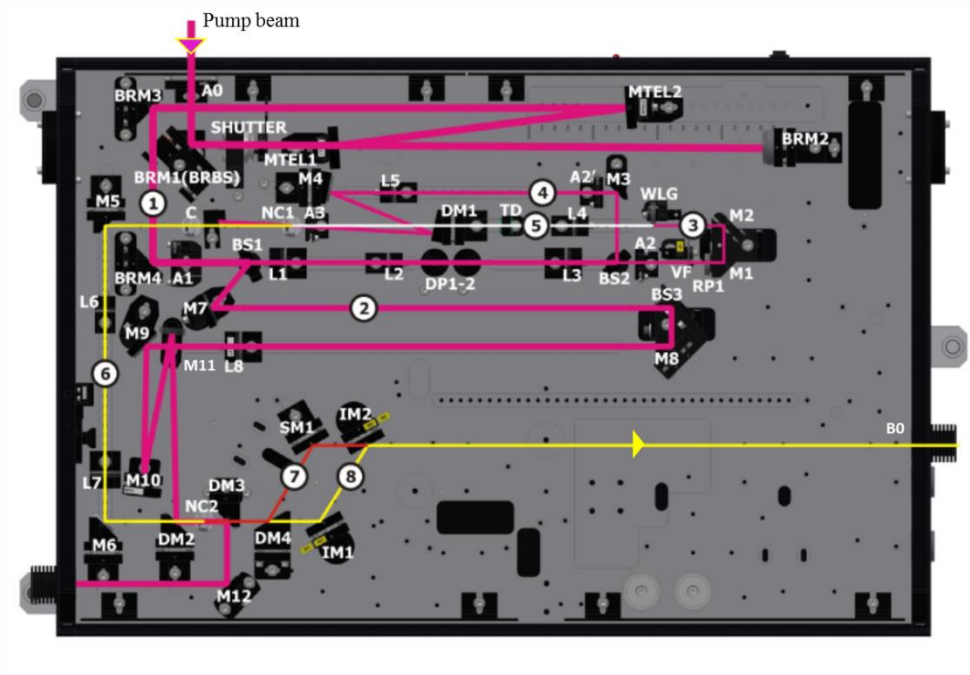

Figure 3.12. Schematic of the femtosecond optical parametric amplifier (OPA): The input pump beam (1) is split to PA2 pump beam (2), WLG pump beam (3) and, PA1 pump beam (4). The generated white light beam (5) is amplified in the nonlinear crystal NC1 and the selected signal beam is used as the seed beam (6), for PA2 in the non-linear crystal NC2. The generated signal (7) and idler (8) beams can be selected by means of the dichroic mirror DM4. Other notions are given in the text [21].

Femtosecond laser pulses of 800 nm wavelength, 5 kHz repetition rate and 1 mJ pulse energy were used to pump the OPA. In the PO unit, the beam passes through a window A0 and is reflected by the first mirror BRM1 to a second mirror BRM2 and then redirected to a mirror telescope MTEL1 and MTEL2 (see Figure 3.12). After the telescope, the beam is reflected by the third mirror BRM3 to the fourth mirror BRM4. The reflected beam from the BRM4 passes through iris aperture A1 and is split first by a beam splitter BS1 and then by a

beam splitter BS2. The transmitted beam after BS2 of 30-70 μJ pulse energy is used to generate a white-light continuum WLC.

In the WLG unit, the beam passes through a variable density filter VF and is reflected from mirrors M1, M2. A λ/2 plate RP1 in WLG is used to adjust the polarization. The WLC pump beam is focused by a lens L3 to a sapphire plate in WLG stage. The VF is used for smooth adjustment of the pump beam intensity. M1 and M2 mirrors are used to control the time delay between the pump and WLC beams in the (PA1) unit. The RP1 changes the pump beam polarization into vertical to generate vertically polarized WLC. The generated WLC beam passes through the lens L4 and a dispersive plate TD. The TD is used to stretch the WLC pulse.

The reflected by BS2 beam is used in the PA1 unit which consists of mirrors M3 and M4, lens L5, dichroic mirror DM1, aperture A3 and a first nonlinear crystal NC1. The DM1 combines the WLC beam with the pump beam by transmitting the WLC beam and reflecting the pump beam. The PA1 pump beam is focused with the lens L5 to the NC1 crystal, whereas, the WLC beam is focused by L4 into the NC1. In the NC1, the two beams (the pump and WLC) are intersected non-collinearly. The NC1 crystal is positioned on a rotational stage in order to adjust the angle of the crystal to reach the phase-matching condition. The amplified WLC beam after the NC1 is considered as the signal beam. The non-collinear geometry provided a good separation of the signal beam from the idler and the residual pump beams. With the use of the compensator C, only the signal beam passes C and reaches the mirror M5. The other beams are blocked by C.

In the SE unit after the NC1, the signal beam is directed into the telescope using the metallic mirror M5. A telescope consisting of two lenses L6 (convex) and L7 (concave) is used to collimate the beams as well as to adjust the beam size. After the telescope, the signal beam is reflected by the mirror M6 and passes through the dichroic mirror DM2, before the second nonlinear crystal NC2. DM2 is used to combine the signal and the pump beams in NC2.

In the PA2 stage, the pump beam has the following path: the first beam splitter BS1, mirror M7, the third beam splitter BS3, mirror M8, lens L8, mirrors M9, M10 and M11, the second dichroic mirror DM2, and the NC2 crystal (see Figure 3.12). This sequence of mirrors is used to delay the pump pulse so that it matches in time with the signal pulse. The BS3 and M8 are positioned on a manual delay stage. This delay line is used for adjustment of the time delay between the pump and the signal in the NC2 crystal. The beam transmitted through BS3 can be used for mixing of the signal and idler frequencies with the pump beam frequency. This mode of OPA operation is not applied in the present work and will not be considered further.

The pump beam is combined with the preamplifier signal beam in the second nonlinear crystal NC2. The NC2 is also positioned on the rotational stage. Both beams propagate collinearly in the NC2, where the signal beam is amplified and the idler beam is generated. After NC2, the beams pass through the third dichroic mirror DM3. The DM3 reflects the residual pump beam to M12 and after M12 it is blocked. After DM3, the beams are separated into signal and idler waves by the fourth dichroic mirror DM4. The signal beam is reflected from DM4 and is redirected by the golden mirror SM1 to the output window B0. The idler beam can be selected by using removable golden mirrors IM1 to the IM2. If IM1 is not inserted, the idler beam is transmitted through the DM4 and is blocked at the mixer stage. If the idler is needed, the IM1 and IM2 are used to direct the idler beam to the output window B0.

3.5.1.2 Control of Linear and Circular Polarization of Light

In the experiment with linearly polarized light, a Glan-type birefringent polarizer and a λ/2 plate were used to control the intensity and the polarization of NIR beam. A telescope consisting of two calcium fluoride (CaF_2) lenses of focal lengths of 150 nm and -75 nm, respectively, was used to expand the beam and an N-BK7 refocusing lens of 200 nm focal

length was used to focus the laser beam into the interaction region (see Figure 3.13). The polarization direction was varied by rotating the λ/2 plate, which was accomplished with the use of a motor. The intensity of the NIR beam was varied by rotating the polarizer since the OPA output is linearly polarized. The expansion of the beam by means of the telescope was made in order to achieve a smaller focus size of the focused beam.

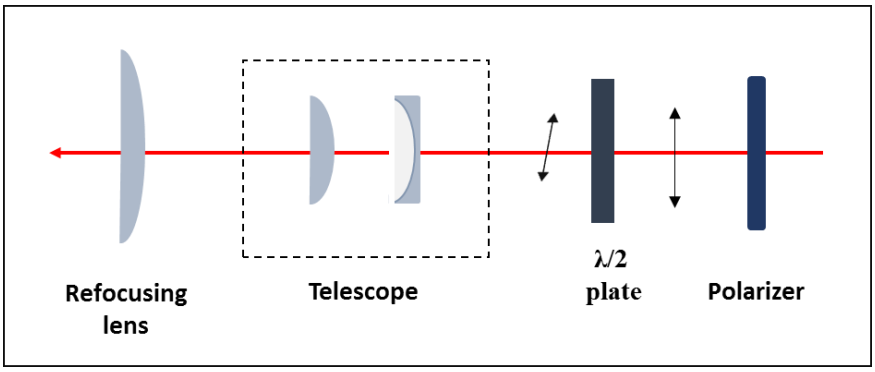

Figure 3.13. Schematic illustration of the linear polarized light control.

To obtain a circularly polarized light, the optical scheme shown in Figure 3.14 was applied. The NIR beam was redirected toward a combination of the λ/2 plate the Glan-type polarizer in order to obtain first a linearly polarized light, with adjustable intensity (by rotating the λ/2 plate) and a fixed polarization direction(defined by the fixed position of the polarizer). A λ/4 (quarter-wave) plate was used to convert the linear polarization to circular.

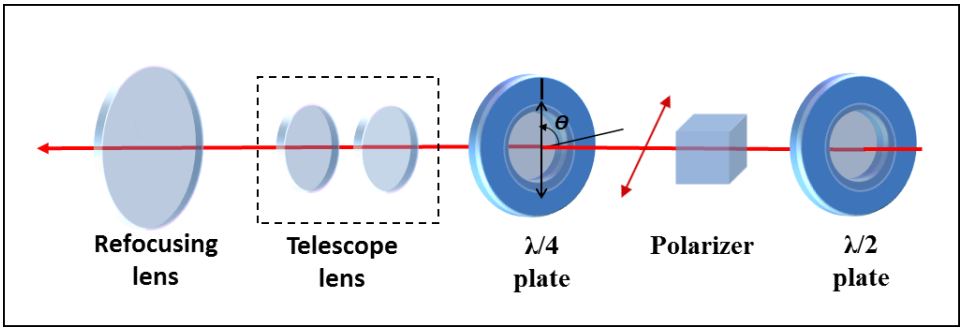

Figure 3.14. Schematic illustration of the circularly polarized light control.

The incident linearly polarized light should have polarization axis oriented at 45° angle relative to the fast and slow axes of the λ/4 plate. To confirm having a pure circularly polarized light in the experiment, a test measurement has been performed. In this measurement, a second polarizer was used of the λ/4 plate, and the intensity of the transmitted light was measured with a power meter while rotating the second polarizer. For circular polarization, the transmitted light intensity does not depend on the orientation angle of the polarizer. As in the experiment with linearly polarized light, the same telescope and the refocusing lens were used to expand and to focus the beam into the interaction region.

3.5.2 Time-of-Flight Electron Spectrometer

The TOF electron spectrometer is designed for experiments on gas and liquid samples. The instrument was used to detect the electrons generated by absorption of XUV and soft x-rays photons [183]. It is also suitable for studying the electron emission in a strong infrared laser field. The spectrometer layout is shown in the Figure 3.15. The entrance of the TOF region is equipped with a skimmer of 500 μm diameter (1). The solenoid coil (2) provides a homogeneous magnetic field inside the drift tube (3). The coil is made of a Kapton-insulated copper wire of 0.8 mm thickness around the drift tube with 500 turns per meter. The drift tube of 97 cm length has been perforated with holes of 2 mm diameter. The μ-metal shielding (4) ensures that the TOF region is free from magnetic fields. A copper mesh (5) of 88% transition is used to accelerate the electrons before reaching the detector. The detector consists of a double-stack of micro-channel plates (6) and a fluorescence screen (7). The conductive layer of the fluorescence screen that collects the electrons function as an anode and generates the electric pulse [183].

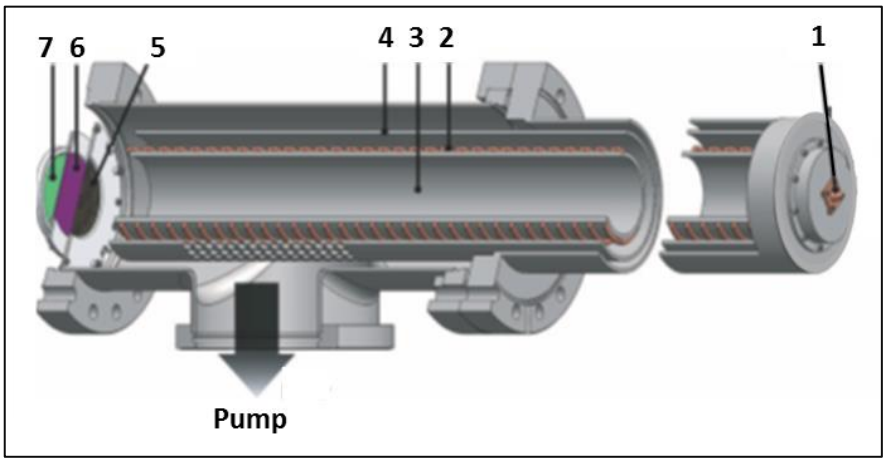

Figure 3.15. The design of the TOF electron spectrometer: skimmer (1), solenoid (2), drift tube (3), μ-metal shield (4), copper mesh (5), double-stack of MCP (6) and fluorescence screen (7) [183].

For the strong laser field experiment, the detection of the slow photoelectrons for linear and the circularly polarized light is carried out. Thus, no low-energy filter of the photoelectrons was used in the measurements. An acceleration voltage of 300 eV was applied to MCP-front. The voltage of 1500 eV was applied to the MCP-back to amplify the electrons signal. A potential of 4.2 kV was applied between the MCP-back and the fluorescence screen, in order to project the amplified electrons onto the fluorescence screen. The signal was recorded by a converter card (RoentDek, fADC4).

Chapter 4

Ultrafast Photoelectron Spectroscopy of Solution: Space-Charge Effect

This chapter presents the results published in:

R Al-Obaidi, *M Wilke, M Borgwardt, J Metje, A Moguilevski, N Engel, D Tolksdorf, A Raheem, T Kampen, S Mähl, I Yu Kiyan and E F Aziz,* ***Ultrafast photoelectron spectroscopy of solutions: Space-charge effect****, New J. Phys. (2015) dx.doi.org/10.1088/1367-2630/17/9/093016.*

The space-charge effect (SCE) observed in the process of electron emission is of fundamental importance in PES studies. It causes spectral shifts and broadenings and often represents a limiting factor in PES experiments. Quantification of this effect is thus very important. In this chapter, the SCE is investigated for $[Fe(CN)_6]^{4-}$ aqueous solution in femtosecond time-resolved pump-probe experiment. Furthermore, we present a simple description of the SCE based on *the mean-field model* and the field *superposition principle*.

4.1 XUV-Photoelectron Spectra of Liquid Water and Iron Hexacyanide

SCE has been studied for an aqueous solution of $[Fe(CN)_6]^{4-}$. The electronic structure of water in the gas and liquid phase as well as of $[Fe(CN)_6]^{4-}$ (aq) was measured using XUV photons (32.55 eV photon energy) for ionization. Figure 4.1 shows the full range of the XUV photoemission spectrum of a 0.5 M $[Fe(CN)_6]^{4-}$ solution recorded without applying the UV pump beam, the total acquisition time was approximately 30 minutes. The spectrometer was operated in the drift mode (compare section 3.2.2), which enables to record spectra in a wide range of kinetic energies. The number of photons per pulse of 10^6 of XUV beam was used to record the spectrum.

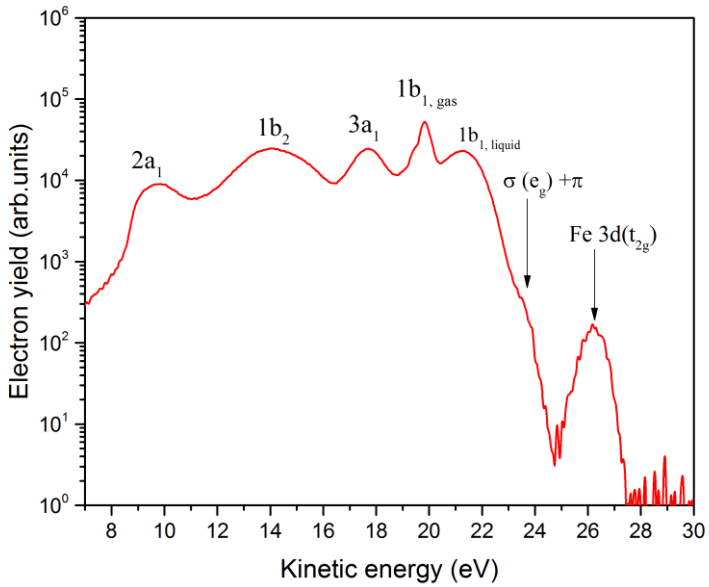

Figure 4.1. Photoelectron spectrum of neat water and of 0.5 M $[Fe(CN)_6]^{4-}$ aqueous solution obtained from ionization by XUV-photons of 32.55 eV energy. Energies are displayed as kinetic energies of the electrons. The spectrum shows $1b_1$, $3a_1$, $1b_2$, $2a_1$, ionization contributions of water in the gas and liquid phase; energy positions agree with previous measurements [45, 146]. The spectral components of $[Fe(CN)_6]^{4-}$, due to emission from the orbitals $\sigma(e_g) + \pi$ (mainly CN-donor contribution) and Fe $3d(t_{2g})$, are labelled.

Ionization contributions from molecular orbital $1b_1$, $3a_1$, $1b_2$, and $2a_1$, of water in the gas and liquid phase are identified according to previous studies [45, 146]. The corresponding peaks are at 23.5 and 26.4 eV, respectively. Peak assignment is according to the literature for the low spin state of $[Fe(CN)_6]^{4-}$ [171, 172]. One should note that the simultaneous detection of photoelectrons from the gas-phase water surrounding the jet is unavoidable since the XUV light focus is much larger than the jet diameter.

4.2 Space-Charge Effect Induced by XUV-Probe Beam

Distortion of the PE spectra due to the SCE appears when many electrons are emitted, and a cloud of high electron density is formed at the sample surface, either through the secondary electron generation by the high energy of XUV photons, or by electrons lifted just above the vacuum level by lower photon energy of the optical pump beam. Let us first consider applying the XUV probe pulse, of varied intensity, without any pump pulse though. The XUV photon flux was varied by changing the intensity of femtosecond laser beam that pumped the HHG process in the argon cell. The number of photons per XUV pulse was varied between 1×10^6 and 2.75×10^6; this was inferred with the help of a movable photodiode to determine the XUV photon flux by measuring the photocurrent. A deceleration voltage was applied to the low-energy filter of the TOF spectrometer to avoid saturation of the electron detector.

Figure 4.2 shows the Fe 3d(t_{2g}) photoelectron peak measured as a function of XUV-pulse intensity. A shift of 500 meV to higher kinetic energies and a peak broadening occur with increasing intensity, which is in qualitative agreement with the spectral changes due to SCE. Gaussian fits were used to determine the center energies of the peaks as well as the peak widths.

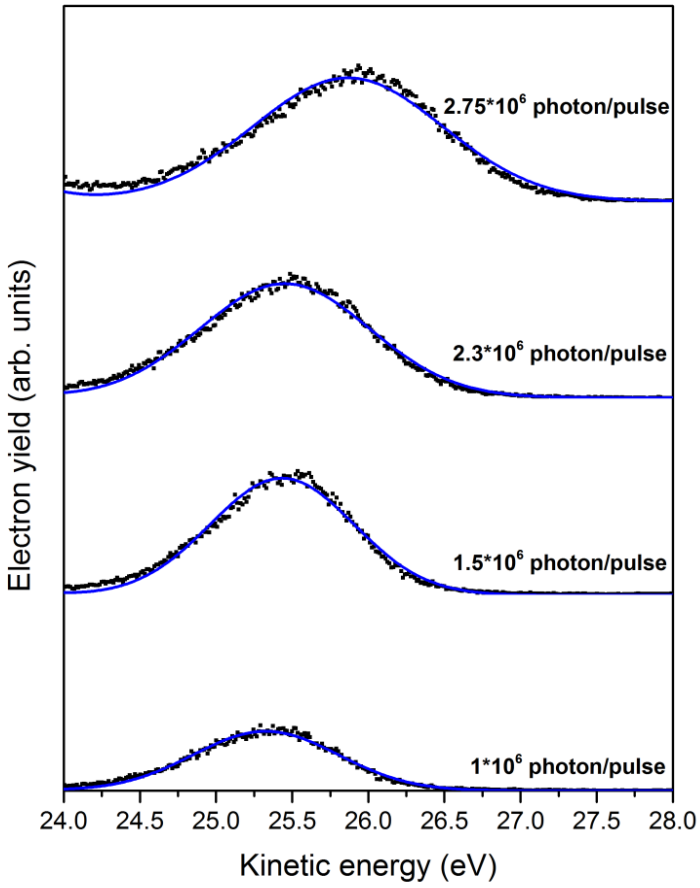

Figure 4.2. The Fe 3d(t_{2g}) photoelectron peak measured as a function of XUV intensity. The number of photons per pulse was varied from 1×10^6 to 2.75×10^6. Gaussian fits are presented by solid lines.

The resulting values are presented in Figure 4.3. Panels (a) and (b) of Figure 4.3 summarize the broadening and the energy shifts. Both observations are consistent with previous simulations and experiments [50, 52, 145, 185-187]. The spectral broadening and the energy shift reach values of approximately 400 and 500 meV, respectively, at the largest number of 2.75×10^6 photons per pulse of XUV beam.

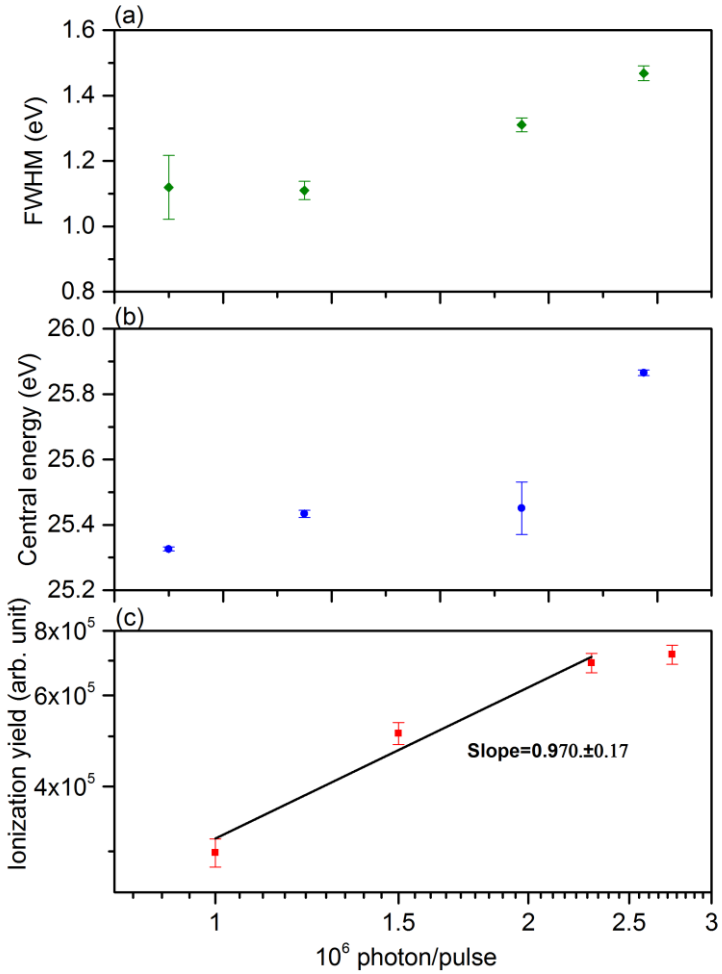

Figure 4.3. Dependency of Gaussian full-width at half- maximum (FWHM) of the Fe 3d(t_{2g}) photoelectron peak (a), the center energy of the peak (b), and ionization yield (c) as a function of a number of photons per XUV pulse.

In references [185, 188], reporting SCE from solid samples for a number of photons per pulse of XUV beam exceeding ~10^4. They observed a peak broadening and energy shift reach to 300 and 200 meV, respectively. The observed SCE-induced increase of the spectral energy shift in the various experiments can be attributed to the high density of electrons

created in the interaction region by the high-intensity of XUV beam. In this case, the electron–electron interaction is stronger than the electron–cation interaction which gives rise to a positive energy shift only. Panel (c) in Figure 4.3 shows the dependence of XUV photoelectrons yields on the number of photons per pulse presented on the double logarithmic scale. In the limit of a low number of photons per pulse (near to 2×10^6 photon per pulse), the non-saturated yield exhibits a linear behavior. The extracted slope is 0.97± 0.17, implying that ionization under the present conditions is a one-photon process. At higher intensities of the XUV beam, the ionization yield is saturated due to the saturation of the electron detector.

4.3 Space-Charge Effect in Pump-Probe Spectra

SCE reflects also in time-resolved photoelectron spectra, causing either an increase or decrease of the kinetic energy (KE) of the photoelectrons. In time-resolved photoelectron spectroscopy from gas and solid samples, positive SCE, i.e. increase of KE, has been observed [52, 71, 140, 143, 186, 187, 189, 190]. Here we investigate how SCE affects the XUV photoelectron spectra. For that, the solution is exposed to a short UV-pump pulse, the third harmonic of the Ti: sapphire laser at 266 nm wavelength (4.65 eV photon energy). The 32.55 eV photon energy of XUV beam is used to probe the transient electron population by recording the full solution valence spectrum. The result for three representative time delays, -12, 0, and 50 ps between the pump and the probe pulses, is shown in Figure 4.4. Spectra are shown on the logarithmic scale. For comparison, the figure also includes the spectrum measured without applying the pump pulse. Negative time delay corresponds to the probe pulse arriving prior to the pump pulse. In these experiments the pump pulse energy was 2 μJ, corresponding to a peak intensity of ~ 1.8×10^{11} W/cm^2 at the beam focus. At such intensity, ionization by the UV pump pulse generates rather slow electrons. This was verified by applying a low voltage of a few volts to the low-energy filter in the spectrometer, which decreased the count rate of electrons produced by the third harmonic beam to zero. Thus, the

spectra presented in Figure 4.4 contain signal exclusively from XUV ionization. The spectral range in Figure 4.4 covers photoelectron signal from both $[Fe(CN)_6]^{4-}$ and water. Contributions from the latter dominate by far, largely because of the small solute concentration. Similar results were obtained for solutions with the use of other solvents, such as ethanol and DMSO. The intensity of the XUV beam was reduced and the SCE generated by the probe beam could be neglected.

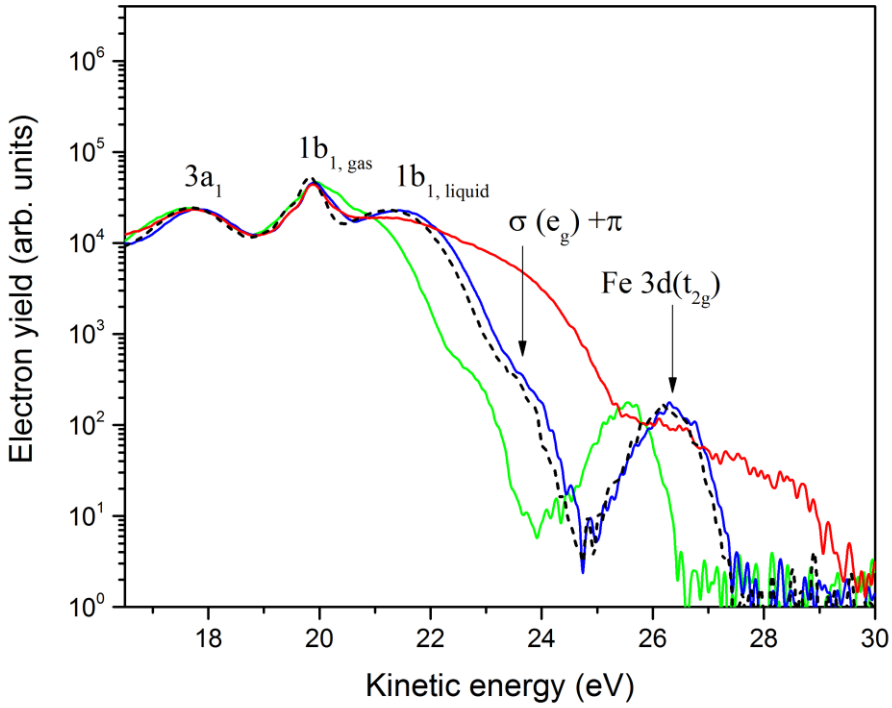

Figure 4.4. Valence photoelectron spectra from 0.5 M $[Fe(CN)_6]^{4-}$ aqueous solution obtained at time delays of 50 ps (green), 0 ps (red), and −12 ps (blue) between the UV pump and the XUV probe pulses. An XUV photoelectron spectrum measured without applying the pump beam is shown by dotted line. Emissions from $1b_1$, and $3a_1$ water orbitals and from Fe 3d(t_{2g}) and σ(e_g) +π orbitals are labeled.

In order to quantify the SCE, we evaluate spectral broadening and energy shifts of several water peaks and of the Fe 3d(t_{2g}) peak.

A remarkable feature apparent in Figure 4.4 is the delay-dependent modification of the spectra which is well pronounced in the range of higher kinetic energies above 21 eV. This is the region of emission from water HOMO and solute HOMO. It is seen that when the pump pulse arrives first the photoelectrons acquire a reduced kinetic energy (negative energy shift; green curve). The situation is reversed when the probe pulse arrives first (positive energy shift; blue curve).

When the pump and probe pulses overlap in time, a nonlinear response of the liquid medium to the superposition of two electromagnetic fields leads to an additional distortion of the XUV spectrum (see the red curve in Figure 4.4). This nonlinear response consists of the simultaneous absorption of one XUV photon and one (or several) UV photons, giving rise to a photoelectron signal which is analogous to the cross-correlation signal recorded when using the copper wire which is part of our pulse-diagnostic routine. The study of laser-assisted XUV ionization of liquids, however, lies beyond the scope of the present project, and we do not consider below short time delays within ±100 *fs* where this effect is significant.

Figure 4.5 shows the Fe 3d(t_{2g}) ionization peak recorded at different UV-pump intensities. The data sets are presented in panels (a) and (b) for two fixed time delays, +198 ps (pump pulse arrived first), and -92 ps (probe pulse arrives first), respectively.

In the former case, the spectral shift at 1.8×10^{11} W/cm^2 peak intensity is negative approximately 0.6 eV, and the shift is positive for negative delay reaches to 0.3 eV. One can see the Figure 4.5 that the SCE reduces significantly when decreasing the UV-pump laser intensity. The reduction of the SCE is due to the low density of electrons generated by the low intensity of the UV-pump beam. It is noted that the energy shift of the Fe 3d(t_{2g}) peak is not affected by the photooxidation of ferrocyanide, which represents the dominant photoreaction channel of $[Fe(CN)_6]^{4-}$ at the applied photon energy of the pump beam [38].

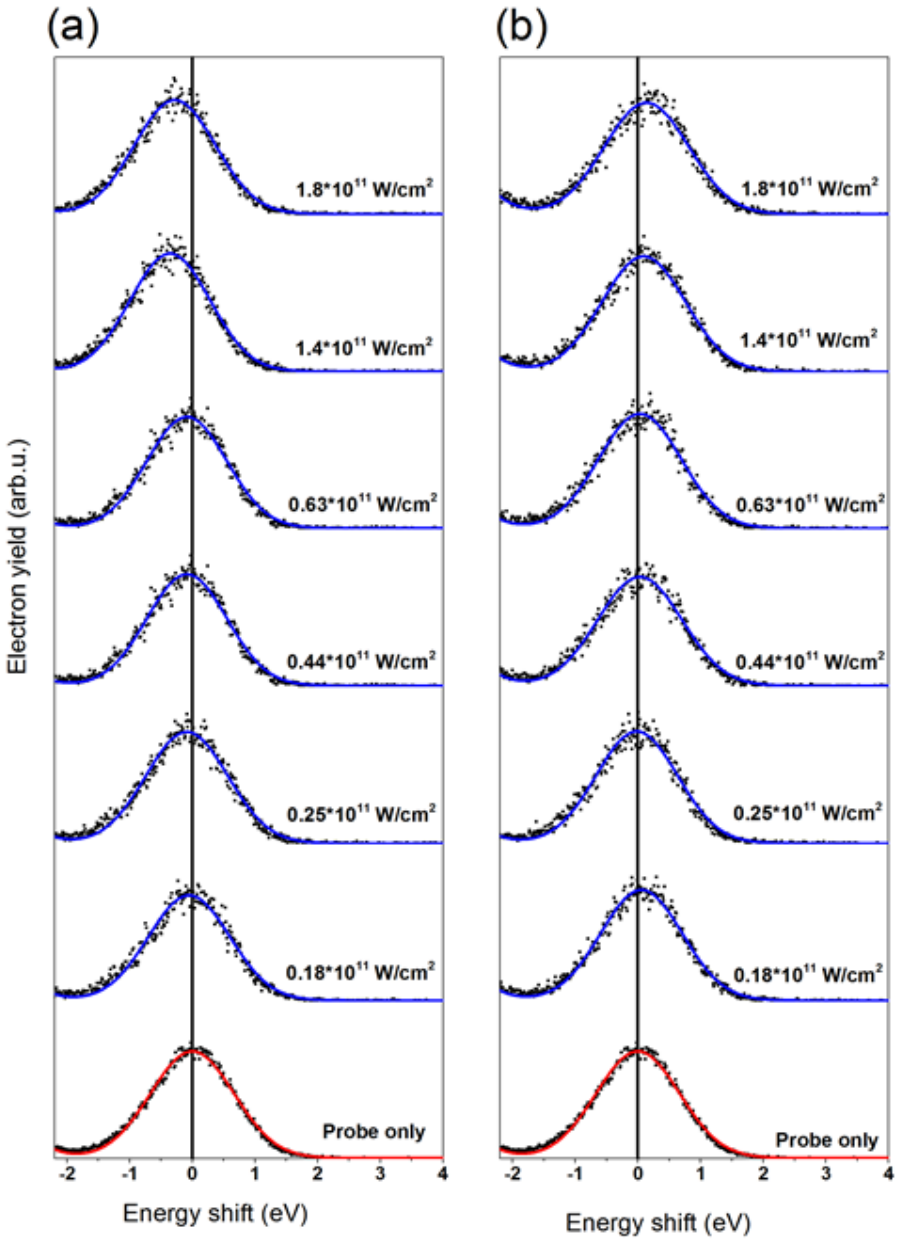

Figure 4.5. XUV photoelectron peak from Fe 3d(t_{2g}) recorded at different UV-pump intensities for two time delays, +198 ps (panel (a)), and -92 ps (panel (b)). The spectra were fitted by Gaussians, shown by solid lines. The vertical lines indicate the peak position in the absence of a UV pulse.

Figure 4.6 shows the dependence of energy position of the Fe 3d(t_{2g}) photoelectron peak as a function of time delay. In the figure, the dashed horizontal line indicates the unperturbed peak position obtained by applying the probe beam only. The spectra were taken by applying different pump intensities in the range between 2.50×10^{10} and 2.54×10^{11} W/cm^2. One can see that the spectral shift exhibits a strong variation, as well as a change of sign, at short time delays. At the laser peak intensity of 2.54×10^{11} W/cm^2, the observed variation amplitude reaches a value of ~1.5 eV. Such a spectral change is dramatic for spectroscopic measurements.

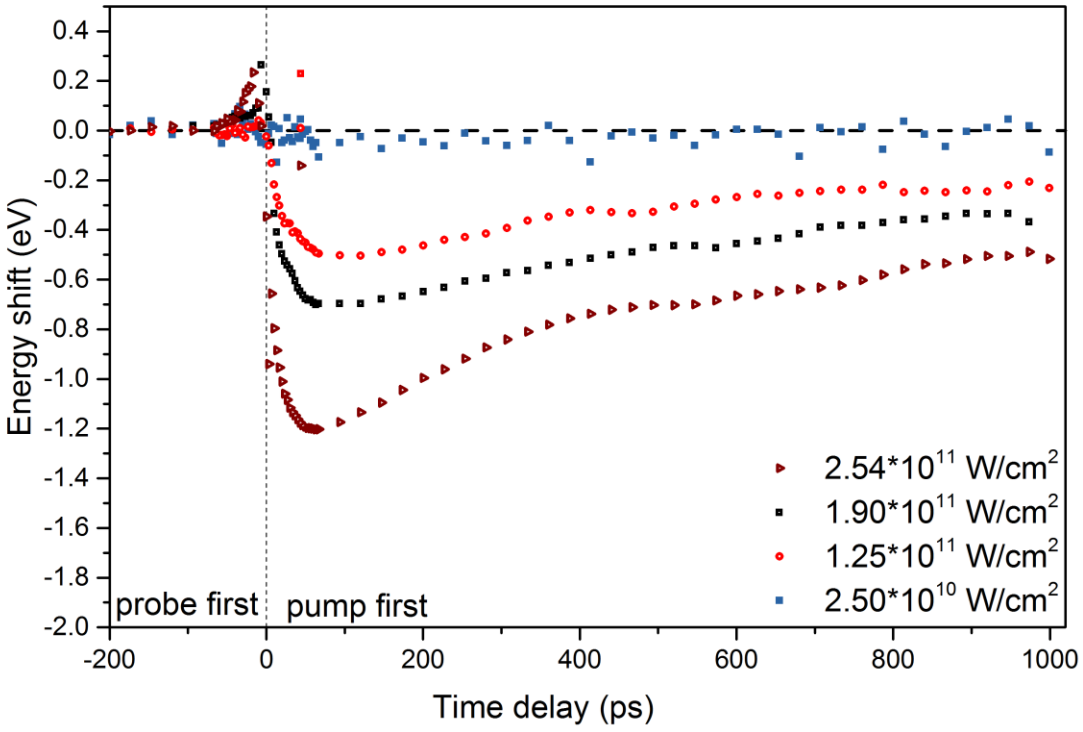

Figure 4.6. Spectral energy shift of the Fe 3d(t_{2g}) ionization peak as a function of time delay between the pump and the probe pulses. Experimental data are measured for different pump intensities in the range of 2.5×10^{10} and 2.54×10^{11} W/cm^2. The dashed horizontal line indicates the peak position obtained by applying the probe beam only.

4.4 The Intensity Dependence Study: Spectral Shift vs Water Ionization Yield

In order to investigate the correlation between the spectral shift and the charge of electrons created by the UV-pump beam the energy shift of the Fe 3d(t_{2g}) photoelectron peak and the respective UV-ionization yields were measured as a function of the UV-pulse intensity, *I*. For the yield measurements the low-energy filter of the spectrometer was disabled. The XUV-probe intensity was kept low so that the photocurrent measured by a photodiode at the interaction region was below 1.3 nA. At these conditions, the SCE generated by the probe beam is very weak. To gain high signal-to-noise ratio, the energy shift was averaged over the range of positive time delays between 3 ps and 1 ns, where SCE yields a large negative value. Both intensity dependencies are presented in Figure 4.7 in double logarithm scale. The absolute values of the averaged shifts will be considered below. It is seen that ionization of water is saturated at laser intensities above 0.6×10^{11} W/cm^2. In the limit of low intensities, the non-saturated yield is proportional to $I^{2.2\pm0.4}$, implying that ionization is rather a two-photon process. This is inferred from a fit of experimental data assuming that the fit function has different polynomial dependencies on *I* below and above the saturation intensity, respectively. The fit results are shown by the black solid line in Figure 4.7.

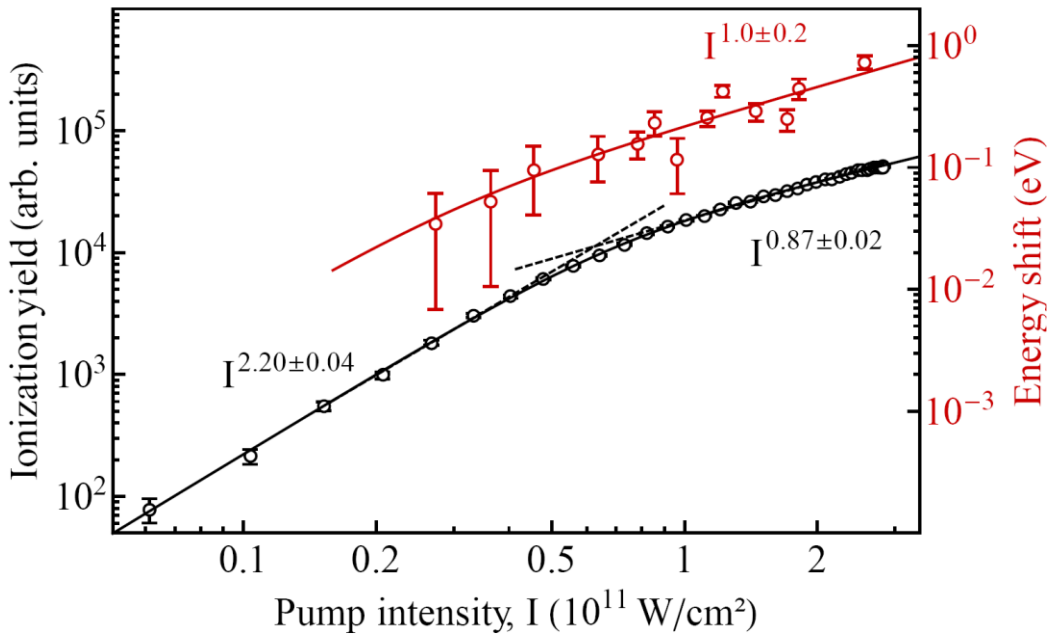

Figure 4.7. Dependency of the energy shift of Fe 3d(t_{2g}) ionization peak (red) and the UV ionization yield (black) on the intensity of the UV pulse. The energy shifts were averaged over time delays between 3 ps and 1 ns. The solid lines and the indicated exponential coefficients represent the resulting fits.

The photoemission threshold of liquid water is at 10.06 eV [191], which requires absorption of three photons of the UV-pump beam for an electron to be vertically excited from the valence band into the continuum. However, due to the possibility of solvent reorientation, the gap between the valence and the conduction bands has a lower value of 6.9 eV [166]. It means that the excitation energy of 9.3 eV (i.e., two UV photons) is sufficient to eject an electron into the conduction band via adiabatic transition. In fact, this two-photon excitation is a route to generate solvated electrons in water [165]. The conduction band of liquid water represents an intermediate state in the three-photon process. Since this state is resonantly

populated in a two-photon transition, the intensity dependence of the non-saturated ionization yield acquires a polynomial coefficient close to 2.

Ionization of gas-phase water, on the other hand, can only occur via non-resonant three-photon absorption and requires a higher intensity to reach saturation. Therefore, the ionization yield of gas-water surrounding the liquid jet is lower. This is confirmed by the fact that a very slight misalignment in the spatial overlap between the pump beam and the jet resulted in the disappearance of the ionization signal. Consequently, the SCE on the gas-phase contribution to the XUV photoelectron spectra is less pronounced, which is consistent with the observations presented in Figure 4.4.

In the saturation regime, the ionization yield is found to be proportional to $I^{0.87\pm0.02}$ (see Figure 4.7). One can see from Figure 4.7 that most of the measurements of the energy shift of the XUV spectra were performed under the saturation regime of water ionization. At intensities below 2.50×10^{10} W/cm^2, the shift was too small and could not be distinguished because of the limited energy resolution. By performing a similar fit (see the red solid line in Figure 4.7) as used in the analysis of the yield curve, we find that at higher intensities the spectral shift is proportional to $I^{1.0\pm0.2}$. Within the error bar of the exponential coefficient, this dependency is the same as for the ionization yield, and we conclude that the spectral shift is directly proportional to the amount of electrons ionized by the pump beam.

The intensity dependency is defined by the geometry of the interaction volume, where the ionization process is saturated. In the case of uniform spatial distribution of the laser intensity in the regime of unsaturated ionization process, the dependence of the ionization yield J on the laser intensity I have the form $J \propto I^n$ where n is the non-linearity order of the ionization process [192]. In the presence of the saturation, and considering the Gaussian distribution of the focused laser beam, the dependence of the ionization yield on I acquires the form $J \propto I^{3/2}$ [193, 194]. The 3/2 power dependencies hold over a broad intensity range, masking the order of the quantum process. The increase of J is due to the increase in the interaction volume where the ionization is saturated. [193, 195]. In the present experiment,

the interaction region is confined by the jet size. Therefore, the polynomial exponent is smaller than 3/2, due to the partial elimination of interaction volume effects [196].

One should note that the saturation intensity is defined by the laser pulse duration and the ionization rate, which is dependent on the order of non-linearity of the ionization process. Application of a laser pulse of longer wavelength would lead to a higher value of saturation intensity due to the increase of the nonlinearity exponent.

For a quantitative characterization of the observed effect, we again consider the Fe 3d(t_{2g}) ionization peak and follow its energy position as a function of time delay between the pump and probe pulses. Figure 4.8 displays a sequence of XUV photoelectron spectra obtained for a number of time delays between pump and probe pulse. The spectra were recorded in two different regimes: at a lower pump intensity of 0.25×10^{11} W/cm^2 when water ionization is not saturated (see Figure 4.8 (a)), and at a higher pump intensity of 1.8×10^{11} W/cm^2, corresponding to the saturation regime of water ionization (see Figure 4.8 (b)).

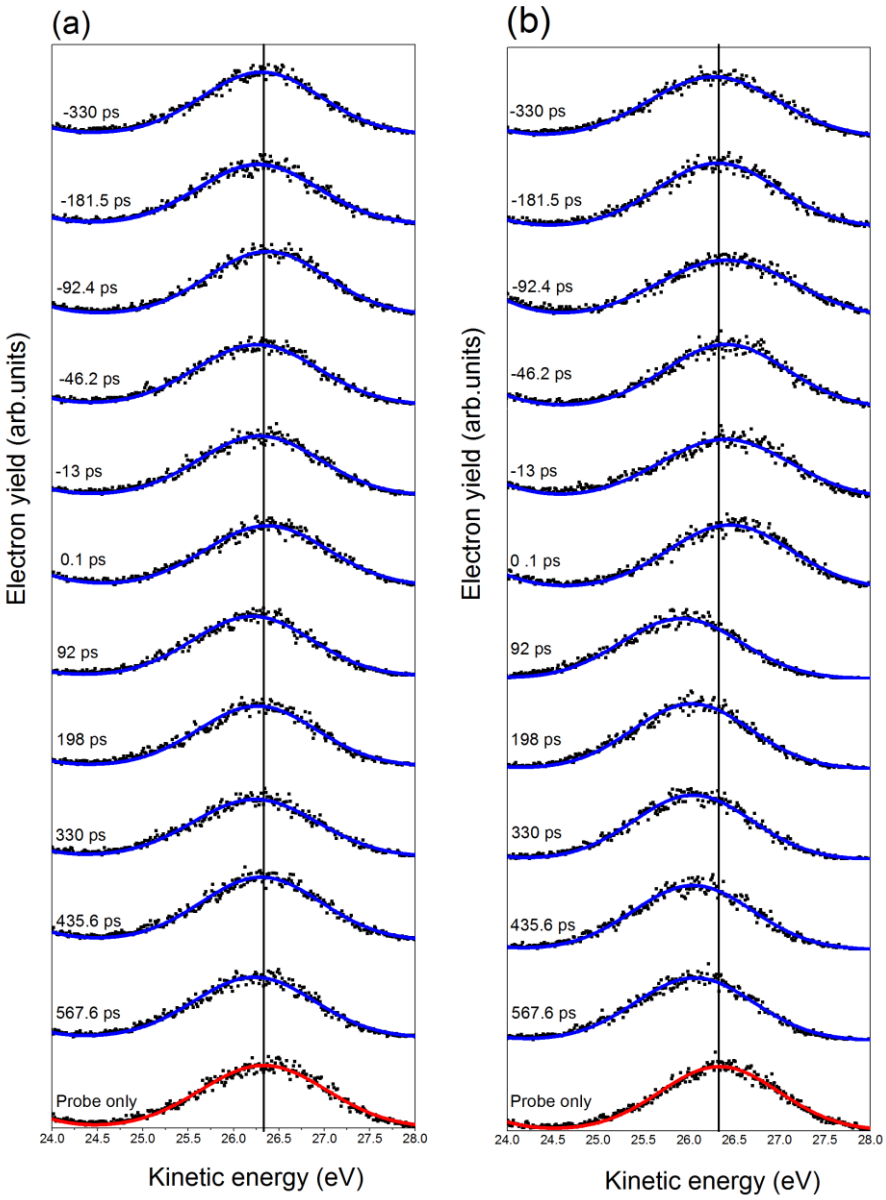

Figure 4.8 The Fe 3d(t_{2g}) ionization peak recorded as a function of time delay between pump and probe pulses. The spectra are obtained at a lower pump intensity of 0.25×10^{11} W/cm^2 (a) and at a higher pump intensity of 1.8×10^{11} W/cm^2 (b). The solid curves represent the Gaussian fits of the Fe 3d(t_{2g}) ionization peak. The vertical solid line indicates the peak position recorded without applying the pump pulse.

The Gaussian fit was used to determine the center energy and the width of the Fe 3d(t_{2g}) peak for each measurement. The fit results show that the height and the area of the peak remain nearly constant over the delay scan. This implies that photooxidation of ferrocyanide, which represents the dominant photoreaction channel of $[Fe(CN)_6]^{4-}$ at the wavelength of 266 nm [38], is negligible at the applied peak intensity and pulse duration of the pump beam. One can see from Figure 4.8 that at the intensity of 1.8×10^{11} W/cm^2 the spectral shift of the Fe 3d(t_{2g}) ionization peak is the dominant effect. The width of the Fe 3d(t_{2g}) photoelectron peak, inferred from Gaussian fitting, is found to be nearly independent of time delay and is the same as the unperturbed width, indicating that the spectral broadening due to the SCE is small. Similar results were obtained for even higher peak intensities of the pump beam in the range up to 2×10^{11} W/cm^2. While the spectral shift is strongly pronounced at the higher pump intensity, one can see from Figure 4.8 that the SCE is rather weak at the lower intensity (under the saturation condition of water ionization). It follows that the negative and positive shift caused by SCE, representing the source of spectral distortion, can be significantly reduced in the time-resolved measurements when the pump laser intensity is reduced below the saturation regime of water ionization.

4.5 Modeling of the Space-Charge Effect

Several theoretical approaches such as *N*-body numerical simulations, mean-field models, and fluid-dynamics simulations were developed to describe the SCE [52, 140, 182, 187, 197]. The *N*-body numerical simulation was applied in the study of the SCE in the regime of few-picosecond laser pulse duration to describe the shift of the gold Fermi edge [140]. In the regime of ultraviolet and extreme ultraviolet light of picosecond and femtosecond pulse duration, the modeling approach was used to study the SCE induced in the solid samples [52, 140].

Simple mean-field models were used to describe the SCE in a number of studies. It was shown that such model can accurately predict the spectral shift of core-level photoemission caused by the SCE in pump-probe experiment [52]. The model could also successfully describe the three-dimensional characters of the SCE in a photoemission experiment performed with electron gun [182]. Other researchers have applied the mean-field model and *N*-body numerical simulations to interpret ultrafast time-resolved electron diffraction experiments [198, 199].

The fluid model was also used to describe the SCE. However, this model was limited to exploring the SCE in the range of picosecond and sub-picosecond pulse duration in experiments on time-resolved electron diffraction in conjunction with photoelectron guns [200].

In this work, the *mean-field model* is adopted to predict the spectral shift arising in the time-resolved photoelectron spectra of the solution. It is complementary to the cited work [52] where the experimental and theoretical study is presented for the time-resolved hard x-ray photoelectron spectroscopy of the solid sample. It was sufficient to consider only the interaction between pump and probe electron clouds, ionized from a solid-state surface, and disregard the possible interaction of electrons with the positive charge created in the solid-state as a result of photoemission. This approximation is valid because of the high carrier mobility in the solid state that leads to ultrafast dissipation of the induced positive charge. In the present case, however, the interaction medium is not a conductor, and the positive space-charge effect needs to be taken into account as well. Below we present a *mean-field model* where this effect is included.

4.5.1 Mean-Field Model and Superposition Principle

The *mean-field model is* also known as *self-consistent field theory*. The idea of the model is to study the behavior of a large number of particles (the so-called many-body system) which

interact with each other. The model treats the interactions between particles not by summing up all mutual two-body interactions, but it describes the interaction of a single particle with the others by an average potential created by the remaining particles [201]. Let us consider a particle q at a spatial position $\overrightarrow{r_q}$, which experiences the potential U created by particles Q. Then the potential of the particle q is defined by the pairwise interaction, and can be expressed as:

$$U(\overrightarrow{r_q}) = \sum_{Q} V(\overrightarrow{r_q}.\overrightarrow{r_Q}) = U[\rho(\overrightarrow{r_q})]\,. \tag{4.1}$$

This expression means that the particle q experiences an average potential which depends on the particle density ρ.

$$\rho(\vec{r}) = \sum_{Q} \psi_Q^*(\vec{r})\,\psi_Q(\vec{r})\,. \tag{4.2}$$

In the present study, the model of one-dimensional character was used to describe the SCE in a non-uniform system containing N charged particles interacting with each other. The basic assumption is to consider the electrons generated by the pump beam as a charged cloud moving at the average velocity in the direction normal to the sample surface (z direction). In this case, the average potential for a system containing N electrons ionized by the pump pulse can be represented as [199]:

$$U(Z) = \frac{Ne}{2\pi\varepsilon_o r^2}\left[\sqrt{Z^2 + r^2} - |Z|\right], \tag{4.3},$$

where e is the electron charge, r is the radius of the pump beam, ε_o is the permittivity of free space, and Z is the axial distance from the center of the cloud. In the next section, the model will be explained in more detail.

The consideration given below is also based on *the field superposition principle*. This principle reads: for all linear systems, the net response at a given place and time caused by two or more stimuli is the sum of the responses which would have been caused by each input

(or stimulus) individually. So that if input X produces a response x, and input Y produces a response y, then input $(X + Y)$ produces a response $(x + y)$ [202].

4.5.2 Positive and Negative Space-Charge Effects

In the present experiment on aqueous solution, we observe positive and negative spectral energy shifts, depending on the sequence of the UV-pump and the XUV-probe pulses. The negative energy shift occurs when the pump pulse arrives before the probe pulse. It is caused by the positive charge accumulated in the liquid medium as a result of the ionization process. The presence of a negative energy shift in the XUV photoelectron spectra is a special feature of time-resolved studies in solutions. The negative energy shift is caused by the carrier mobility in liquids, dissipating on a nanosecond time scale.

To explain the mechanism of shifts induced by SCE, let us consider that XUV photons produce photoelectrons with an initial kinetic energy E_0, escaping from the sample. As mentioned above, the intensity of the XUV beam was attenuated so that charging of the system can be neglected. Our goal is to determine the kinetic energy E_f of the XUV-generated electrons in the far field (at the detector) when a strong laser pulse is applied at a negative or positive time delay t_d. The laser field ionizes the sample, and thus a cloud of electrons with a total negative charge $-Q$ is created. We assume that the cloud formation by the pump pulse is instantaneous, and the laser-generated electrons move toward the detector with a mean kinetic energy E_L which is smaller than E_0, ($E_L << E_0$).

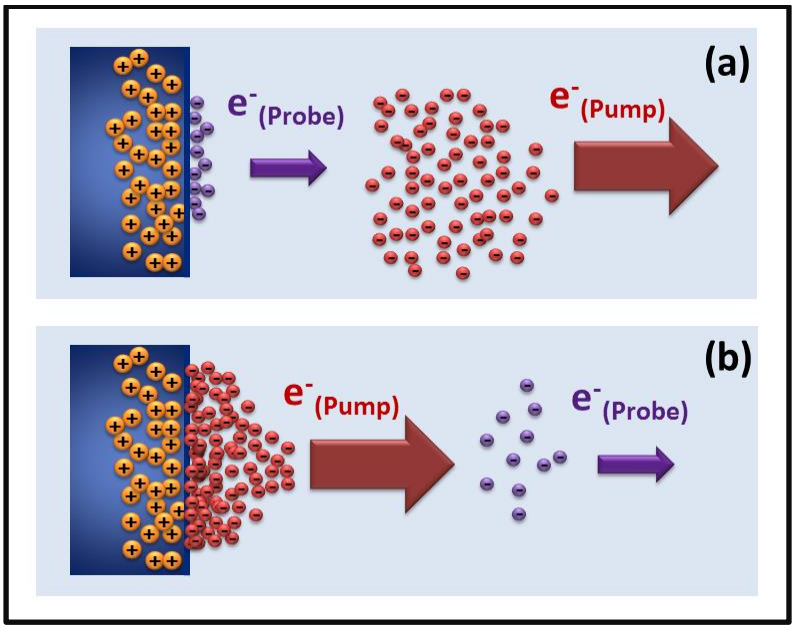

Figure 4.9: Illustration of the charge dynamics in the vicinity of the interaction region for different sequences of the pump and the probe pulses: (a) "pump → probe" sequence, (b) "probe → pump" sequence.

Accordingly, the liquid sample acquires a positive charge $+Q$ localized within the interaction region with the laser beam. We do not specify the size of the interaction region but denote the electric potential of positive charges at the sample surface by U_s. Since the positively charged particles are inertial, we do not consider their motion. However, a slow dissipation of the positive charge near the sample surface is possible due to the presence of carriers, e.g., anions in the solution or electrons generated in the bulk of the sample. Their diffusion into the charged region of the medium leads to regeneration of charge neutrality. Therefore, we consider the positive potential $U_s(t)$ as time-dependent. The characteristic time of this dependency, which is discussed below, is much larger than the time of the electron cloud dynamics.

The potential $U_s(t)$ can be considered as being analogous to the surface photovoltage SPV potential in n-type *Si* (see, e.g., Refs. [203, 204]), where photoexcitation initiates electron motion from the surface into the bulk, and the surface acquiring a positive charge. In the present case, we instead consider photoexcited electrons moving into the outer space from the surface and leave the sample.

The XUV-generated electrons experience the interaction with both the negative and the positive charges created by the laser pulse. By using the field superposition principle, we first consider these interactions separately and then add them up.

Positive-charge effect. If the pump laser pulse interacts with the sample first, the XUV electrons are emerging from the sample in the presence of the potential $U_s(t_d)$ (see Figure 4.9 (a) for illustration). This results in a decrease of their kinetic energy in the far field by $eU_s(t_d)$, where $-e$ is the electron charge. If the probe pulse arrives first (see Figure 4.9 (b)), the XUV electrons move over the distance $\ell_0 = (2E_0/m_e)^{1/2}|t_d|$ from the interaction region before the pump pulse creates the positive charge. Here m_e is the electron mass. In the latter case, the positive charge effect results in a decrease of E_0 by $eQ/(4\pi\varepsilon_0\ell_0)$.

Negative-charge effect. For both pulse sequences, the negative-charge effect leads to acceleration of the XUV-electrons. If these electrons are emitted after the interaction of the pump laser with the sample (see Figure 4.9 (a)), their kinetic energy is sufficiently high to reach the cloud of the laser-generated slow electrons and penetrate through it. Then, the acceleration mechanism can be described in the same manner as in the case illustrated in Figure 4.9 (b). The difference lies solely in the initial potential energy of the Coulomb interaction between the XUV electron and the cloud of the laser-generated electrons, which is equal to $eQ/(4\pi\varepsilon_0\ell_L)$ and $eQ/(4\pi\varepsilon_0\ell_0)$ for the cases (a) and (b), respectively, depicted in Figure 4.9. Here $\ell_L = (2E_L/m_e)^{1/2}|t_d|$ and ℓ_0 is introduced above. To determine the energy gain due to acceleration, we solve the system of two equations representing the energy and the momentum conservation rules:

$$\frac{Q}{e}E_L + E_0 + \frac{eQ}{4\pi\varepsilon_0\ell_{0,L}} = \frac{Q}{e}E_L' + E_f'. \tag{4.4}$$

$$\frac{Q}{e}E_L^{1/2} + E_0^{1/2} = \frac{Q}{e}E_L'^{1/2} + E_f'^{1/2}, \tag{4.5}$$

here the cloud of the laser-generated electrons is considered as a single object of mass $M = m_eQ/e$, and E_f' and E_L' are the kinetic energies of the XUV- and the laser-generated electrons, respectively, in the far field. Eq. (4.4) and (4.5) can be represented in terms of mass and velocity:

$$\frac{MV^2}{2} + \frac{m_e\vartheta^2}{2} + \frac{eQ}{4\pi\varepsilon_0\ell_{0,L}} = \frac{MV_1^2}{2} + \frac{m_e\vartheta_1^2}{2}. \tag{4.6}$$

$$MV + m_e\vartheta = MV_1 + m_e\vartheta_1, \tag{4.7}$$

Were V,ϑ are the initial velocities of the laser-generated and XUV electrons, respectively, and V_1,ϑ_1 are their final velocities in the far field at to the detector.

Eq. (4.7) can be represented as:

$$V_1 = V + \frac{m_e}{M}\vartheta - \frac{m_e}{M}\vartheta_1. \tag{4.8}$$

If $M >> m_e$, then $V1 \approx V$ and equation (4.6) yield:

$$\frac{m_e(\vartheta - V)^2}{2} + \frac{eQ}{4\pi\varepsilon_0\ell_{0,L}} = \frac{m_e(\vartheta_1 - V)^2}{2}. \tag{4.9}$$

From Eq. (4.9) one can derive:

$$E_f = E_0 - m\vartheta V + mV^2 + \frac{eQ}{4\pi\varepsilon_0\ell_{0,L}} + mV\sqrt{(\vartheta - V)^2 + \frac{2}{m}\frac{eQ}{4\pi\varepsilon_0\ell_{0,L}}} \tag{4.10}$$

Below we consider the limits of short ($|t_d|\rightarrow 0$) and long ($|t_d|\rightarrow\infty$) time delays, where the solution acquires a simple form. Adding the negative and positive charge effects together,

the results for the energy change E_f - E_0 of XUV-generated electrons are presented in Table 4.1.

Table 4.1: The time-delay dependency of the energy changes E_f -E_0 of XUV electrons in the far field due to the charge dynamics initiated by the laser pulse. The results are given for different sequences of the pump and the probe pulses in the limit of short and long time-delays. The coefficients are $a = eQ(me/2E_L)^{1/2}/(4\pi\varepsilon_0)$,

$b = (eQE_L/\pi\varepsilon_0)^{1/2}(m_e/2E_0)^{1/4}$, and $c = eQ(m_eE_L/2)^{1/2}/(4\pi\varepsilon_0E_0)$.

Pulse sequence	$\|t_d\| \to 0$	$\|t_d\| \to \infty$
pump → probe	$-eU_s(t_d) + a\|t_d\|^{-1}$	$-eU_s(t_d) + a\|t_d\|^{-1}$
probe → pump	$b\|t_d\|^{-1/2}$	$c\|t_d\|^{-1}$

4.5.3 Comparison of the Model and the Experimental Results

The simple model described above reproduces the experimental results very well as shown in Figure 4.10. The positive-charge dissipation was considered to have an exponential character. We found, however, that a single exponential decay is not sufficient to reproduce the experimental data in the full range of positive time delays. Therefore, the time dependency of $Us(t_d)$ was considered to have two exponential decay constants, which were used as fit parameters.

One should note that for both pulses sequences the predicted energy change as a function of t_d has a singularity at $|t_d| \rightarrow 0$. This singularity is a consequence of the one-dimensional character of the model, where the Coulomb interaction of point charges is used to describe the interaction between the pump and probe electron clouds, and the interaction between the probe electron cloud and the laser-generated positive ions at $t_d < 0$. At short time delays, the initial distance between the point charges is small, giving rise to the high-potential energy of their interaction, which is transformed to the electron kinetic energy in the far field. This description corresponds well to the observed sharp increase in the energy shift at short time delays (see Figure 4.10). The latter provides us with a method to achieve the temporal overlap of XUV and laser pulses with a sub-picosecond precision via optimizing the positive spectral energy shift.

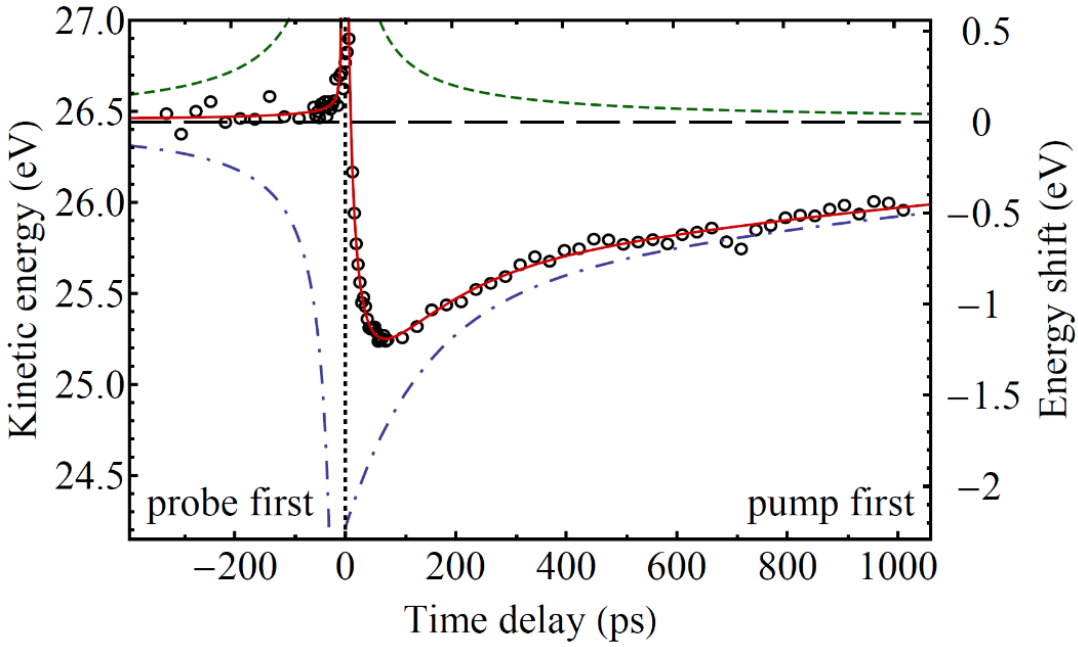

Figure 4.10. Energy of the Fe 3d(t_{2g}) ionization peak as a function of time delay between the pump and the probe pulses, recorded at the laser peak intensity of 2.54×10^{11} W/cm^2. Experimental data are shown by circles. Dashed horizontal line indicates the peak position obtained without applying the pump pulse. The vertical scale on the right-hand side provides a measure of the spectral energy shift due to the space-charge effect. The red solid curve represents results from the analytical model introduced in the present work. The calculated individual contributions from the negative and positive charge effects are represented by green (dashed) and blue (dot-dashed) lines, respectively.

The solid line in Figure 4.10 shows the model curve (Eq. 4.10), and demonstrates that the model describes the measured time dependence of the spectral shift well. The decay constants of 136 ± 15 ps and 1.5 ± 0.3 ns of the positive-charge dissipation were obtained from the fit (see the dot-dashed line in Figure 4.10 for the individual contribution of the

positive-charge effect). The coexistence of two dissipation mechanisms correlated with these values represents an interesting subject for further investigations.

4.6 Conclusion

In this chapter, it is shown that the space-charge effect represents an important problem in the study of electronic and structural dynamics in solutions with the use of femtosecond time-resolved XUV photoelectron spectroscopy. When applying a short laser pulse to excite the solute, the charge dynamics induced due to ionization of the solvent medium leads to a significant distortion of photoelectron energy spectra recorded with the XUV probe pulse. This distortion results in the spectral energy shift, which can exceed 1 eV at moderate peak intensities of the applied laser field.

The intensity studies have demonstrated that the space-charge effect is directly proportional to the yield of ionized electrons. Depending on the sequence of the laser and the XUV pulses, the energy shift acquires a positive or negative value. The negative energy shift arises when the pump pulse arrives first to the interaction region, and it is caused by the positive charge accumulated in the liquid medium as a result of the ionization process. The appearance of a negative shift in XUV photoelectron spectra represents a specific feature of time-resolved studies in solutions. It reflects the low carrier mobility in liquids that leads to the positive-charge dissipation occurring on a nanosecond time scale. At short time delays, the spectral shift exhibits a sharp positive peak. This feature provides an effective means to determine the temporal overlap of pump and probe pulses with a sub-picosecond precision.

Chapter 5

Space-Charge Effect Induced by a Single Laser Pulse of High Intensity

In this chapter, the influence of the SCE on the angle-resolved photoemission spectra generated by a single strong laser pulse is discussed. Near-infrared radiation (NIR) is used to ionize water vapor of variable densities. The density of the medium and the high peak intensity are shown to play significant roles for the SCE. These parameters were studied for linearly and circularly polarized intense laser fields. For both polarizations, the spectra were measured in the tunneling regime where *the Kelydsh parameter* $\gamma < 1$.

5.1 Near-Infrared Photoelectron Spectra of Water Vapor for Linearly Polarized Light

The linearly polarized NIR light at 1300 nm wavelength (0.95 eV) was used to ionize the water vapor. Hence, absorption of 14 photons is required to overcome the ionization threshold of water in the gas phase, 12.6 eV [146]. In order to detect the slow electrons emerging from this process, the low-energy filter of the spectrometer was disabled.

Figure 5.1 shows a photoemission spectrum of water vapor measured at 7×10^{13} W/cm^2 peak intensity in the laser focus. This intensity gives rise to the ponderomotive energy U_p of 11.2 eV which can be calculated according to the Eq. (2.9) in section 2.1. The laser polarization was set parallel to the spectrometer axis so that the shown spectrum was obtained for the emission angle $\theta=0^o$ with respect to the polarization direction. The vapor pressure in the vicinity of the microjet is inversely proportional to the radial distance R from the jet center [28]:

$$P = \frac{R_0}{R} P_0 \ (R > R_o), \tag{5.1}$$

where P_0 is the equilibrium pressure at the jet surface, and R_0 is the jet radius. This equation was used to estimate the vapor pressure for different jet positions with respect to the position of the laser focus. The equilibrium water vapor pressure at 0^o C is 5.9 mbar. A nozzle of 20 µm diameter was used to form the water jet so that R_0 10 µm.

The multiphoton photoelectron spectrum was recorded at 50 µm distance between the jet center and the laser focus. According to Eq. (5.1), the vapor pressure was 1.2 mbar in the interaction volume. However, taking the spatial distribution of the Gaussian laser beam into account, ionization contributions from the liquid cannot be completely excluded.

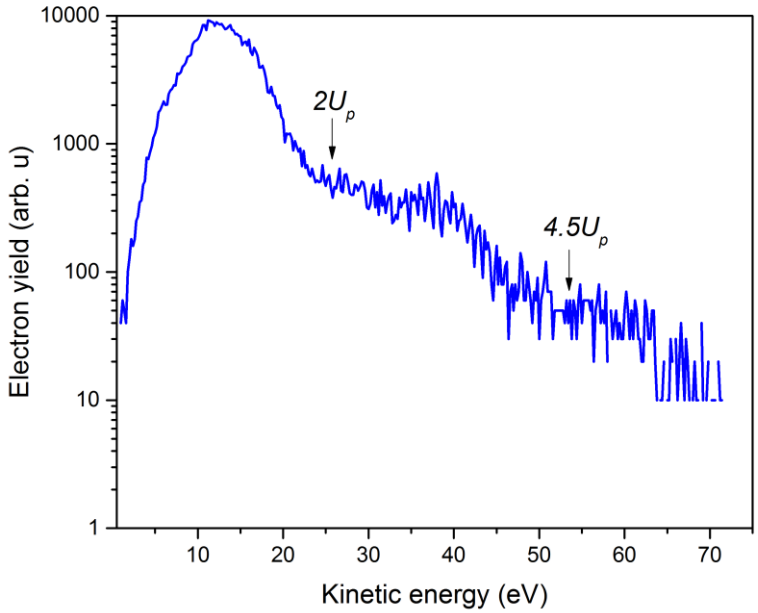

Figure 5.1. The multiphoton photoemission spectrum of water vapor measured at 7×10^{13} W/cm^2 laser peak intensity of the linearly polarized field at the emission angle of $\theta=0^o$. The spectrum was measured at 1.2 mbar vapor pressure.

The kinetic energy cut-off of $2U_P$ of photoelectrons of direct ionization process is indicated in Figure 5.1. The contribution of the HATI process to the ionization yield is also apparent in the spectrum, forming a plateau in the range beyond the $2U_P$. The plateau is followed by a steep roll-of-cut-off, Refs. [65, 67], where this plateau changes the slope and another plateau is formed beyond the 4.5 U_P energy. Such spectral feature has been observed in angle-resolved photoelectron spectra of xenon [205]. According to models used by Lohr *et al* [206], a process of predominantly multiphoton character should create a plateau above 4.5 U_P, and a tunneling process should likewise create a plateau, starting above $2U_P$. This would indicate that the recorded data reveal the transition between MPI and tunneling process. However, the shape of the spectrum in Figure 5.1 in the energy range above $2U_P$ can also be

seen as a peak structure arising at a kinetic energy of ~38 eV on top the declining HATI plateau. The origin of this peak remains a subject for further investigation. For HATI process, a cut-off at 10 U_P should be expected. The observed cut-off lies however at a lower kinetic energy due to the spatiotemporal distribution of laser intensity in the focus, leading to more pronounced ionization contributions at lower intensities. This also leads to the formation of the declined shape of the HATI plateau.

5.1.1 Space-Charge Effect Induced at Different Vapor Pressures in the Vicinity of Microjet

In order to investigate the SCE in the photoemission spectra generated by a single intense laser field, the spectral range at low kinetic energies is of primary interest. This is because the fast electrons are affected by SCE since they leave the interaction region before a significant charge is accumulated. In this study, the spectral range below 20 eV is considered. Spectra of water vapor at different vapor pressures in the vicinity of microjet were measured. By decreasing the distance between the jet and the laser focus from 500 μm to 50 μm, the vapor pressure in the interaction region was varied by approximately one order of magnitude, in the range between 0.12 and 1.2 mbar. Pressures were calculated using Eq. (5.1). The residual vapor pressure in the chamber was approximately 5×10^{-5} mbar, which represents the lowest pressure value studied in the experiment. Figure 5.2 shows three exemplary photoemission spectra measured at the 7×10^{13} W/cm^2 laser peak intensity; the emission angle was $\theta=0^o$. The various vapor pressures are 1.2, 0.3, and 0.12 mbar (see the black, green and blue curve, respectively). One can see from Figure 5.2 that the $2U_P$ energy electrons generated by the HATI process have rather similar kinetic energy distributions at different vapor pressure. However, below $2U_P$ the contributions of direct ionization give rise to different energy distributions. In particular, the maxima of the three distributions lie at different energies. A spline routine was applied to determine the central energies shift of the

direct ionization peaks of the three measurements. The central energy position of the peaks measured at 1.2, 0.3 and 0.12 mbar vapor pressure are found to be at 12.75, 11.42, 9.03 eV, respectively. SCE in the vicinity of the microjet is hence manifested in a spectral energy shift of few eV. This is in contrast to the observation at kinetic energies above $2U_P$, where the fast electrons are not affected by the SCE and the spectral feature at 38 eV remains at the same position for all three measurements. Thus, ionization of the high-density water vapor generates a dense electron cloud, and the Coulomb interaction between electrons leads to the modification of the photoemission spectrum. Figure 5.3 shows the photoemission spectra of direct ionization of water vapor on a linear scale, where the spectral change can be seen in greater details.

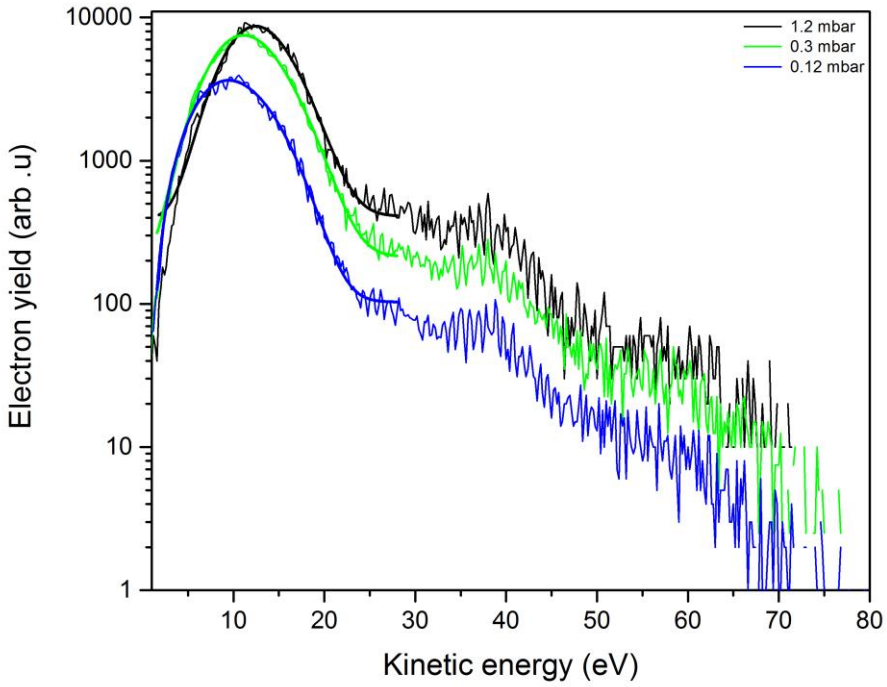

Figure 5.2. Photoemission spectra of water vapor recorded at different vapor pressures and at the emission angle $\theta=0^o$. The spectra were measured at 7×10^{13} W/cm^2 peak intensity.

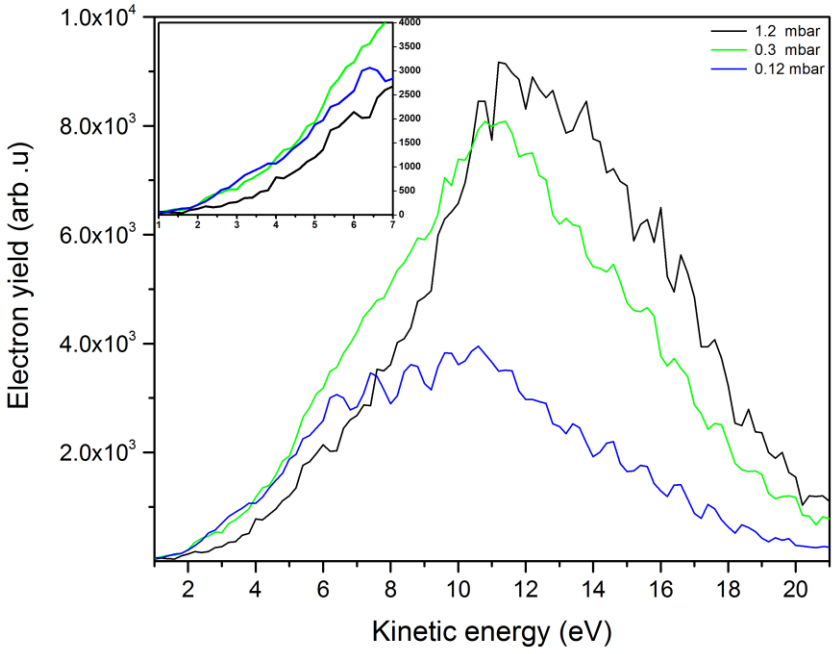

Figure 5.3. Photoemission spectra of direct ionization of water vapor shown on the linear scale. The spectra were recorded at different vapor pressures of 1.2, 0.3, 0.12 mbar. The emission angle is $\theta=0^o$, and the peak intensity is 7×10^{13} W/cm^2.

In the discussion below, the spectral range will be divided into two parts, the higher-energy, and the lower-energy range, above and below the position of direct electrons, respectively. The green and blue curves in Figure 5.3 represent spectra measured at 0.3 and 0.12 mbar vapor pressure. For the latter pressure, the spectral contribution of slow electrons is rather strong (see the blue curve in Figure 5.3). Normally, the signal of slower electrons exceeds the signal of the faster electrons (above the peak energy) and in such a low-density medium the SCE is rather weak.

At 0.3 mbar vapor pressure (see the green curve in Figure 5.3), the yields of the faster and the slower electrons are increased due to the increase of medium density. In this case, however, the manifestation of SCE becomes pronounced. A reduction in the ratio of the slower electron yield to the faster electron yield due to SCE is apparent in the spectrum. This becomes even more pronounced in the spectrum measured at 1.2 mbar vapor pressure (see the black curve in Figure 5.3). The spectrum shows a significant reduction of the signal of slower electrons, while the signal of the faster electrons is dramatically increased in this measurement. The SCE can be interpreted as follows. The decrease of the signal of slower electrons in the vicinity of the microjet arises from the higher vapor pressure. The high density of the generated positive ions creates a strong electric field which is sufficient to trap the slower electrons near the sample surface. As a result, the slower electrons do not reach the detector. In contrast, the faster electrons are accelerated by the slower electrons and, thus, gain an additional kinetic energy due to the SCE.

5.1.2 The Intensity Dependence Study for Linearly Polarized Field

The peak intensity of the laser field represents one of the important parameters that plays a significant role in SCE. Here, the intensity dependence of SCE is considered for the case of linearly polarized field. Figure 5.4 shows photoemission spectra of water vapor measured at different vapor pressures and different laser intensities.

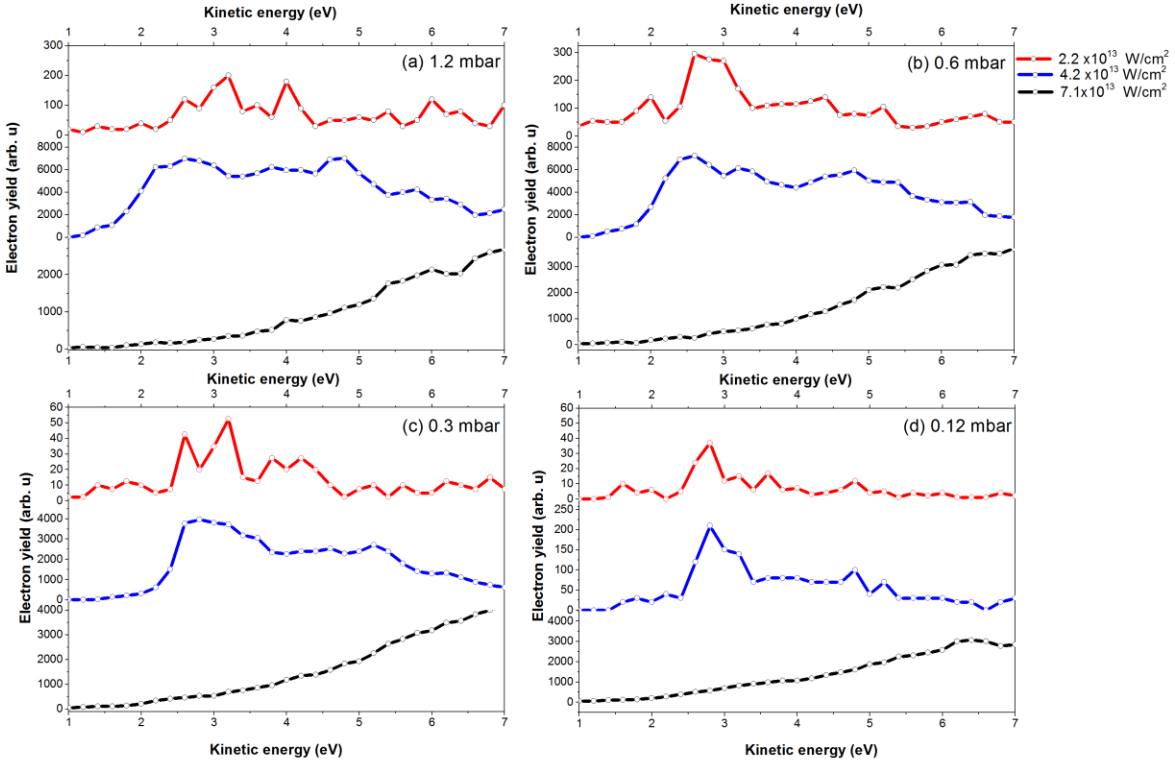

Figure 5.4. Kinetic energy distributions of water vapor recorded at vapor pressure: 1.2 mbar (a), 0.6 mbar (b), 0.3 mbar (c) and 0.12 mbar (d). The photoemission spectra were measured at 7×10^{13}, 4.2×10^{13} and 2.2×10^{13} W/cm^2 peak intensity.

The peak intensity was varied from 2.2×10^{13} to 7×10^{13} W/cm^2 by rotating the λ/2 plate. Photoelectrons were detected along at the direction of the linear polarization $\theta=0^o$. In the Figure, the spectra are shown in the range of kinetic energies below 7 eV. At the low laser intensity of 2.2×10^{13} W/cm^2, the yield of the slower electrons appears as a peak structure in the emission spectra (see red curves in Figure 5.4). When the laser intensity was increased to 4.2×10^{13} W/cm^2 (see blue curves in Figure 5.4), the slower electron peaks became more pronounced. However, the spectra measured at the high intensity of 7×10^{13} W/cm^2 are rather different from the previous (see black curves in Figure 5.4). In this case, a suppression of the

peak signal intensities in the range below 7 eV kinetic energy is observed. The suppression of the peaks cannot be induced by the channel closing effect. This can be confirmed from the dependence of spectra on the vapor pressure.

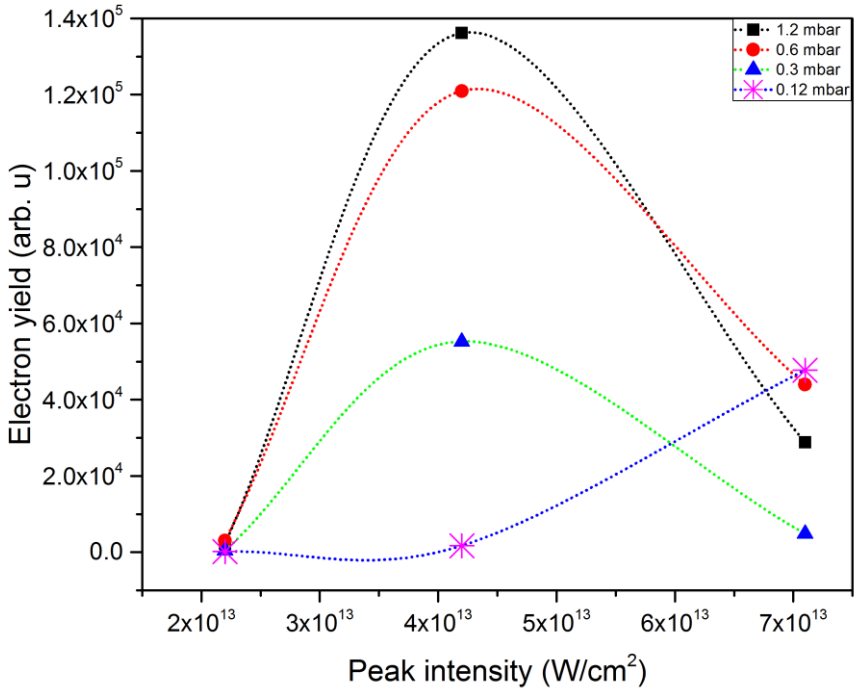

Figure 5.5. Ionization yield from water vapor as a function of the peak laser intensity, for three different water vapor pressures. The signal was integrated over the range of kinetic energies from 1 to 7 eV.

Figure 5.5 shows the electron yield recorded at the vapor pressures 1.2, 0.6, 0.3, and 0.12 mbar, respectively. Signal was integrated over the range of 1 to 7 eV electron kinetic energy range in order to demonstrate the SCE clearly. The black (squares), red (circles), and green (triangles) data points show a reduction of the signal by more than a factor of three when the intensity is increased from 4.2×10^{13} to 7.1×10^{13} W/cm^2. The partial disappearance of the

slower electrons with increasing laser intensity is seen (see red and blue curves in Figure 5.4 (a), (b) and (c)). It is a consequence of strong SCE created by a large amount of positive ions generated at the high laser intensity. In contrast, the spectra recorded at the low vapor pressure of 0.12 mbar exhibit opposite tendency (see the blue curve in Figure 5.5). At this pressure, the integrated signal shows an increase of the electron yield by a factor of two at the high intensity. Thus ionization of water vapor at the low vapor pressure of 0.12 mbar creates a weak SCE, which is not sufficient to affect slower electrons.

5.2 Near-Infrared Photoelectron Spectra of Water Vapor for a Strong Circularly Polarized Light

The process of strong-field ionization by circularly polarized light was studied for the same NIR light wavelength of 1300 nm (0.95 eV) as in the linear-polarization study. Photoelectrons were detected in the plane of the circular polarization. Figure 5.6 shows the photoemission spectrum of water vapor measured in the vicinity of microjet at the vapor pressure of 0.6 mbar. The distance between the jet and the laser focus was 100 μm. The spectrum was recorded at 6.64×10^{14} W/cm^2 peak intensity. The kinetic-energy distribution of photoelectrons in the circularly polarized field is different than in linearly polarized field ionization (see section 5.1). According to Refs. [207, 208] the maximum in the energy spectrum for the circularly polarized field corresponds to the ponderomotive energy $F^2/\ 2\omega^2$. The ponderomotive energy of ~ 102 eV has been calculated from the peak intensity and the wavelength applied in the experiment. It should be noted that in the tunneling regime the ionization rate in the circularly polarized field is lower than in the field of linear polarization of the same intensity value [209]. It requires an order of magnitude higher intensity for the circularly polarized field to achieve a comparable ionization rate as for the linearly polarized field.

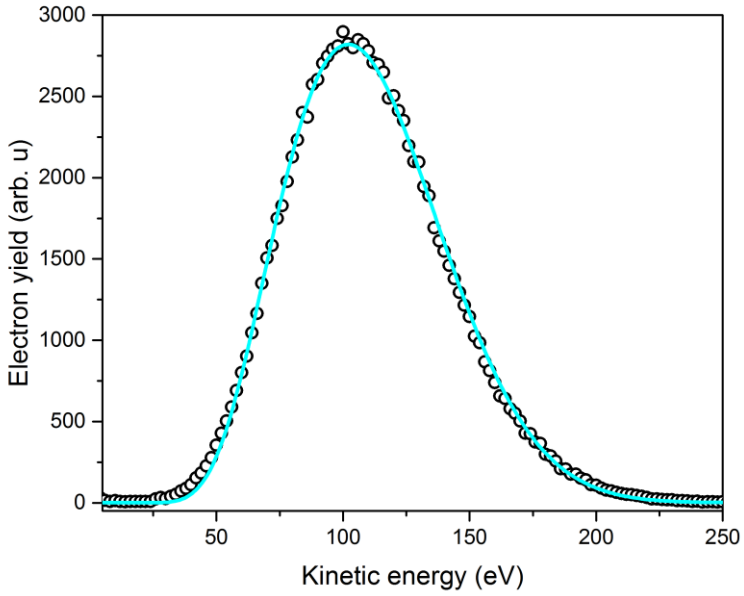

Figure 5.6. Distribution of electron kinetic energies in the plane of circular polarization (black open circles). The photoemission spectrum was recorded at 0.6 mbar vapor pressure and 6.64×10^{14} W/cm^2 peak laser intensity. The solid line represents results of the simulation based on SFA theory.

5.2.1 Simulated Spectrum and its Comparison to the Experimental Results

The photoemission spectra generated in a strong circularly polarized laser field were simulated using the approach developed in Ref. [80]. The method is based on the strong field approximation (SFA) to describe the ionization transition in the length gauge. In this approximation, the core potential is neglected in the description of the final electron state. While the approach is suited for the description of the process of photodetachment of negative ions, where the asymptotic Coulomb potential of the core is absent, in this work the

SFA method is applied to describe the ionization process of neutral molecules in a strong laser field.

The simulation is carried out by applying Eq. (2.38), and taking into account the experimental conditions. The $1b_1$ HOMO orbital of the water molecule in the gas phase has the binding energy E_0=12.60 eV [146] and is described by the angular momentum quantum number $l=1$. Therefore, the simulation involves summation over photodetachment rates for different values $m_l=0, \pm 1$ of the projection of the initial angular momentum. The electron yield was integrated over the spatiotemporal intensity distribution in the laser focus [210] with peak intensity value of 6.64×10^{14} W/cm^2. The result of the simulation is presented in Figure 5.6 by the solid blue line. It shows the distribution of electron kinetic energies in the plane of the circular polarization while is normalized to the experimental curve. The simulated spectrum consists of contributions from a series of above-threshold ionization peaks with a number of absorbed photons $n\geq14$. The ATI peaks are not resolved in the spectrum because they are broadened due to the spatiotemporal variation in the ponderomotive energy shift. Figure 5.6 shows a very good agreement between the experimental data and the predictions in the length gauge.

5.2.2 The Vapor Pressure Study in the Vicinity of the Microjet for Circularly Polarized Field

In order to investigate the SCE for the circularly polarized field, photoemission spectra of water vapor were measured at different vapor pressure, i.e., for different distances of the liquid jet from the laser focal spot. Figure 5.7 shows the obtained photoelectron distributions measured at a peak intensity of 6.1×10^{14} W/cm^2.

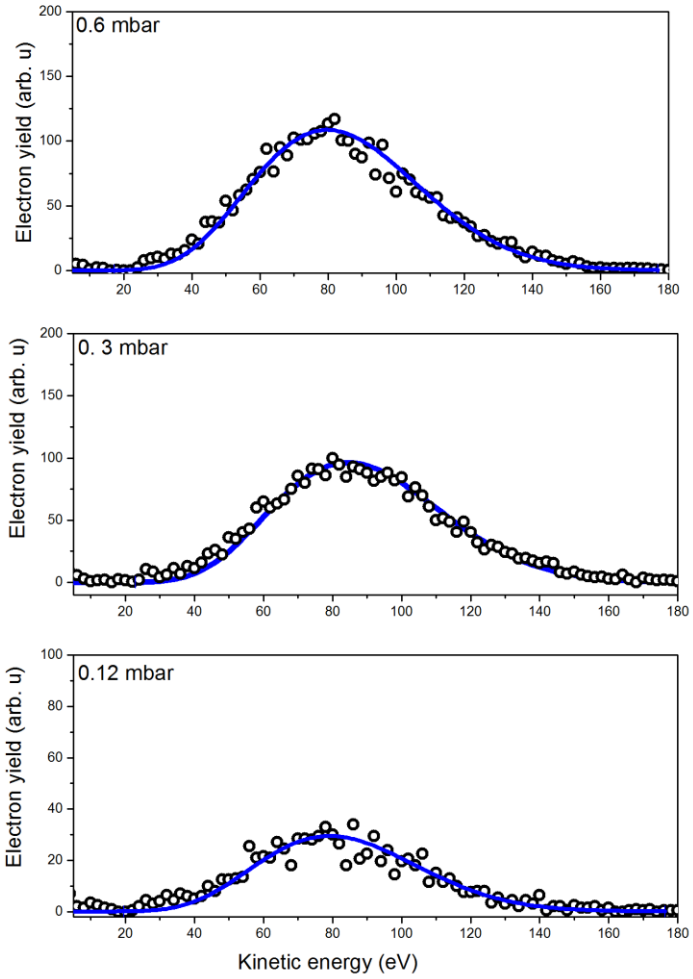

Figure 5.7. Distribution of electron kinetic energies in the plane of circular polarization measured at 6.1 $\times 10^{14}$ W/cm^2 peak intensity (open circles). The photoemission spectra were measured at the vapor pressures 0.6, 0.3, and 0.12 mbar. Solid curves show predictions by the SFA theory in the length gauge.

The presented spectra are of the vapor pressure of 0.6, 0.3, and 0.12 mbar. The simulations with the use of SFA approach in the length gauge were performed to describe the experimental spectra (see Figure 5.7). Analysis of the experimental spectra, i.e., the determination of widths and central energies of the peaks was done using the Origin software. No significant change in peak width is observed, and also no energy shift is found, showing that the SCE on the photoemission spectra is negligibly small in the case of circularly polarized field. This is because for the applied experimental parameters the ionization yield is not high enough to cause the SCE.

5.2.3 The Intensity Dependence Study for Circularly Polarized Field

As for the linear-polarization study, the intensity-dependence was explored in the investigation of SCE in the case of strong-field ionization by circularly polarized light. The laser intensity was varied from 6.13×10^{14} to 6.64×10^{14} W/cm^2. Obtained electron emission spectra from water vapor, recorded with circularly polarized NIR pulses, are shown in Figure 5.8. The spectra were measured at 0.6 mbar vapor pressure in the vicinity of the microjet. Open circles represent the experimental data, and the red solid lines show the predictions based on SFA theory in the length gauge. The spectral peaks are ponderomotively shifted and broadened due to the increase of the laser intensity, but not because of the SCE. This is inferred from the analysis of the peaks using the Origin software. The vertical line in Figure 5.8 shows the center energy of the ionization peak measured at the laser intensity 6.13×10^{14} W/cm^2. For the higher laser intensities than 6.13×10^{14} W/cm^2, the peak position is shifted to higher energy for increasing laser intensity. Energy shift is up to ~10 eV at the highest peak intensity of 6.64×10^{14} W/cm^2. The width of the peak increases by approximately 3 eV. Observed spectral changes are in good agreement with the predictions of the SFA theory, and the SCE does not need to be invoked in the interpretation of the experimental data.

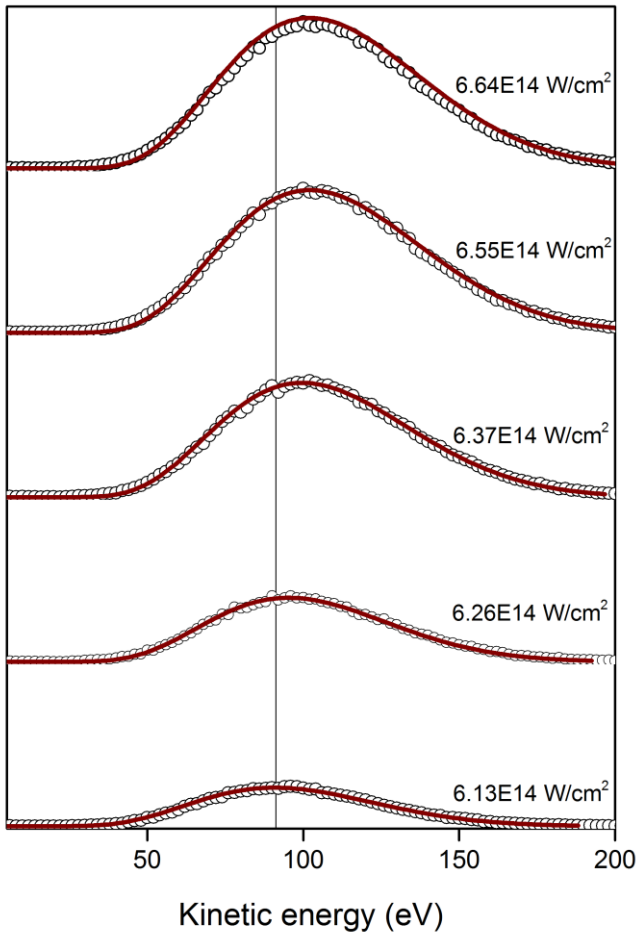

Figure 5.8. Distribution of electron kinetic energies in the plane of circular polarization. The photoemission spectra were recorded at 0.6 mbar vapor pressure and different laser peak intensity. The open circles represent the experimental data. The red solid lines represent the predictions by SFA theory in the length gauge.

5.3 Conclusion

In conclusion, the space-charge effect in the angle-resolved photoemission spectra from the gas-phase (vapor water) generated by a single strong infrared laser pulse was investigated for the linear and circular polarizations of the laser field. For a given peak intensity, the magnitude of this effect is found to be different for the two cases of polarization. The photoelectron yield was recorded in a high dynamics range of the signal, exhibiting both the direct and HATI contributions produced by linearly polarized field. It was shown that the HATI plateaus formed by the fast photoelectrons, is not affected by SCE. However, the direct ionization electrons below the $2U_p$ kinetic energy experience strong SCE. This was confirmed in both studies, where the gas density and the laser peak intensity were varied respectively. In particular, the higher-energy electrons from direct ionization (above the direct ATI peak) are found to be accelerated by the SCE, whereas the lower-energy ATI electrons experience deceleration due to the SCE.

In the case of the circularly polarized field, the SCE in the photoemission spectra is found to be negligibly small at the medium density and laser peak intensity applied in the experiment. This indicates that at the given experimental parameters the ionization yield in circularly polarization field much smaller than in the field of linear polarization, and much higher laser intensities (or medium densities) need to be applied to make this effect essential.

The theory based on the strong-field approximation in the length gauge was applied to simulate photoemission spectra in the circularly polarized field. It was demonstrated that this theory reproduces well the experiment.

Zusammenfassung

In dieser Studie wurden mittels Photoelektronenspektroskopie die lichtinduzierten Prozesse, die durch ein intensives Laserfeld an Flüssigkeitsgrenzflächen hervorgerufen werden, untersucht. Photoelektronen, die von dem intensiven optischen Feld eines ultrakurzen Laserpulses in einer dichten Probe erzeugt werden, führen zu einem Raumladungseffekt RLE, der die Emissionsspektren verändert. Der RLE ist daher Begleiterscheinung anderer Prozesse, die von intensiven Lasern erzeugt werden. Insbesondere führen sie zu Änderungen in der Spektralverteilung der Photoelektronen und reduzieren damit die Energieauflösung des Photoelektronenspektroskopie-experiments. Die vorliegende Arbeit beschäftigt sich mit der Untersuchung der Haupteigenschaften des RLE in Anregungs-Abfrage-Experimenten und Experimenten mit einem einzelnen Laserpuls hoher Spitzenintensität.

Zuerst wurde das Auftreten des RLE für den Fall von Photoelektronenspektren von Flüssigkeiten, die mittels Anregungs-Abfrage-Experimenten durchgeführt wurden, untersucht. Die beiden Techniken Anregungs-Abfrage-Spektroskopie und die Flüssigkeitsmikrojettechnik wurden in dieser Arbeit zusammen angewandt. Im Allgemeinen ermöglicht die Verbindung dieser beiden Techniken die Untersuchung der Elektronendynamik und Struktur in Lösungen und an Grenzflächen.

In diesem Fall wurde eine Kaliumhexacyanidoferrat(II)-Lösung $[Fe(CN)_6]^{4-}$ als Modellsystem verwendet. Der Einfluss der Intensität des Anregungslasers auf den RLE wurde untersucht. Es wurde beobachtet, dass eine große Zahl von Photonen pro XUV Puls eine Verbreiterung von Peaks und eine positive Verschiebung der Energien aufgrund des RLE erzeugt.

Für das Anregungs-Abfrage-Experiment wurde UV-Licht mit einer Photonenenergie von 4.65 eV verwendet, um die Elektronendynamik von $[Fe(CN)_6]^{4-}$ auszulösen. Mit dem XUV-Strahl aus einer HHG-Quelle mit einer Photonenenergie von 32.55 eV wurde die gesamte

elektronische Struktur der Valenzschalen von Cyanoferrat in einem Ein-Photonenschritt zum Kontinuum untersucht. Es wurde gezeigt, dass die Reihenfolge der Anregungs-Abfrage-Pulse (welcher Puls interagiert zuerst mit der Probe) eine wichtige Rolle in der Erscheinung des RLE spielt. Insbesondere wurde eine positive Energieverschiebung in den Photoelektronenspektren bei negativer Zeitverzögerung (der Abfrage Puls kommt vor dem Anregungspuls an) beobachtet. Bei umgekehrter Reihenfolge wurde eine große negative Verschiebung beobachtet.

Die positive Verschiebung wird durch einen negativen RLE erzeugt, der mittels Elektron-Elektron-Wechselwirkung zu einer Beschleunigung der XUV-Photoelek-tronen im Fernfeld führt. Die negative Energieverschiebung wird durch einen positiven RLE hervorgerufen, der durch positive Ionen in der flüssigen Probe erzeugt wird. Die Abfuhr der während der Ionisation in der Probe erzeugten positiven Ladungen findet auf einer Zeitskala von Nanosekunden statt. Solch lange Zeiten verdeutlichen die eingeschränkte Ladungsträgermobilität in Flüssigkeiten verglichen zu der in leitfähigen Festkörpern.

Ein Modell basierend auf der mean-field Betrachtung und dem Superpositionsprinzip von Feldern wurde zur Beschreibung des RLE entwickelt. Das Modell beschreibt die spektrale Verschiebung der Photoelektronen, die im Experiment beobachtet wurde, gut. Es sei darauf hingewiesen, dass die spektrale Verschiebung das Hauptresultat des RLE ist und dass unter den gewählten Bedingungen keine spektrale Verbreiterung beobachtet wurde.

Im zweiten Teil wurde der RLE, der von einem einzelnen Laserpuls hoher Intensität in einem Gas hoher Dichter erzeugt wird, untersucht. Unter den gegebenen experimentellen Bedingungen wie Spitzenintensität des Lasers und Gasdichte, war der RLE deutlich stärker im Fall von linear polarisiertem Licht verglichen zum Fall von zirkular polarisiertem Licht. Diese Beobachtung wurde in zwei Studien bestätigt, in denen die Spitzenintensität des Lasers beziehungsweise die Gasdichte variiert wurden. Dies lässt sich mit der Tatsache interpretieren, dass die Ionisationsrate in zirkularen, intensiven Feldern viel kleiner als in linear polarisierten Feldern ist.

Im Fall von linear polarisiertem Licht enthalten die Photoemissionsspektren Beiträge von direkten Photoelektronen, die einen Peak bei niedrigen kinetischen Energien erzeugen und Beiträge von HATI-Elektronen, die ein Plateau über eine Energie von $2U_P$ hinaus erzeugen. Die Stärke des RLE war abhängig von der kinetischen Energie. Insbesondere sind die schnellen HATI-Elektronen nicht vom RLE beeinflusst. Die langsamen Elektronen erfahren hingegen einen starken RLE. Der RLE führt zur Umverteilung von Photoelektronen, die den Peak der direkten Emission erzeugen. Langsame Elektronen werden abgebremst und schnelle Elektronen werden beschleunigt.

Im Fall eines zirkular polarisierten Feldes kann das Fehlen des der RLE sowohl für langsame als auch für schnelle Elektronen mit der geringen Ionisationsausbeute erklärt werden, die dazu führt, dass die Elektronendichte nicht hoch genug ist um den RLE hervorzurufen. Die Photoemissionsspektren von zirkular polarisiertem Licht wurden dazu verwandt, die Strong-Field-Approximation (SFA) zu untersuchen. Unter Berücksichtigung der räumlichen und zeitlichen Verteilung der Laserintensität im Fokus lassen sich die gemessenen Photoemissionsspektren gut reproduzieren.

Der RLE in Experimenten, die die Verwendung von intensiven Laserfeldern erfordern, nicht vernachlässigt werden. Die vorgelegte Arbeit beschreibt den Ansatz, wie der RLE in der Auswertung von Photoelektronenspektren berücksichtigt werden kann.

Summary

In this study, the method of photoelectron spectroscopy was applied to investigate the photo-process induced by a strong laser field at a liquid interface. The photoelectrons generated by the intense optical field of short pulses in the medium of high density give rise to space-charge effect (SCE) that modifies the emission spectra. Thus, the SCE accompanies other processes induced in a strong laser field. Namely, it causes distortion of the spectral distribution of photoelectrons and, as a result, it decreases the energy resolution in the photoelectron spectroscopy measurements. The present work was focused on revealing the main features of the SCE in pump-probe experiments as well as in experiments with the use of a single laser pulse of high peak intensity.

First, a manifestation of the SCE in photoelectrons spectra obtained by the method of time-resolved photoelectron spectroscopy was investigated in the case of a liquid sample. A combination of two techniques, pump-probe photoelectrons spectroscopy, and the liquid microjet techniques, was applied in this study. Such a combination, in general, provides the unique possibility to study the electronic and structural dynamics in solutions and interfaces.

Here, an aqueous solution of potassium ferrocyanide $[Fe(CN)_6]^{4-}$ was used in the experiment as a model sample. The effect of the laser intensity of probe pulse only on the SCE was investigated. It was observed that at a large number of photon per pulse of the XUV pulse SCE causes a peak broadening and positive energy shift.

For the pump-probe experiment, UV light of 4.65 eV photon energy was used to initiate the electronic dynamics of $[Fe(CN)_6]^{4-}$. The XUV beam from high-order harmonic generation (HHG) of 32.55 eV photon energy source was used to probe the entire electronic structure of the valence shell of the ferrocyanide in a one-photon transition to the continuum. The sequence of the pump-probe pulses (which pulse interacts with the sample first) was shown to play a significant role in the manifestation of the SCE. In particular, a positive energy

shift in the photoelectron spectra was observed at negative time delays (the probe pulse arriving before the pump pulse). When the pulse sequence is reversed, a large negative energy shift was observed in the photoelectron spectra.

The positive energy shift is caused by the negative space charge effect originating from the electron-electron interaction, resulting acceleration the XUV photoelectrons in the far field. The negative energy shift is caused by positive space charge effect originating from the interaction of photoelectrons with positive ions originating in the liquid sample. The latter results in the deceleration of the XUV photoelectrons. The dissipation of the positive charge generated during the ionization process of the sample was found to occur on a nanosecond time scale. Such a long scale reflects the restricted carrier mobility in liquids, as compared to solid conductors.

A model based on *the mean-field consideration* and the *field superposition principle* was developed to described the SCE. The model reproduces well the spectral shift of XUV photoelectrons observed in the experiment. One should note that the spectral shift represents the main result of the SCE, and no spectral broadening was observed under the applied experimental conditions.

In the second part, the SCE induced in the photoemission spectra by a single laser pulse of high intensity was studied in a dense gas. At the given experimental conditions, including the laser peak intensity and the gas density, the magnitude of the SCE was found to be much larger in the case of linearly polarized field than for circular polarization. This finding was confirmed in two studies, where the laser peak intensity and the gas density were varied, respectively. The interpretation lies in the fact that the ionization rate in the circularly strong field is much lower than in the linearly polarized field.

In the case of linearly polarized light, the photoemission spectra show the contributions of the direct photoelectrons forming a peak at lower kinetic energies, and the contributions of HATI electrons forming a plateau beyond the $2U_P$ energy. The magnitude of the SCE was

found to be dependent on the kinetic energy value. In particular, the fast HATI electrons are not influenced by the SCE. However, the slower direct electrons experience strong SCE. The SCE leads to redistribution of photoelectrons forming the energy peak of the direct emission. Here, the slower electrons become decelerated, and the faster electrons are accelerated.

In the case of a circularly polarized field, the SCE is absent for both the slow and fast photoelectrons and can be attributed to the fact that under the experimental conditions ionization yields are too small to produce the high electron densities necessary for SCE to occur. The photoemission spectra of circularly polarized light were used to test the strong-field-approximation (SFA) theory. By taking the spatiotemporal distribution of the laser intensity in the focus into account, the simulated spectra reproduce well the measured photoemission spectra.

The SCE cannot be disregard in the experiments requiring the application of strong laser fields. The present work provides the approach how to treat the SCE in the analysis of photoelectrons spectra.

Bibliography:

1. Joshi, C.J. and P.B. Corkum, *Interactions of ultra-intense laser light with matter.* Physics Today, 1995. **48**(1): p. 36-44.
2. Hoffmann, M.C. and J.A. Fülöp, *Intense ultrashort terahertz pulses: generation and applications.* Journal of Physics D: Applied Physics, 2011. **44**(8): p. 083001.
3. Van Dao, L., et al., *Generation of high flux, highly coherent extreme ultraviolet radiation in a gas cell.* Journal of Applied Physics, 2008. **104**(2): p. 023105.
4. He, X., et al., *Spatial and spectral properties of the high-order harmonic emission in argon for seeding applications.* Physical Review A, 2009. **79**(6): p. 063829.
5. Bauer, M., *Femtosecond ultraviolet photoelectron spectroscopy of ultra-fast surface processes.* Journal of Physics D: Applied Physics, 2005. **38**(16): p. R253.
6. Dietrich, P. and P.B. Corkum, *Ionization and dissociation of diatomic molecules in intense infrared laser fields.* The Journal of chemical physics, 1992. **97**(5): p. 3187-3198.
7. Link, O., et al., *Ultrafast phase transitions in metastable water near liquid interfaces.* Faraday discussions, 2009. **141**: p. 67-79.
8. Hatamoto, T., et al., *Strong-field ionization of alcohols: An electron spectroscopic study of ionization dynamics.* Chemical physics letters, 2007. **439**(4): p. 296-300.
9. Hansch, P., M. Walker, and L. Van Woerkom, *Resonant hot-electron production in above-threshold ionization.* Physical Review A, 1997. **55**(4): p. R2535.
10. Eberly, J.H., J. Javanainen, and K. Rzążewski, *Above-threshold ionization.* Physics reports, 1991. **204**(5): p. 331-383.
11. Freeman, R. and P. Bucksbaum, *Investigations of above-threshold ionization using subpicosecond laser pulses.* Journal of Physics B: Atomic, Molecular and Optical Physics, 1991. **24**(2): p. 325.
12. Paulus, G., W. Nicklich, and H. Walther, *Investigation of above-threshold ionization with femtosecond pulses: connection between plateau and angular distribution of the photoelectrons.* EPL (Europhysics Letters), 1994. **27**(4): p. 267.
13. Rudenko, A., et al., *Resonant structures in the low-energy electron continuum for single ionization of atoms in the tunnelling regime.* Journal of Physics B: Atomic, Molecular and Optical Physics, 2004. **37**(24): p. L407.
14. Blaga, C., et al., *Strong-field photoionization revisited.* Nature Physics, 2009. **5**(5): p. 335-338.

15. Joachain, C.J., N.J. Kylstra, and R.M. Potvliege, *Atoms in intense laser fields*. 2012: Cambridge University Press.
16. Milošević, D., et al., *Above-threshold ionization by few-cycle pulses.* Journal of Physics B: Atomic, Molecular and Optical Physics, 2006. **39**(14): p. R203.
17. Dyke, J., et al., *Gas phase HeI photoelectron spectra of some transition metals: Cu, Ag, Au, Cr and Mn.* Journal of Physics B: Atomic and Molecular Physics, 1979. **12**(18): p. 2985.
18. Pireaux, J. and R. Caudano, *X-ray photoemission study of core-electron relaxation energies and valence-band formation of the linear alkanes. II. Solid-phase measurements.* Physical Review B, 1977. **15**(4): p. 2242.
19. Rye, R., et al., *Chemical-state effects in Auger electron spectroscopy.* The Journal of Chemical Physics, 1978. **69**(4): p. 1504-1512.
20. Kothe, A., et al., *Charge transfer to solvent dynamics in iodide aqueous solution studied at ionization threshold.* Physical Chemistry Chemical Physics, 2015. **17**(3): p. 1918-1924.
21. Nordlund, D., et al., *Electronic structure effects in liquid water studied by photoelectron spectroscopy and density functional theory.* Chemical Physics Letters, 2008. **460**(1): p. 86-92.
22. Faubel, M., et al., *Ultrafast soft X-ray photoelectron spectroscopy at liquid water microjets.* Accounts of chemical research, 2011. **45**(1): p. 120-130.
23. Bressler, C. and M. Chergui, *Molecular structural dynamics probed by ultrafast X-ray absorption spectroscopy.* Annual review of physical chemistry, 2010. **61**: p. 263-282.
24. Dierker, B., et al., *Probing orbital symmetry in solution: polarization-dependent resonant inelastic soft x-ray scattering on liquid micro-jet.* New Journal of Physics, 2013. **15**(9): p. 093025.
25. Lange, K.M. and E.F. Aziz, *Electronic structure of ions and molecules in solution: a view from modern soft X-ray spectroscopies.* Chemical Society Reviews, 2013. **42**(16): p. 6840-6859.
26. Brandenburg, T., et al., *The electronic structure of perfluorodecalin studied by soft X-ray spectroscopy and electronic structure calculations.* Physical Chemistry Chemical Physics, 2014. **16**(42): p. 23379-23385.
27. Petit, T., et al., *Probing ion-specific effects on aqueous acetate solutions: Ion pairing versus water structure modifications.* Structural Dynamics, 2014. **1**(3): p. 034901.

28. Faubel, M., S. Schlemmer, and J. Toennies, *A molecular beam study of the evaporation of water from a liquid jet*. Zeitschrift für Physik D Atoms, Molecules and Clusters, 1988. **10**(2-3): p. 269-277.

29. Faubel, M. and T. Kisters, *Non-equilibrium molecular evaporation of carboxylic acid dimers*. 1989.

30. Lange, K.M., et al., *Ligand discrimination of myoglobin in solution: an iron L-edge X-ray absorption study of the active centre*. Chemical Communications, 2013. **49**(39): p. 4163-4165.

31. Panzer, D., et al., *Water influences on the copper active site in hemocyanin*. The Journal of Physical Chemistry Letters, 2010. **1**(10): p. 1642-1647.

32. Bergmann, N., et al., *On the enzymatic activity of catalase: an iron L-edge X-ray absorption study of the active centre*. Physical Chemistry Chemical Physics, 2010. **12**(18): p. 4827-4832.

33. Aziz, E.F., et al., *Probing the electronic structure of the hemoglobin active center in physiological solutions*. Physical review letters, 2009. **102**(6): p. 068103.

34. Bagchi, B., *Dynamics of solvation and charge transfer reactions in dipolar liquids*. Annual Review of Physical Chemistry, 1989. **40**(1): p. 115-141.

35. Lange, K.M. and E.F. Aziz, *The Hydrogen Bond of Water from the Perspective of Soft X-Ray Spectroscopy*. Chemistry–An Asian Journal, 2013. **8**(2): p. 318-327.

36. Bressler, C., et al., *Femtosecond XANES study of the light-induced spin crossover dynamics in an iron (II) complex*. Science, 2009. **323**(5913): p. 489-492.

37. Cannizzo, A., et al., *Light-induced spin crossover in Fe (II)-based complexes: The full photocycle unraveled by ultrafast optical and X-ray spectroscopies*. Coordination Chemistry Reviews, 2010. **254**(21): p. 2677-2686.

38. Reinhard, M., et al., *Photooxidation and photoaquation of iron hexacyanide in aqueous solution: A picosecond X-ray absorption study*. Structural Dynamics, 2014. **1**(2): p. 024901.

39. Gawelda, W., et al., *Ultrafast nonadiabatic dynamics of [FeII (bpy) 3] 2+ in solution*. Journal of the American Chemical Society, 2007. **129**(26): p. 8199-8206.

40. Chen, X. and S.E. Bradforth, *The ultrafast dynamics of photodetachment*. Annu. Rev. Phys. Chem., 2008. **59**: p. 203-231.

41. Suzuki, T., *Femtosecond time-resolved photoelectron imaging*. Annu. Rev. Phys. Chem., 2006. **57**: p. 555-592.

42. Tang, Y., et al., *Time-resolved photoelectron spectroscopy of bulk liquids at ultra-low kinetic energy*. Chemical Physics Letters, 2010. **494**(1): p. 111-116.

43. Liu, S., et al., *Time-resolved photoelectron imaging using a femtosecond UV laser and a VUV free-electron laser.* Physical Review A, 2010. **81**(3): p. 031403.

44. Link, O., et al., *Ultrafast electronic spectroscopy for chemical analysis near liquid water interfaces: concepts and applications.* Applied Physics A, 2009. **96**(1): p. 117-135.

45. Arrell, C., et al., *A simple electron time-of-flight spectrometer for ultrafast vacuum ultraviolet photoelectron spectroscopy of liquid solutions.* Review of Scientific Instruments, 2014. **85**(10): p. 103117.

46. Ziemkiewicz, M.P., et al., *Femtosecond time-resolved XUV+ UV photoelectron imaging of pure helium nanodroplets.* The Journal of chemical physics, 2014. **141**(17): p. 174306.

47. Metje, J., et al., *Monochromatization of femtosecond XUV light pulses with the use of reflection zone plates.* Opt. Express, 2014. **22**(9): p. 10747-11760.

48. Clauberg, R. and A. Blacha, *High electron density effects in electron spectroscopies: Consequences for picosecond photoemission and electron-beam sampling.* Journal of Applied Physics, 1989. **65**(11): p. 4095-4106.

49. Vodopyanov, K., et al., *Laser induced electron emission from gold surface irradiated by picosecond pulses at $\lambda = 2.9\ \mu m$.* Applied Physics B, 1989. **48**(6): p. 485-488.

50. Passlack, S., et al., *Space charge effects in photoemission with a low repetition, high intensity femtosecond laser source.* Journal of applied physics, 2006. **100**(2): p. 024912.

51. Farkas, G. and C. Toth, *Energy spectrum of photoelectrons produced by picosecond laser-induced surface multiphoton photoeffect*. Physical Review A, 1990. **41**(7): p. 4123.

52. Oloff, L., et al., *Time-resolved HAXPES at SACLA: probe and pump pulse-induced space-charge effects.* New Journal of Physics, 2014. **16**(12): p. 123045.

53. Gribakin, G. and M.Y. Kuchiev, *Multiphoton detachment of electrons from negative ions.* Physical Review A, 1997. **55**(5): p. 3760.

54. Codling, K., et al., *Charge-symmetric fragmentation of diatomic molecules in intense picosecond laser fields.* Journal of Physics B: Atomic, Molecular and Optical Physics, 1991. **24**(23): p. L593.

55. Hutchinsons, M., et al., *High–intensity lasers: interactions with atoms, molecules and clusters.* Philosophical Transactions of the Royal Society of London A: Mathematical, Physical and Engineering Sciences, 1998. **356**(1736): p. 297-315.

56. G. N. Lewis, Nature Physics 118, 1926. **132**.

57. Damon, E. and R. Tomlinson, *Observation of ionization of gases by a ruby laser.* Applied Optics, 1963. **2**(5): p. 546-547.

58. Gavrila, M., *Atoms in intense laser fields.* 1992.

59. Mainfray, G. and G. Manus, *Multiphoton ionization of atoms.* Reports on progress in physics, 1991. **54**(10): p. 1333.

60. Bandrauk, A.D. and S.C. Wallace, *Coherence phenomena in atoms and molecules in laser fields*. Vol. 287. 2012: Springer Science & Business Media.

61. Delone, N.B. and M. Fedorov, *Above threshold ionization.* Progress in quantum electronics, 1989. **13**(4): p. 267-298.

62. Agostini, P., et al., *Free-free transitions following six-photon ionization of xenon atoms.* Physical Review Letters, 1979. **42**(17): p. 1127.

63. Petite, G., P. Agostini, and H.G. Muller, *Intensity dependence of non-perturbative above-threshold ionisation spectra: experimental study.* Journal of Physics B: Atomic, Molecular and Optical Physics, 1988. **21**(24): p. 4097.

64. Freeman, R., et al., *Above-threshold ionization with subpicosecond laser pulses.* Physical review letters, 1987. **59**(10): p. 1092.

65. Paulus, G., et al., *High-order above-threshold ionization of atomic hydrogen using intense, ultrashort laser pulses.* Journal of Physics B: Atomic, Molecular and Optical Physics, 1996. **29**(7): p. L249.

66. Busuladžić, M., A. Gazibegović-Busuladžić, and D. Milošević, *High-order above-threshold ionization in a laser field: Influence of the ionization potential on the high-energy cutoff.* Laser physics, 2006. **16**(2): p. 289-293.

67. Paulus, G., et al., *Plateau in above threshold ionization spectra.* Physical review letters, 1994. **72**(18): p. 2851.

68. Paulus, G., W. Becker, and H. Walther, *Classical rescattering effects in two-color above-threshold ionization.* Physical Review A, 1995. **52**(5): p. 4043.

69. Weingartshofer, A., et al., *Direct observation of multiphoton processes in laser-induced free-free transitions.* Physical Review Letters, 1977. **39**(5): p. 269.

70. Saathoff, G., et al., *Laser-assisted photoemission from surfaces.* Physical Review A, 2008. **77**(2): p. 022903.

71. Miaja-Avila, L., et al., *Laser-assisted photoelectric effect from surfaces.* Physical review letters, 2006. **97**(11): p. 113604.

72. Walker, B., et al., *Precision measurement of strong field double ionization of helium.* Physical review letters, 1994. **73**(9): p. 1227.

73. Ammosov, M.V., N.B. Delone, and V.P. Krainov. *Tunnel ionization of complex atoms and atomic ions in electromagnetic field*. in *1986 Quebec Symposium*. 1986. International Society for Optics and Photonics.

74. Corkum, P., N. Burnett, and F. Brunel, *Above-threshold ionization in the long-wavelength limit*. Physical review letters, 1989. **62**(11): p. 1259.

75. Keldysh, L., *Ionization in the field of a strong electromagnetic wave*. Sov. Phys. JETP, 1965. **20**(5): p. 1307-1314.

76. Reiss, H.R., *Foundations of strong-field physics*, in *Lectures on Ultrafast Intense Laser Science 1*. 2010, Springer. p. 41-84.

77. Bauer, D., D. Milošević, and W. Becker, *Strong-field approximation for intense-laser–atom processes: The choice of gauge*. Physical Review A, 2005. **72**(2): p. 023415.

78. Reiss, H.R., *Effect of an intense electromagnetic field on a weakly bound system*. Physical Review A, 1980. **22**(5): p. 1786.

79. Wolkow, D., *Über eine Klasse von Lösungen der Diracschen Gleichung*. Zeitschrift für Physik, 1935. **94**(3-4): p. 250-260.

80. Beiser, S., M. Klaiber, and I.Y. Kiyan, *Photodetachment in a strong circularly polarized laser field*. Physical Review A, 2004. **70**(1): p. 011402.

81. Keldysh, L., *Ionization in the field of a strong electromagnetic wave*. Zh. Eksperim. i Teor. Fiz., 1964. **47**.

82. Faisal, F.H., *Multiple absorption of laser photons by atoms*. Journal of Physics B: Atomic and Molecular Physics, 1973. **6**(4): p. L89.

83. Paulus, G.G., et al., *Rescattering effects in above-threshold ionization: a classical model*. Journal of Physics B: Atomic, Molecular and Optical Physics, 1994. **27**(21): p. L703.

84. New, G., *Introduction to Nonlinear Optics*. 2011: Cambridge University Press.

85. Franken, P., et al., *Generation of optical harmonics*. Physical Review Letters, 1961. **7**(4): p. 118.

86. New, G. and J. Ward, *Optical third-harmonic generation in gases*. Physical Review Letters, 1967. **19**(10): p. 556.

87. Metchkov, D., et al., *Fifth harmonic generation in sodium vapor*. Optics Communications, 1977. **21**(3): p. 391-394.

88. Wildenauer, J., *Generation of the 9th-harmonic, 11th-harmonic, and 15th-harmonic of iodine laser-radiation*. Journal of Applied Physics, 1987. **62**(1): p. 41-48.

89. Reintjes, J., C.-Y. She, and R.C. Eckardt, *Generation of coherent radiation in XUV by fifth-and seventh-order frequency conversion in rare gases.* Quantum Electronics, IEEE Journal of, 1978. **14**(8): p. 581-596.

90. Bokor, J., P. Bucksbaum, and R. Freeman, *Generation of 35.5-nm coherent radiation.* Optics letters, 1983. **8**(4): p. 217-219.

91. McPherson, A., et al., *Studies of multiphoton production of vacuum-ultraviolet radiation in the rare gases.* JOSA B, 1987. **4**(4): p. 595-601.

92. Li, X., et al., *Multiple-harmonic generation in rare gases at high laser intensity.* Physical Review A, 1989. **39**(11): p. 5751.

93. Miyazaki, K. and H. Sakai, *High-order harmonic generation in rare gases with intense subpicosecond dye laser pulses.* Journal of Physics B: Atomic, Molecular and Optical Physics, 1992. **25**(3): p. L83.

94. Corkum, P.B., *Plasma perspective on strong field multiphoton ionization.* Physical Review Letters, 1993. **71**(13): p. 1994.

95. Schafer, K., et al., *Above threshold ionization beyond the high harmonic cutoff.* Physical review letters, 1993. **70**(11): p. 1599.

96. Ferray, M., et al., *Multiple-harmonic conversion of 1064 nm radiation in rare gases.* Journal of Physics B: Atomic, Molecular and Optical Physics, 1988. **21**(3): p. L31.

97. Hertz, H., *Ueber einen Einfluss des ultravioletten Lichtes auf die electrische Entladung.* Annalen der Physik, 1887. **267**(8): p. 983-1000.

98. Reinert, F. and S. Hüfner, *Photoemission spectroscopy—from early days to recent applications.* New Journal of Physics, 2005. **7**(1): p. 97.

99. Hofmann, S., *Auger-and X-Ray Photoelectron Spectroscopy in Materials Science*

2013, Springer.

100. Einstein, A., *Über einen die Erzeugung und Verwandlung des Lichtes betreffenden heuristischen Gesichtspunkt*. Annalen der Physik, 1905. **322**(6): p. 132-148.

101. Bonzel, H.P. and C. Kleint, *On the history of photoemission.* Progress in surface science, 1995. **49**(2): p. 107-153.

102. Rutherford, E., *XXXVII. The connexion between the β and γ ray spectra.* The London, Edinburgh, and Dublin Philosophical Magazine and Journal of Science, 1914. **28**(165): p. 305-319.

103. Carlson, T.A., *Photoelectron spectroscopy.* Annual Review of Physical Chemistry, 1975. **26**(1): p. 211-234.

104. Eland, J.H., *Photoelectron spectroscopy: an introduction to ultraviolet photoelectron spectroscopy in the gas phase*. 2013: Elsevier.

105. Kordyuk, A., *ARPES experiment in fermiology of quasi-2D metals (Review Article).* Low Temperature Physics, 2014. **40**(4): p. 286-296.

106. Stolow, A., A.E. Bragg, and D.M. Neumark, *Femtosecond time-resolved photoelectron spectroscopy*. Chemical Reviews, 2004. **104**(4): p. 1719-1758.

107. Reid, K.L., *Photoelectron angular distributions.* Annual review of physical chemistry, 2003. **54**(1): p. 397-424.

108. Thürmer, S., et al., *Photoelectron angular distributions from liquid water: Effects of electron scattering*. Physical review letters, 2013. **111**(17): p. 173005.

109. Hüfner, S., *Photoelectron spectroscopy: principles and applications*. 2013: Springer Science & Business Media.

110. Carlson, T., *Photoelectron and Auger spectroscopy*. 2013: Springer Science & Business Media.

111. Nordling, C., E. Sokolowski, and K. Siegbahn, *Precision method for obtaining absolute values of atomic binding energies.* Physical Review, 1957. **105**(5): p. 1676.

112. Turner, D.W. and M. Al Jobory, *Determination of ionization potentials by photoelectron energy measurement*. The Journal of Chemical Physics, 1962. **37**(12): p. 3007-3008.

113. Feuerbacher, B., B. Fitton, and R.F. Willis, *Photoemission and the electronic properties of surfaces*. 1978: John Wiley & Sons.

114. Plummer, E., et al., *A comparison of surface electron spectroscopies.* Surface Science, 1985. **158**(1): p. 58-83.

115. Adawi, I., *Theory of the surface photoelectric effect for one and two photons.* Physical Review, 1964. **134**(3A): p. A788.

116. Ueba, H. and B. Gumhalter, *Theory of two-photon photoemission spectroscopy of surfaces.* Progress in surface science, 2007. **82**(4): p. 193-223.

117. Hurst, G., et al., *Resonance ionization spectroscopy and one-atom detection.* Reviews of Modern Physics, 1979. **51**(4): p. 767.

118. Schlag, E.W., *ZEKE SPECTROSCOPY. Edition anglaise*. 1998: Cambridge University Press.

119. Muller-Dethlefs, K. and E.W. Schlag, *High-resolution zero kinetic energy (ZEKE) photoelectron spectroscopy of molecular systems.* Annual Review of Physical Chemistry, 1991. **42**(1): p. 109-136.

120. Chance, B., *The accelerated flow method for rapid reactions.* Journal of the Franklin Institute, 1940. **229**(5): p. 613-640.

121. Porter, G. *Flash photolysis and spectroscopy. A new method for the study of free radical reactions*. in *Proceedings of the Royal Society of London A: Mathematical, Physical and Engineering Sciences*. 1950. The Royal Society.

122. Abramczyk, H., *Introduction to laser spectroscopy*. 2005: Elsevier.

123. Haight, R., et al., *Picosecond time-resolved photoemission study of the InP (110) surface.* Physical review letters, 1985. **54**(12): p. 1302.

124. Pallix, J.B. and S.D. Colson, *Time-resolved photoelectron studies of the relaxation of the S 1 (1 E") excited state of sym-triazine.* Chemical physics letters, 1985. **119**(1): p. 38-41.

125. Song, X., et al., *Direct observation of time-dependent intramolecular vibrational relaxation in jet-cooled p-n-alkylanilines by laser photoelectron spectroscopy.* Chemical physics letters, 1990. **174**(5): p. 377-384.

126. Smith, J., C. Lakshminarayan, and J. Knee, *Picosecond measurements of vibrational dynamics using pump–probe laser photoelectron spectroscopy.* The Journal of Chemical Physics, 1990. **93**(6): p. 4475-4476.

127. Syage, J.A., *Measurement of cluster reorganization by time-resolved photoelectron spectroscopy.* Chemical physics letters, 1993. **202**(3-4): p. 227-232.

128. Syage, J.A., *Ultrafast measurements of chemistry in clusters: Excited-state proton transfer.* The Journal of Physical Chemistry, 1995. **99**(16): p. 5772-5786.

129. Zewail, A.H., *Femtochemistry: Atomic-scale dynamics of the chemical bond.* The Journal of Physical Chemistry A, 2000. **104**(24): p. 5660-5694.

130. Baumert, T., R. Thalweiser, and G. Gerber, *Femtosecond two-photon ionization spectroscopy of the B state of Na 3 clusters.* Chemical physics letters, 1993. **209**(1): p. 29-34.

131. Stolow, A., *Femtosecond time-resolved photoelectron spectroscopy of polyatomic molecules.* Annual review of physical chemistry, 2003. **54**(1): p. 89-119.

132. Stolow, A., *Time-resolved photoelectron spectroscopy: Non-adiabatic dynamics in polyatomic molecules.* International Reviews in Physical Chemistry, 2003. **22**(2): p. 377-405.

133. Ullrich, S., et al., *Electronic relaxation dynamics in DNA and RNA bases studied by time-resolved photoelectron spectroscopy.* Physical Chemistry Chemical Physics, 2004. **6**(10): p. 2796-2801.

134. Girardeau-Montaut, C. and J. Girardeau-Montaut, *Space-charge effect on the energy spectrum of photoelectrons produced by high-intensity short-duration laser pulses on a metal.* Physical Review A, 1991. **44**(2): p. 1409.

135. Farkas, G., et al., *On the intensity dependence of the non-linear electron emission from silver induced by a high power laser beam*. Physics Letters A, 1967. **24**(9): p. 475-476.

136. Ammosov, M., *Influence of the Coulomb repulsion between electrons on their energy spectrum in the case of the nonlinear surface photoeffect*. JOSA B, 1991. **8**(11): p. 2260-2264.

137. Villeneuve, D., et al., *Space charge and plasma effects in zero kinetic energy (ZEKE) photoelectron spectroscopy*. The Journal of chemical physics, 1997. **107**(14): p. 5310-5318.

138. Riffe, D.M., et al., *Femtosecond thermionic emission from metals in the space-charge-limited regime.* JOSA B, 1993. **10**(8): p. 1424-1435.

139. Aeschlimann, M., et al., *Observation of surface enhanced multiphoton photoemission from metal surfaces in the short pulse limit*. The Journal of chemical physics, 1995. **102**(21): p. 8606-8613.

140. Graf, J., et al., *Vacuum space charge effect in laser-based solid-state photoemission spectroscopy*. Journal of applied physics, 2010. **107**(1): p. 014912.

141. He, Y., et al., *High Resolution Angle Resolved Photoemission with Tabletop 11eV Laser*. arXiv preprint arXiv:1509.01311, 2015.

142. Hellmann, S., et al., *Time-resolved x-ray photoelectron spectroscopy at FLASH.* New Journal of Physics, 2012. **14**(1): p. 013062.

143. Dell'Angela, M., et al., *Vacuum space charge effects in sub-picosecond soft X-ray photoemission on a molecular adsorbate layer*. Structural Dynamics, 2015. **2**(2): p. 025101.

144. Zhou, X., et al., *Space charge effect and mirror charge effect in photoemission spectroscopy*. Journal of electron spectroscopy and related phenomena, 2005. **142**(1): p. 27-38.

145. Pietzsch, A., et al., *Towards time resolved core level photoelectron spectroscopy with femtosecond x-ray free-electron lasers.* New Journal of Physics, 2008. **10**(3): p. 033004.

146. Winter, B., et al., *Full valence band photoemission from liquid water using EUV synchrotron radiation.* The Journal of Physical Chemistry A, 2004. **108**(14): p. 2625-2632.

147. Faubel, M., B. Steiner, and J.P. Toennies, *Photoelectron spectroscopy of liquid water, some alcohols, and pure nonane in free micro jets.* The Journal of chemical physics, 1997. **106**(22): p. 9013-9031.

148. Myneni, S., et al., *LETTER TO THE EDITOR: Spectroscopic probing of local hydrogen-bonding structures in liquid water.* Journal of Physics Condensed Matter, 2002. **14**: p. L213-L219.

149. Bergmann, U., et al., *X-ray Raman spectroscopy at the oxygen K edge of water and ice: Implications on local structure models.* Physical Review B, 2002. **66**(9): p. 092107.

150. Guo, J.-H., et al., *X-ray emission spectroscopy of hydrogen bonding and electronic structure of liquid water.* Physical review letters, 2002. **89**(13): p. 137402.

151. Tokushima, T., et al., *High resolution X-ray emission spectroscopy of liquid water: The observation of two structural motifs.* Chemical Physics Letters, 2008. **460**(4): p. 387-400.

152. Nishizawa, K., et al., *High-resolution soft X-ray photoelectron spectroscopy of liquid water.* Physical Chemistry Chemical Physics, 2011. **13**(2): p. 413-417.

153. Winter, B., et al., *Hydrogen bonds in liquid water studied by photoelectron spectroscopy.* The Journal of chemical physics, 2007. **126**(12): p. 124504-124504.

154. Huse, N., et al., *Probing the hydrogen-bond network of water via time-resolved soft x-ray spectroscopy.* Physical Chemistry Chemical Physics, 2009. **11**(20): p. 3951-3957.

155. Wilson, K.R., et al., *X-ray spectroscopy of liquid water microjets.* The Journal of Physical Chemistry B, 2001. **105**(17): p. 3346-3349.

156. Migus, A., et al., *Excess electrons in liquid water: first evidence of a prehydrated state with femtosecond lifetime.* Physical review letters, 1987. **58**(15): p. 1559.

157. Gauduel, Y., et al., *Femtosecond dynamics of geminate pair recombination in pure liquid water.* The Journal of Physical Chemistry, 1989. **93**(10): p. 3880-3882.

158. Gauduel, Y., et al., *Some evidence of ultrafast H 2 O+-water molecule reaction in femtosecond photoionization of pure liquid water: Influence on geminate pair recombination dynamics.* Chemical physics, 1990. **149**(1): p. 1-10.

159. Long, F.H., H. Lu, and K.B. Eisenthal, *Femtosecond studies of electron-cation dynamics in neat water: The effects of isotope substitution.* Chemical Physics Letters, 1989. **160**(4): p. 464-468.

160. McGowen, J., et al., *Femtosecond studies of hydrated electron recombination following multiphoton ionization at 390 nm.* Chemical physics letters, 1994. **231**(4): p. 504-510.

161. Hertwig, A., et al., *Ultrafast relaxation dynamics of solvated electrons in water.* Berichte der Bunsengesellschaft für physikalische Chemie, 1998. **102**(6): p. 805-810.

162. Yamamoto, Y.-i., et al., *Time-and Angle-Resolved Photoemission Spectroscopy of Hydrated Electrons Near a Liquid Water Surface.* Physical review letters, 2014. **112**(18): p. 187603.

163. Siefermann, K.R., et al., *Binding energies, lifetimes and implications of bulk and interface solvated electrons in water.* Nature chemistry, 2010. **2**(4): p. 274-279.

164. E. Frisch, M.F., and G.W. Trucks. , *Gaussian 03. Gaussian, (2003).*

165. Elles, C.G., et al., *Excitation-energy dependence of the mechanism for two-photon ionization of liquid H2O and D2O from 8.3 to12. 4eV.* The Journal of chemical physics, 2006. **125**(4): p. 044515.

166. Coe, J.V., et al., *Using cluster studies to approach the electronic structure of bulk water: Reassessing the vacuum level, conduction band edge, and band gap of water.* The Journal of chemical physics, 1997. **107**(16): p. 6023-6031.

167. Goulet, T., et al., *On the electronic structure of liquid water: conduction-band tail revealed by photoionization data.* Chemical Physics Letters, 1990. **170**(5): p. 492-496.

168. Sander, M.U., et al., *Liquid water ionization: mechanistic implications of the H/D isotope effect in the geminate recombination of hydrated electrons.* Chemical Physics, 2000. **258**(2): p. 257-265.

169. Sander, M.U., K. Luther, and J. Troe, *Excitation energy dependence of the photoionization of liquid water.* The Journal of Physical Chemistry, 1993. **97**(44): p. 11489-11492.

170. Hocking, R.K., et al., *Fe L-edge XAS studies of K4 [Fe (CN) 6] and K3 [Fe (CN) 6]: A direct probe of back-bonding.* Journal of the American Chemical Society, 2006. **128**(32): p. 10442-10451.

171. Seidel, R., et al., *Valence Photoemission Spectra of Aqueous Fe2+/3+ and [Fe (CN) 6] 4–/3–and Their Interpretation by DFT Calculations.* The Journal of Physical Chemistry B, 2011. **115**(40): p. 11671-11677.

172. Engel, N., et al., *Chemical Bonding in Aqueous Ferrocyanide: Experimental and Theoretical X-ray Spectroscopic Study.* The Journal of Physical Chemistry B, 2014. **118**(6): p. 1555-1563.

173. Aristov, V., et al., *Focusing properties of shaped multilayer x-ray mirrors.* JETP Lett, 1986. **44**(4): p. 265.

174. Rulliere, C., *Femtosecond laser pulses*. 2005: Springer.

175. Poletto, L. and F. Frassetto, *Time-preserving grating monochromators for ultrafast extreme-ultraviolet pulses.* Applied optics, 2010. **49**(28): p. 5465-5473.

176. Seidel, R., S. Thürmer, and B. Winter, *Photoelectron spectroscopy meets aqueous solution: studies from a vacuum liquid microjet*. The Journal of Physical Chemistry Letters, 2011. **2**(6): p. 633-641.

177. Winter, B., et al., *Electron binding energies of aqueous alkali and halide ions: EUV photoelectron spectroscopy of liquid solutions and combined ab initio and molecular dynamics calculations.* Journal of the American Chemical Society, 2005. **127**(19): p. 7203-7214.

178. Ottosson, N., et al., *Photoelectron spectroscopy of liquid water and aqueous solution: Electron effective attenuation lengths and emission-angle anisotropy.* Journal of Electron Spectroscopy and Related Phenomena, 2010. **177**(2): p. 60-70.

179. Winter, B. and M. Faubel, *Photoemission from liquid aqueous solutions.* Chemical reviews, 2006. **106**(4): p. 1176-1211.

180. Winter, B., *Liquid microjet for photoelectron spectroscopy.* Nuclear Instruments and Methods in Physics Research Section A: Accelerators, Spectrometers, Detectors and Associated Equipment, 2009. **601**(1): p. 139-150.

181. Kurahashi, N., et al., *Photoelectron spectroscopy of aqueous solutions: Streaming potentials of NaX (X= Cl, Br, and I) solutions and electron binding energies of liquid water and X^-.* The Journal of chemical physics, 2014. **140**(17): p. 174506.

182. Collin, S., et al., *Transverse and longitudinal space-charge-induced broadenings of ultrafast electron packets.* Journal of applied physics, 2005. **98**(9): p. 094910.

183. Kothe, A., et al., *Time-of-flight electron spectrometer for a broad range of kinetic energies.* Review of Scientific Instruments, 2013. **84**(2): p. 023106.

184. Träger, F., *Springer handbook of lasers and optics*. 2007: Springer Science & Business Media.

185. Frietsch, B., et al., *A high-order harmonic generation apparatus for time-and angle-resolved photoelectron spectroscopy.* Review of Scientific Instruments, 2013. **84**(7): p. 075106.

186. Hellmann, S., et al., *Time-resolved x-ray photoelectron spectroscopy at FLASH.* New Journal of Physics, 2012. **14**(1): p. 013062.

187. Hellmann, S., et al., *Vacuum space-charge effects in solid-state photoemission.* Physical Review B, 2009. **79**(3): p. 035402.

188. Wernet, P., et al., *Femtosecond time-resolved photoelectron spectroscopy with a vacuum-ultraviolet photon source based on laser high-order harmonic generation.* Review of Scientific Instruments, 2011. **82**(6): p. 063114.

189. Leuenberger, D., et al., *Disentanglement of electron dynamics and space-charge effects in time-resolved photoemission from h-BN/Ni (111).* Physical Review B, 2011. **84**(12): p. 125107.

190. Tao, Z., et al., *Space charge effects in ultrafast electron diffraction and imaging.* Journal of Applied Physics, 2012. **111**(4): p. 044316.

191. Delahay, P. and K. Von Burg, *Photoelectron emission spectroscopy of liquid water.* Chemical Physics Letters, 1981. **83**(2): p. 250-254.

192. Farkas, G., et al., *On the laser-induced non-linear photoelectric effect in metals.* Physics Letters A, 1967. **25**(8): p. 572-573.

193. Lin, S.H., *Multiphoton spectroscopy of molecules*. 2012: Elsevier.

194. Speiser, S., O. Kafri, and S. Kimel, *A correction factor for experimental multiphoton absorption cross section.* Chemical Physics Letters, 1972. **14**(3): p. 369-371.

195. Speiser, S. and J. Jortner, *The 32 power law for high order multiphoton processes.* Chemical Physics Letters, 1976. **44**(3): p. 399-403.

196. Uiterwaal, C., et al., *Generalized multiphoton-ionization cross sections of the rare gases for 500-fs, 248.6-nm pulses.* Physical Review A, 1998. **57**(1): p. 392.

197. Barnes, J. and P. Hut, *A hierarchical O (N log N) force-calculation algorithm*. 1986.

198. Reed, B.W., *Femtosecond electron pulse propagation for ultrafast electron diffraction.* Journal of applied physics, 2006. **100**(3): p. 034916.

199. Siwick, B.J., et al., *Ultrafast electron optics: Propagation dynamics of femtosecond electron packets.* Journal of Applied Physics, 2002. **92**(3): p. 1643-1648.

200. Qian, B.-L. and H.E. Elsayed-Ali, *Electron pulse broadening due to space charge effects in a photoelectron gun for electron diffraction and streak camera systems.* Journal of applied physics, 2002. **91**(1): p. 462-468.

201. Grunewald, M., et al., *Mean field approach to the electron glass.* Journal of Physics C: Solid State Physics, 1982. **15**(32): p. L1153.

202. Bakshi, V.B.U., *Electromagnetic Fields*. 2008: Technical Publications.

203. Marsi, M., et al., *Transient charge carrier distribution at UV-photoexcited SiO 2/S i interfaces.* Physical Review B, 2000. **61**(8): p. R5070.

204. Spencer, B.F., et al., *Time-resolved surface photovoltage measurements at n-type photovoltaic surfaces: Si (111) and ZnO (10 1¯ 0).* Physical Review B, 2013. **88**(19): p. 195301.

205. Nandor, M., M. Walker, and L. Van Woerkom, *Angular distributions of high-intensity ATI and the onset of the plateau.* Journal of Physics B: Atomic, Molecular and Optical Physics, 1998. **31**(20): p. 4617.

206. Lohr, A., et al., *Above-threshold ionization in the tunneling regime.* Physical Review A, 1997. **55**(6): p. R4003.

207. Krainov, V. and B. Shokri, *Energy and angular distributions of electrons resulting from barrier-suppression ionization of atoms by strong low-frequency radiation.* Journal of Experimental and Theoretical Physics, 1995. **80**(4): p. 657-661.

208. Nikishov, A. and V. Ritus, *Ionization of systems bound by short-range forces by the field of an electromagnetic wave.* Soviet Physics JETP, 1966. **23**(1).

209. Protopapas, M., D. Lappas, and P. Knight, *Strong field ionization in arbitrary laser polarizations.* Physical review letters, 1997. **79**(23): p. 4550.

210. Bergues, B., et al., *Reply to "Comment on 'Photodetachment in a strong laser field: An experimental test of Keldysh-like theories'".* Physical Review A, 2008. **77**(6): p. 067402.

Erklärung der Selbstständigkeit

Hiermit versichere ich, die vorliegende Arbeit selbstständig verfasst und anderen als die angegebenen Quellen und Hilfsmittel benutzt sowie die Zitate deutlich kenntlich gemacht zu haben. Die Arbeit ist weder in einem früheren Promotionsverfahren angenommen noch als ungenügend beurteilt worden.

Berlin, den 25.08.2016

Al-Obaidi Ruba Taha Salim